McKelvey School of Engineering Theses & Dissertations

McKelvey School of Engineering

Spring 5-15-2015

Potential-flow Inflow Model Including Wake Distortion and Contraction

Jianzhe Huang
Washington University in St. Louis

WASHINGTON UNIVERSITY IN ST. LOUIS

School of Engineering and Applied Science
Department of Mechanical Engineering and Materials Science

Dissertation Examination Committee:
David Peters, Chair
Kenneth Jerina
Swami Karunamoorthy
Mark Meacham
Shankar Sastry
Heinz Schaettler

Potential-flow Inflow Model Including Wake Distortion and Contraction
by
Jianzhe Huang

A dissertation presented to the
Graduate School of Arts & Sciences
of Washington University in
partial fulfillment of the
requirements for the degree
of Doctor of Philosophy

May 2015
St. Louis, Missouri

<u>Table of Contents</u>

List of Figures

List of Tables

List of Symbols

$[A]$:   transform matrix

a_j^m: Morillo-Duffy variables

α_n^m: Nowak-He variables

m: harmonic numbers

n, j: polynomial numbers

$P_n^m(\nu)$:   normalized Legendre function of first kind

$Q_n^m(i\eta)$:   normalized Legendre function of second kind

R: rotor radius, m

ζ: non-dimensional coordinate along free-stream line, positive below disk

s: distance from the point of velocity computation along a streamline to the rotor disk at r_0, ψ_0

s_0: x-distance downstream in edgewise flow

t: time, sec

V_∞:   free-stream velocity, m/sec

V_{MD}:   induced velocity based on Morillo-Duffy variable

V_{NC}:   induced velocity based on Nowak-He variable

V_F: final induced velocity

V_{DS}:   downstream limiting velocity

χ: skew angle

τ_1^0:   elliptical pressure coefficient

τ_2^1:   cyclic pressure coefficient

τ_3^0:   second collective mode

σ: distance along x-axis from $(-s_0)$ to the point at which the velocity is desired, $\sigma = (-x - s_0)$

x, y, z: non-dimensional rotor disk coordinates, coordinate divided by R

ν, η, ψ: ellipsoidal coordinates

ν_0, η_0, ψ_0:   the ellipsoidal coordinates of the intersection point of rotor plane and the free-stream line

ω: reduced frequency, $\omega = \Omega R / V_\infty$

Ω: rotor speed, rad/sec

$m!!$:   double factorial, $m(m\text{-}2)(m\text{-}4)\ldots$

<u>Acknowledgments</u>

Washington University in St. Louis

May 2015

ABSTRACT OF THE DISSERTATION

Potential-Flow Inflow Model Including
Wake Distortion and Contraction
by
Jianzhe Huang
Doctor of Philosophy in Mechanical Engineering
Washington University in St. Louis, 2015
Professor David Peters, Chair

Dynamic wake models have been used in real-time flight simulations for over thirty years. The models have evolved from the earliest, three-degree-of-freedom models (derived from momentum theory) to full finite-state models derived from potential flow theory by a formal Galerkin method. These models are widely used in industry, but still have some drawbacks that need to be remedied. These drawbacks include: 1.) lack of good convergence both on the disk and off the disk (one can use one or the other but not both), 2.) poor results downstream in the limit of shallow skew angles, 3.) poor convergence inside of the rotor wake, 4.) lack of the effects of wake curvature and wake contraction, and 5.) lack of other important nonlinearities. This thesis uses applications of adjoint theorem, a special change of variable and effective introduction of solution blending to overcome these obstacles. The resultant model is well-behaved in all regimes and is applicable to use in realistic problems of flight simulation, even when only a few states are allowed.

Chapter 1: Introduction

1.1 Motivation

The analysis of any rotary-wing system requires a calculation of the flow field that is created by the lifting rotors that are part of the system. For real-time flight simulation and for preliminary design purposes, the computation of the induced-flow field must be very efficient. For this reason, finite-state models have been developed through the years to represent the flow in terms of state variables that represent induced flow shape functions. These will be discussed in detail in a later section. For now, it suffices to say that the models have evolved from simple models of the normal flow at the disk—in terms of a uniform component and flow gradients—to models that now include a complete expansion of all three components of flow everywhere in the flow field. The most sophisticated of these is the Fei model [1].

The major drawbacks of the more sophisticated models have been: 1.) they are not as well-conditioned as models that only give the normal component of inflow on the disk, such as the He model; 2.) they diverge downstream as the skew angle approaches $90\,°$(edgewise flow); and 3.) the more sophisticated models are linear, as opposed to the He-type models which are nonlinear, and important necessity for rotor analyses. Therefore, it is desirable to find a new type of model that combines the robustness of models like the He model with the generality of more flow information of models like the Fei model.

The first part of the approach taken here is to compute both the He second-form (which we call the Nowak-He variables) and the Fei states (which is called as Morillo-Duffy variables) from

a single set of unified inflow states. Those solutions can then hopefully be blended to obtain the well-behaved solution both on the disk and away from the disk.

The second task taken here is to eliminate the tendency of the flow to become divergent as one approaches edgewise flow. The reason for this issue is that, as the flow approaches the edgewise condition, the trailing wake moves closer and closer to the downstream rotor plane—so that the induced flow downstream does not decay. As a result, the Legendre Functions (which are the expansion functions and which all decay in the far field) are unable to converge to the velocity downstream. To remove this deficiency, the second part of the approach taken here is to use the Adjoint Theorem of Fei to compute the ill-behaved downstream velocity based on the well-behaved upstream velocity field. Therefore, the Adjoint Theorem is extended to the case of perfectly edgewise flow to show that the flow downstream can be computed from the velocity upstream.

The third and final task here is to make the appropriate nonlinear extensions to the more sophisticated Fei model so that it is ready to be used in production codes. In order to do this: 1.) the mass-flow parameter should be defined, 2.) the wake contraction effect must be considered according to the continuity equation, and 3.) the effect of wake curvature must be added to the formulation.

These all must be done in an integrated and unified way such that the simpler He-type models remain special cases of the new, unified, sophisticated model. That is the purpose of this work.

1.2   Previous Work

In the early 1980s, based on Mangler's actuator-disc theory [2], Dale Pitt and David Peters developed a linear, unsteady theory that relates the transient rotor loads (thrust, roll moment and

pitch moment) to the overall transient response of the rotor induced flow field, which is known as the Pitt-Peters model [3]. The perturbed induced inflow and the pressure distribution are defined as

$$\lambda = \lambda_0 + \bar{r}\lambda_s \sin(\bar{\psi}) + \bar{r}\lambda_c \cos(\bar{\psi}) \tag{1.1}$$

$$P = \sum_{m=0}^{1} \sum_{n=m+1}^{m+3} P_n^m(v)Q_n^m(i\eta)\left[C_n^m \cos(m\bar{\psi}) + D_n^m \sin(m\bar{\psi}) \right] \tag{1.2}$$

where v, η and $\bar{\psi}$ are ellipsoidal coordinates defined in Appendix 1. P_n^m and Q_n^m are associated Legendre functions of the first and second kinds, and C_n^m and D_n^m are coefficients which are functions of time and are governed by a set of ordinary differential equations. With the assumption of superposition of pressure, in which the velocity field is derived from superimposing the unsteady pressure and static pressure of the flow, they obtained a set of differential equations to obtain the dynamic inflow derivatives for a helicopter rotor with an unsteady loading and induced flow distribution. The equations are expressed as:

$$[M]\begin{Bmatrix} \overset{+}{\lambda_0} \\ \lambda_s \\ \lambda_c \end{Bmatrix} + [L]^{-1}\begin{Bmatrix} \lambda_0 \\ \lambda_s \\ \lambda_c \end{Bmatrix} = \begin{Bmatrix} C_T \\ -C_L \\ -C_M \end{Bmatrix} \tag{1.3}$$

where $[M]$ and $[L]$ are apparent mass matrix and the dynamic inflow gain matrix, respectively. They are defined as follows

$$[M] = \begin{bmatrix} \dfrac{128}{75\pi} & 0 & 0 \\[3mm] 0 & \dfrac{16}{45\pi} & 0 \\[3mm] 0 & 0 & \dfrac{16}{45\pi} \end{bmatrix} \tag{1.4}$$

$$[L] = \frac{1}{V} \begin{bmatrix} \dfrac{1}{2} & 0 & -\dfrac{15\pi}{64}\sqrt{\dfrac{1-\sin(\alpha)}{1+\sin(\alpha)}} \\[3mm] 0 & \dfrac{4}{1+\sin(\alpha)} & 0 \\[3mm] \dfrac{15\pi}{64}\sqrt{\dfrac{1-\sin(\alpha)}{1+\sin(\alpha)}} & 0 & \dfrac{4\sin(\alpha)}{1+\sin(\alpha)} \end{bmatrix} \tag{1.5}$$

where V is the flow velocity, and α is the skewed angle of the free streamline, changing from 0° to 90°.

One can see from (1.3) that there are three states in this model, and each has a physical meaning. They represent, respectively, uniform flow, a side-to-side gradient, and a fore-to-aft gradient. The theory was verified experimentally [4]. At present, it is used in virtually every stability and handling quality application. The limitation for the Pitt-Peters model is that it is a low-order approximation to the rotor induced flow field with only one harmonic and one radial shape function for each harmonic. Thus, the model is only the crudest wake description of uniform flow since it lacks higher-harmonic terms of the flow field.

Due to the limitation of the Pitt-Peters model, researchers desired a higher-harmonic theory which could be more accurate. In 1987, David Peters and Chengjian He developed a higher-harmonic theory, which is known as the Peters-He generalized dynamic wake model [5, 6]. The

pressure distribution for the Peters-He model was extended from Pitt's pressure distribution to include higher harmonic terms and arbitrary number of radial functions for each harmonic

$$P = -\frac{1}{2}\sum_{m=0}^{\infty}\sum_{n=m+1,m+3,\cdots}^{\infty} \bar{P}_n^m(v)\bar{Q}_n^m(i\eta)\Big[\tau_n^{mc}\cos(m\bar{\psi})+\tau_n^{ms}\sin(m\bar{\psi})\Big]$$ (1.6)

The inflow distribution is expanded to include an arbitrary number of harmonics and radial functions, which is similar as the expression of the pressure

$$v_z = \sum_{m=0}^{\infty}\sum_{n=m+1,m+3,\cdots}^{\infty} \frac{\bar{P}_n^m(v)}{v}\Big[\alpha_n^m\cos(m\bar{\psi})+\beta_n^m\sin(m\bar{\psi})\Big]$$ (1.7)

where $\bar{P}_n^m(v)$ and $\bar{Q}_n^m(i\eta)$ are associated normalized Legendre functions of the first and second kind, respectively. (See Appendix 2)

Both Pitt and He began with the complete potential flow equations and then assumed "superposition of pressures," which implies that inflow modes with no induced velocity on the rotor disk are neglected. As a result, the Peters-He model takes the form

$$[M]\{\overset{+}{\alpha_n^m}\}+V\Big[\tilde{L}^c\Big]^{-1}\{\alpha_n^m\} = \frac{1}{2}\{\tau_n^{mc}\}$$ (1.8)

$$[M]\{\overset{+}{\beta_n^m}\}+V\Big[\tilde{L}^s\Big]^{-1}\{\beta_n^m\} = \frac{1}{2}\{\tau_n^{ms}\}$$ (1.9)

where $\{\alpha_n^m\}$ and $\{\beta_n^m\}$ are the coefficients of the axial induced velocity component on the disk, and $\{\tau_n^{mc}\}$ and $\{\tau_n^{ms}\}$ represent cosine and sine pressure coefficients. The matrix $[M]$ is the apparent mass matrix; and $\Big[\tilde{L}^c\Big]$ and $\Big[\tilde{L}^s\Big]$ are the cosine and sine influence coefficient matrices,

respectively. These are all given in closed form. The Peters-He model is widely used in many production codes including FLIGHTLAB (Advanced Rotorcraft Technology), COPTER (Bell Helicopter), RCAS (U. S. Government) and ONERA-DFVLR (European Community), etc, as in [7].

The Peters-He model expands the flow in terms of Legendre functions, because they are the natural solution to Laplace's Equation with a discontinuity at a circular disk. However, the Peters-He model contains only Legendre functions that have $m+n=odd$ (where m is the harmonic number and n is a radial expansion number). The functions with $m + n$ odd represent pressure discontinuities at the disk. As the result of discarding the $m+n=even$ terms, which are related to mass-sources, the Peters-He model cannot describe the inflow distribution caused by mass-injection. Even more important, however, is the fact that the neglect of the even terms precludes computation of the flow off the disk (as was learned in latter research). Thus, the Peters-He model treats only the normal component of flow on the rotor disk.

Subsequent researchers have attempted to extend the Peters-He model to include all components of flow throughout the field. In 1996, Wen-Ming Cao and David Peters [8] made an attempt to compute the flow off of the rotor disk as well as on the disk. This work demonstrated that there must be a second set of wake states (besides the He states) for flow off the rotor to be calculated; but it was not known what these states should be.

In 2001, Jorge Morillo and David Peters [6] addressed these issues and showed that the extra states could be found rigorously (with no need for the limiting assumption of superposition of pressures) by writing the velocity field as a gradient of velocity potentials and by including the

6

mass source terms in the expansions, so that the $m+n=odd$ terms and $m+n=even$ terms are all included in the model,

$$P = -\sum_{m=0}^{\infty} \sum_{n=m+1}^{\infty} \left[\tau_n^{mc} \Phi_n^{mc} + \tau_n^{ms} \Phi_n^{ms} \right]$$

(1.10)

$$\vec{v} = \sum_{m=0}^{\infty} \sum_{n=m+1}^{\infty} \left[\hat{a}_n^m \vec{\nabla} \Psi_n^{mc} + \hat{b}_n^m \vec{\nabla} \Psi_n^{ms} \right]$$

(1.11)

where Φ_n^m and Ψ_n^m are the pressure and velocity potentials. This set of functions was also used by Pitt and He, but they only considered the odd functions and considered them only for the normal component of velocity. With these definitions, Morillo and Peters were able to use a Galerkin approach to obtain a closed-form set of equations for all three components of the velocity potential—and thus of the velocity field everywhere in the upper hemisphere (i.e., upstream hemisphere)—including the plane of the rotor disk. The governing equations are obtained from this Galerkin procedure in closed form and take the following form:

$$\left[M^c \right]\{\overset{*}{a_n^m}\} + \left[D^c \right]\left[\tilde{L}^c \right]^{-1}\left[M^c \right]\{a_n^m\} = \left[D^c \right]\{\tau_n^{mc}\}$$

(1.12)

$$\left[M^s \right]\{\overset{*}{b_n^m}\} + \left[D^s \right]\left[\tilde{L}^s \right]^{-1}\left[M^s \right]\{b_n^m\} = \left[D^s \right]\{\tau_n^{ms}\}$$

(1.13)

where $\left[D \right]$ is the damping matrix. All matrices are in closed form, and mass sources are also allowed. The Peters-Morillo model gave excellent agreement with a class of closed-form solutions for step response and frequency response above the rotor disk, but convergence was slow due to ill-conditioned matrices. However, the Peters-Morillo model could not treat non-zero flux mass sources, which are the fundamental mass-source terms (the terms with $m=n$).

7

In 2005, Yu and Peters [9] tried to develop an improved state-space representation that included the non-zero mass flux forcing terms. They extended the $[D]$ matrix in the right-hand side to incorporate the mass source terms into the governing equation

$$\left[M^c\right]\{\overset{*}{a_n^m}\}+\left(\left[D^c\right]\cos\chi-\left[C^c\right]\sin\chi\right)\{a_n^m\}=\left[\bar{D}^c\right]\{\tau_n^{mc}\} \tag{1.14}$$

where $[C]$ is a secondary damping matrix, χ is the inflow angle, and $[\bar{D}]$ is the extended matrix. However, they were unable to find the potential functions for $m=n$ and, consequently, still had not added the missing states. Despite the extended $[D]$ matrix, the model remained ill-conditioned and converged slowly.

Hsieh and Peters [10] found the here-to-fore illusive potential functions for $m=n$. The special case $m=n=0$ still involved a singularity, but they replaced the infinite integral with an approximate solution for the infinite kinetic energy that converges as the number of terms is increased. Later, Garcia-Duffy and Peters [11] incorporated these into a complete dynamic inflow model for all components of flow in the upper hemisphere—and with good convergence. This model with the $m=n$ term will be referred to as the Hsieh/Duffy model. All of these models are only valid for the flow on or above the plane of the rotor disk. What remains, then, is to find a solution for the flow below the plane of the rotor, and apply the new method to finite blade systems and find the inflow within the wake region.

Recently, Fei [12, 13] extended Hsieh/Duffy model and found a rigorous solution for the flow below the plane of the rotor, which allows application of finite-state methods within the rotor wake—giving the entire velocity field at all points. The ability to find the flow field everywhere

impacts not only rotor flight simulation but also wind energy applications, as in [14]. It also allows treatment of multi-rotor systems for which the induced flow from one rotor impinges upon another. The cost of finding flow below the disk is that one must also compute the adjoint of the velocity (i.e., the co-states of the flow). Once that is done, the complete flow below the plane follows directly. The co-state method insures that the flow below the disk converges at least as well as the flow above the disk. The adjoint methodology has been validated for both step response and frequency response throughout the range of skew angles. It is interesting to note that the three-dimensional inflow model has an analog in two-dimensional flow and can be applied to airfoil theory, as in [15]. This has also led to applications to the locomotion of organisms by the above finite-state methodology, as in [16].

For the helicopter at the hover condition, the linearized equations will become singular when V_∞ goes to 0. Peters, Hsieh, and Garcia-Duffy [11] described an approximate method whereby the equations could be extended to the nonlinear case; but the method is not generally valid. Here, the correct formulation will be demonstrated.

1.3 Approach

In this thesis, the Nowak-He and Huang-He inflow model will be shown to be related through a simple change of variable. This implies that one can compute both sets of states from a single set of unified, state-variable equations. By the blending of the two solutions, the axial component of velocity can be greatly improved as compared with the existing Morillo-Duffy inflow model and Nowak-He inflow model. For the x and y components of the induced velocity (in-plane), the Morillo-Duffy solution and the Huang-He solution can be similarly blended. The adjoint theorem is then employed to formulate both the induced velocity below the rotor disk and the induced velocity downstream. This theorem is extended to compute the flow downstream as

the wake skew angle becomes small. Finally, appropriate nonlinearities will be added to allow the model to be effective even down to hover, including the effects of wake contraction and wake skew.

Chapter 2: Solution Details

2.1 Fluid Dynamics Equations

The governing equations for Newtonian fluid are based on the basic conservation laws, which include conservation of mass, conservation of momentum, and conservation of energy. Each of the conservation laws lead to either one or a set of differential equations. Together these give the equations that describe the motion of Newtonian fluid [17]:

$$\frac{\partial \rho}{\partial t} + \vec{\nabla} \cdot \left(\rho \vec{v}_t \right) = 0 \tag{2.1}$$

$$\rho \frac{\partial \vec{v}_t}{\partial t} + \rho \left(\vec{v}_t \cdot \vec{\nabla} \right) \vec{v}_t = -\vec{\nabla} p + \vec{\nabla} \left(\bar{\lambda} \vec{\nabla} \cdot \vec{v}_t \right) + \bar{\mu} \left(\vec{\nabla} \left(\vec{\nabla} \cdot \vec{v}_t \right) + \left(\vec{\nabla} \cdot \vec{\nabla} \right) \vec{v}_t \right) + \rho \vec{f} \tag{2.2}$$

$$\rho \frac{\partial e}{\partial t} + \rho \left(\vec{v}_t \cdot \vec{\nabla} \right) e = -p \vec{\nabla} \cdot \vec{v}_t + \vec{\nabla} \left(k \vec{\nabla} T \right) + \bar{\Phi} \tag{2.3}$$

$$p = p \left(\rho, T \right) \tag{2.4}$$

$$e = e \left(\rho, T \right) \tag{2.5}$$

where ρ is the fluid density, $\vec{v}_t$ is the total velocity, p is the pressure, $\bar{\lambda}$ and $\bar{\mu}$ are the second viscosity coefficient and the dynamic viscosity respectively, $\vec{f}$ represents the external forces, e is the internal energy per unit mass, k is the thermal conductivity of the fluid, $\bar{\Phi}$ is the viscous dissipation function and T is temperature.

However, for a helicopter, it is reasonable to assume that the inflow at standard atmospheric conditions is incompressible and inviscid around the actuator disk [17]. Since there are no

11

significant body forces around an actuator disk, the equations are reduced to the following potential flow equations

$$\vec{\nabla} \cdot \vec{v}_t = 0 \qquad (2.6)$$

$$\rho \frac{\partial \vec{v}_t}{\partial t} + \rho \left(\vec{v}_t \cdot \vec{\nabla} \right) \vec{v}_t = -\vec{\nabla} p \qquad (2.7)$$

Herein, we initially consider the linearized equations written as a perturbation of velocity about the steady free-stream. (Later on, some of the nonlinearities of the model will be added back.) The steady free-stream velocity is labeled as V_∞. The total velocity is represented by

$$\vec{v}_t = V_\infty \vec{\xi} + \delta \vec{v} \qquad (2.8)$$

where $\vec{\xi}$ is a unit vector that is along the free streamline and is skewed with respect to positive z by an angel of χ as shown in Figure 2.1; and

$$\delta \vec{v} = \delta v_x \vec{i} + \delta v_y \vec{j} + \delta v_z \vec{k} \qquad (2.9)$$
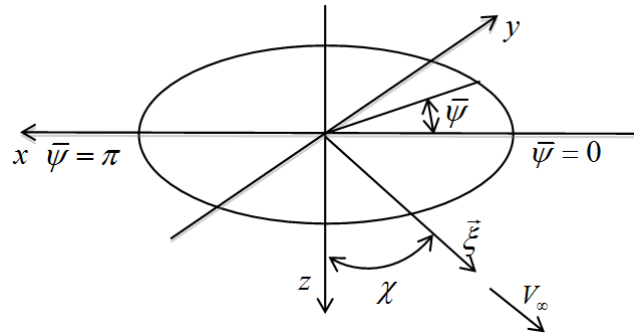
Figure 2.1 Coordinate system

Also, from the coordinates in Fig. 2.1, $\vec{\xi}$ can be expressed as

12

$$\vec{\xi} = -\sin(\chi)\vec{i} + \cos(\chi)\vec{k}$$

where $\vec{i}$, $\vec{j}$ and $\vec{k}$ are unit vectors in x, y and z directions, respectively.

Substitution of these equations into the momentum equations and continuous equation, considering that V_∞ is constant, gives the linearized equations as

$$\vec{\nabla} \cdot \delta\vec{v} = 0 \tag{2.10}$$

$$\rho \frac{\partial \delta\vec{v}}{\partial t} + \rho V_\infty \frac{\partial \delta\vec{v}}{\partial \xi} = -\vec{\nabla}p \tag{2.11}$$

To normalize the variables, all lengths are divided by the rotor radius R; and the velocities are all divided by V_∞. Therefore, Eqs. (10)-(11) can be rewritten as

$$\vec{\nabla} \cdot \vec{v} = 0 \tag{2.12}$$

$$\frac{\partial \vec{v}}{\partial \tau} + \frac{\partial \vec{v}}{\partial \xi} = -\vec{\nabla}P \tag{2.13}$$

where P is defined as normalized pressure $p/\rho V_\infty^2$, $\vec{v}$ as normalized induced velocity $\delta\vec{v}/V_\infty$ and time as a reduced time τ, which is tV_∞/R ; and where the Laplacian operator is redefined as the gradient with respect to non-dimensional coordinates. The boundary condition in the upper hemisphere is that velocity $\vec{v}$ must be zero in all directions far upstream.

Suppose $\vec{v}$ can be represented by the gradient of some function, Ψ, then it may be written as

$$\vec{v} = \vec{\nabla}\Psi \tag{2.14}$$

Then it is clear from Eq. (2.12) that Ψ will be a potential function and will satisfy Laplace's equation

$$\vec{\nabla} \cdot \vec{\nabla} \Psi = 0 \tag{2.15}$$

Substitution of this velocity potential in Eq. (2.14) into Eq. (2.13), followed by a divergence operation to the resultant equation, gives:

$$\frac{\partial \vec{\nabla} \cdot \vec{\nabla} \Psi}{\partial \tau} + \frac{\partial \vec{\nabla} \cdot \vec{\nabla} \Psi}{\partial \xi} = -\vec{\nabla} \cdot \vec{\nabla} P \tag{2.16}$$

Based on Eq. (2.15), the left hand side of Eq. (2.16) is equal to 0, so if one define

$$\Phi = P \tag{2.17}$$

Then it is known that Φ satisfies Laplace's equation

$$\vec{\nabla} \cdot \vec{\nabla} \Phi = 0 \tag{2.18}$$

which implies that Φ is also a potential function, as that is related to pressure, so it is called as pressure potential. Solution of Eqs. (2.15) or (2.18) will yield a family of functions in terms of which both Ψ and Φ may be expanded.

2.2 Elliptical Potential Functions

In order to write the equations, one expands the pressure in terms of potential functions which satisfy Laplace equations. As discontinuities in pressure only occur across the disk, it is convenient to write Laplace's equation in ellipsoidal coordinates. The solutions to Laplace's equation in these coordinates are Legendre functions of the first and second kind along with

sines and cosines. One may then reconstruct the pressures in the flow field (See in Appendix 2) as an expansion in these functions. The pressure potential can be expressed as

$$\Phi_n^{mc}\left(v,\eta,\bar{\psi}\right) = \bar{P}_n^m\left(v\right)\bar{Q}_n^m\left(i\eta\right)\cos\left(m\bar{\psi}\right) \qquad (2.19)$$

$$\Phi_n^{ms}\left(v,\eta,\bar{\psi}\right) = \bar{P}_n^m\left(v\right)\bar{Q}_n^m\left(i\eta\right)\sin\left(m\bar{\psi}\right) \qquad (2.20)$$

where v, η and $\bar{\psi}$ are the ellipsoidal coordinates defined in Appendix 1; and m takes values from $\{0,1,2,3,4,\ldots\}$ and n is from $\{m,m+1,m+2,m+3,\ldots\}$.

The values of the coefficients depend upon the boundary conditions. It is noted that the solution includes both odd terms and even terms of v, which (respectively) are capable for describing pressure discontinuities and mass injections anywhere on the rotor disk. In the plane of the rotor disk but off the disk ($v = 0$), the functions with $m+n=odd$ ($\bar{P}_n^m\left(v\right)$ are odd functions) are zero. For $m+n=even$ ($\bar{P}_n^m\left(v\right)$ are even functions), the pressure potential has normal derivatives that are zero off the disk. One can also see from Figure A1.1 that ellipsoidal coordinates take on the values $0<v<1$ above the disk while $-1<v<0$ below the disk. Since there is a jump in v across the disk, this implies a jump in Φ for the odd terms and a jump in the normal derivative of Φ for the even terms. On the disk, $\eta = 0$ such that the $m+n=odd$ potentials can be used to describe a pressure jump of the system; and $m+n=even$ potentials (which have a discontinuity in slope) can be used to represent a mass source in the flow field.

The pressure can be expanded as a summation of all the pressure potential terms as

$$P = -\sum_{m=0}^{\infty}\sum_{n=m}^{\infty}\left(\tau_n^{mc}\Phi_n^{mc} + \tau_n^{ms}\Phi_n^{ms}\right) \qquad (2.21)$$

15

The pressure drop and the injected mass across the disk can be expressed by the flowing equations

$$\Delta P = \left[P_{lower} - P_{upper} \right]\Big|_{\eta=0} = 2\sum_{m=0}^{\infty} \sum_{n=m+1,m+3,\cdots}^{\infty} \left(\tau_n^{mc} \Phi_n^{mc} + \tau_n^{ms} \Phi_n^{ms} \right)\Big|_{\eta=0} \tag{2.22}$$

$$\frac{\Delta \dot{m}}{\rho V_{\infty}} = \left[P_{lower} + P_{upper} \right]\Big|_{\eta=0} = 2\sum_{m=0}^{\infty} \sum_{n=m,m+2,\cdots}^{\infty} \left(\tau_n^{mc} \Phi_n^{mc} + \tau_n^{ms} \Phi_n^{ms} \right)\Big|_{\eta=0} \tag{2.23}$$

where ΔP is the net pressure drop across the disk going from negative to positive z, $\Delta \dot{m}$ is the net mass per unit time per unit area being injected into the flow field at the disk.

2.3 Prime Velocity Potentials

There are two useful definitions of velocity potentials. One set is defined as the prime potentials, and the other set is defined as derived potentials. In order to satisfy the upstream boundary condition of zero velocity, the prime potentials are defined as

$$\Psi_n^{mc} = \int_{-\infty}^{\xi} \Phi_n^m \cos\left(m\bar{\psi} \right) d\xi \tag{2.24}$$

$$\Psi_n^{ms} = \int_{-\infty}^{\xi} \Phi_n^m \sin\left(m\bar{\psi} \right) d\xi \tag{2.25}$$

Since $\lim_{\eta\to\infty} \bar{Q}_n^m (i\eta) = 0$, it is guaranteed that the definition of the prime potential will satisfy the boundary condition that the velocity field far upstream from the rotor is equal to zero. Then the flow velocities can be written as

$$\vec{v} = \sum_{m=0}^{\infty} \sum_{n=m}^{\infty} \left(\hat{a}_n^m \vec{\nabla} \Psi_n^{mc} + \hat{b}_n^m \vec{\nabla} \Psi_n^{ms} \right) \tag{2.26}$$

16

Substitution of Eqs. (2.24) and (2.25) into Eq. (2.26), and with note that $\hat{\Psi}_n^{mc}$, $\hat{\Psi}_n^{ms}$, Φ_n^{mc} and Φ_n^{ms} are only functions of non-dimensional coordinates and $\hat{a}_n^m$, $\hat{b}_n^m$, τ_n^{mc} (and that the τ_n^{ms} are only functions of reduced time τ) gives:

$$\sum_{m=0}^{\infty}\sum_{n=m}^{\infty}\left(\vec{\nabla}\Psi_n^{mc}\frac{\partial\hat{a}_n^m}{\partial\tau}+\vec{\nabla}\frac{\partial\Psi_n^{mc}}{\partial\xi}\hat{a}_n^m\right)=\sum_{m=0}^{\infty}\sum_{n=m}^{\infty}\left(\vec{\nabla}\Phi_n^{mc}\tau_n^{mc}\right) \tag{2.27}$$

$$\sum_{m=0}^{\infty}\sum_{n=m}^{\infty}\left(\vec{\nabla}\Psi_n^{ms}\frac{\partial\hat{b}_n^m}{\partial\tau}+\vec{\nabla}\frac{\partial\Psi_n^{ms}}{\partial\xi}\hat{b}_n^m\right)=\sum_{m=0}^{\infty}\sum_{n=m}^{\infty}\left(\vec{\nabla}\Phi_n^{ms}\tau_n^{ms}\right) \tag{2.28}$$

There are no closed-form expressions for these prime velocity potentials at arbitrary skew angles. Therefore, one must do preprocessing to integrate the gradients of Ψ_n^m at points in the flow field in order to calculate the velocity. This can be accomplished by integration of the potentials along the streamlines, which is time consuming.

The derived potentials, $\hat{\Psi}_n^m$, are defined as the prime potentials for the special case of axial flow. These can be found in closed form, and thus their use avoids any numerical integration for calculating the induced velocity components. Their disadvantage is that the ξ derivative in the potential flow equations is more complicated for these, and one must relate the derived potentials to the prime potentials through a change of variable. Peters and Morillo found the change of variable (for $m \neq n$) in the following form:

$$\hat{\Psi}_n^m = \sigma_n^m\Phi_{n+1}^m + \varsigma_n^m\Phi_{n-1}^m \tag{2.29}$$

where

$$\sigma_n^m = \frac{1}{K_n^m \sqrt{(2n+1)(2n+3)\left[(n+1)^2 - m^2\right]}} \tag{2.30}$$

$$\varsigma_n^m = \frac{1}{K_n^m \sqrt{(4n^2-1)(n^2-m^2)}} \qquad n \neq m \tag{2.31}$$

and

$$K_n^m = \left(\frac{\pi}{2}\right)^{(-1)^{n+m}} H_n^m \tag{2.32}$$

$$H_n^m = \frac{(n+m+1)!!(n-m-1)!!}{(n+m)!!(n-m)!!} \tag{2.33}$$

This definition is only valid above the rotor disk ($n > m$). For the case when $m = n \neq 0$, Peters and Hsieh developed a formulation for the potentials in terms of an alternate type of "Legendre function" with subscript greater than superscript:

$$\hat{\Psi}_m^{mc} = \left[\sigma_m^m \bar{P}_{m+1}^m(\nu)\bar{Q}_{m+1}^m(i\eta) + \bar{P}_{m-1}^m(\nu)\bar{Q}_{m-1}^m(i\eta)\right]\cos(m\bar{\psi}) \tag{2.34}$$

$$\hat{\Psi}_m^{ms} = \left[\sigma_m^m \bar{P}_{m+1}^m(\nu)\bar{Q}_{m+1}^m(i\eta) + \bar{P}_{m-1}^m(\nu)\bar{Q}_{m-1}^m(i\eta)\right]\sin(m\bar{\psi}) \tag{2.35}$$

where

$$\bar{P}_{m-1}^m(\nu) = \frac{2}{\pi} \frac{\sqrt{(2m)!!}}{\sqrt{(2m+1)!!}} \frac{\left(1-\nu^2\right)^{m/2}}{(1+\nu)^m} \sum_{n=0}^{m-1} \frac{(m-1)!2^{m-1-n}(-1)^n}{n!(m-1-n)!(n+m)}(1-\nu)^n \tag{2.36}$$

$$\bar{Q}_{m-1}^m(i\eta) = \frac{1}{\left(1+\eta^2\right)^{m/2}} \tag{2.37}$$

Even here, the case for $m = n = 0$ is singular. By solving the Laplace equation with $m = n = 0$ and then adding a line singularity (which is not obtainable by separation of variables), Peters and Hsieh were able to find the $m = n = 0$ derived velocity potential as

$$\hat{\Psi}_0^0 = \frac{2}{\pi} \nu \left[1 - \eta \tan^{-1} \left(\frac{1}{\eta} \right) \right] - \frac{2}{\pi} \ln |1 + \nu| - \frac{1}{\pi} \ln |1 + \eta^2| + \frac{2}{\pi} \ln |Z_{max}| \qquad \nu > 0 \qquad (2.38)$$

where Z_{max} is a large number representing the radius to which the ξ integral is taken. When the potential is evaluated at infinity, the last term cancels the logarithmic terms—so that the potential is zero at Z_{max}. Of course, this additional constant has no effect on the velocity field because one needs only the gradients of the potential functions to obtain velocity. This large number Z_{max} will, however, affect the Galerkin integrals to be derived in the following section so that this logarithmic constant will need to be dealt with. (Derived velocity potentials are not defined below the rotor plane.)

Because the velocity potentials all satisfy Laplace's equation, the continuity equation in Eq. (2.12) is satisfied automatically. That means it is sufficient to consider only the momentum equation as a governing equation for the velocity expansion coefficients. Thus, to obtain a finite-state wake model is equivalent to solve the problem of representing the momentum equations in finite-state form.

2.4 Galerkin Method

In order to transform the momentum equation into a set of ordinary differential equations, the Galerkin Method is adopted here in which velocities are expanded in terms of the prime potentials. (Derived potentials will be considered later.) The test functions for the Galerkin method are chosen to be the same Laplace solutions that are used as expansions for the pressure

19

potentials. Since the velocity potentials are only defined in the upper hemisphere, the integrations will be done in the upper hemisphere, and all boundary conditions are matched. As the integration is only considered over the upper hemisphere, the velocity solution will only be valid above the disk. The complications of boundary conditions on velocity inside the wake make Galerkin below the disk impractical.

After substitution of the proper expansions of pressure potentials, velocity potentials, and the expression of velocity into the momentum equation, volume integration is taken on both sides of the momentum equations. With the divergence theorem, one can then transfer the volume integral into a surface integral, which vanishes at $r \to \infty$. By the method shown in [6], the surface integral in the plane of the rotor is transformed to integrals on the rotor disk, itself, which have closed-form representations. This leads to a set of ordinary differential equations. The cosine and sine functions completely separate into two uncoupled sets during this procedure. For the cosine parts, the Galerkin method gives:

$$
\begin{bmatrix} \left[\tilde{L}^c\right]_{o,o} & \left[\tilde{L}^c\right]_{o,e} \\ \left[\tilde{L}^c\right]_{e,o} & \left[\tilde{L}^c\right]_{e,e} \end{bmatrix} \begin{Bmatrix} \left\{\overset{*}{\hat{a}}_n^m\right\}_o \\ \left\{\overset{*}{\hat{a}}_n^m\right\}_e \end{Bmatrix} + \begin{bmatrix} \left[D\right]_{o,o}^c & \left[D\right]_{o,e}^c \\ \left[D\right]_{e,o}^c & \left[D\right]_{e,e}^c \end{bmatrix} \begin{Bmatrix} \left\{\hat{a}_n^m\right\}_o \\ \left\{\hat{a}_n^m\right\}_e \end{Bmatrix} = \begin{bmatrix} \left[D\right]_{o,o}^c & \left[D\right]_{o,e}^c \\ \left[D\right]_{e,o}^c & \left[D\right]_{e,e}^c \end{bmatrix} \begin{Bmatrix} \left\{\tau_n^{mc}\right\}_o \\ \left\{\tau_n^{mc}\right\}_e \end{Bmatrix} \tag{2.39}
$$

where

$$
\left[\tilde{L}^c\right] = \left[\iint_s \frac{\partial \Phi_j^{rc}}{\partial z}\left(\int_0^\infty \Phi_n^{mc} d\xi\right) ds\right] = \left[\iint_s \Phi_j^{rc} \frac{\partial}{\partial z}\left(\int_0^\infty \Phi_n^{mc} d\xi\right) ds\right] \tag{2.40}
$$

$$
\left[D^c\right] = \left[\iint_s \frac{\partial \Phi_j^{rc}}{\partial z} \Phi_n^{mc} ds\right] = \left[\iint_s \Phi_j^{rc} \frac{\partial \Phi_n^{mc}}{\partial z} ds\right] \tag{2.41}
$$

The sine components are similar to Eq. (2.39). Note that the subscript notation "o" stands for the terms with $m+n=odd$ and "e" is for the terms with $m+n=even$. For the cosine terms, $m=0,1,2,3,...$ and for the sine terms $m=1,2,3,...$, since

$$\Phi_n^{ms} = \bar{P}_n^{ms}(v)\bar{Q}_n^{ms}(i\eta)\sin(m\bar{\gamma}) \tag{2.42}$$

which implies that when $m=0$, $\Phi_n^{ms}=0$. In either the case of sine terms or cosine terms, $n=m,m+2,m+4,...$ or $n=m+1,m+3,m+5,...$ depending on the subscript of the partition is "e" or "o".

The $[D]$ matrix is as follows for both cosine and sine case:

$$D_{jn}^{rm} = \frac{1}{K_n^m}\delta_{jn}\delta_{rm}$$
$$j+r=odd; \qquad n+m=odd$$
$$j+r=even; \qquad n+m=even \tag{2.43}$$

$$D_{jn}^{rm} = \frac{2\delta_{nm}}{\pi\sqrt{H_n^m H_j^m}}\frac{\sqrt{(2j+1)(2n+1)}}{(j+n+1)(j-n)}(-1)^{\frac{j+3n-1}{2}}$$
$$j+r=odd; \qquad n+m=even$$
$$j+r=even; \qquad n+m=odd \tag{2.44}$$

And the $[\tilde{L}]$ matrix is given by

$$\left[\tilde{L}_{jn}^{0m}\right]^c = X^m\Gamma_{jn}^{0m} \tag{2.45}$$

$$\left[\tilde{L}_{jn}^{rm}\right]^c = \left[X^{|m-r|}+(-1)^l X^{|m-r|}\right]\Gamma_{jn}^{rm} \tag{2.46}$$

21

$$\left[\tilde{L}_{jn}^{rm}\right]^{s} = \left[X^{|m-r|} - (-1)^{l} X^{|m-r|}\right]\Gamma_{jn}^{rm} \tag{2.47}$$

where

$$X = \tan(\chi/2), \qquad l = \min(r, m) \tag{2.48}$$

$$\Gamma_{jn}^{rm} = \frac{sign(r-m)}{\sqrt{K_n^m K_j^r}\sqrt{(2n+1)(2j+1)}}\delta_{j,n\pm 1}$$

$$r+m=odd; \qquad j+r=odd; \qquad n+m=odd \tag{2.49}$$
$$r+m=odd; \qquad j+r=even; \qquad n+m=even$$

$$\Gamma_{jn}^{rm} = \frac{(-1)^{\frac{n+j-2r}{2}}(2)\sqrt{(2n+1)(2j+1)}}{\sqrt{H_n^m H_j^r}(n+j)(n+j+2)\left[(n-j)^2-1\right]}$$

$$r+m=even; \qquad j+r=odd; \qquad n+m=odd \tag{2.50}$$

$$\Gamma_{jn}^{rm} = \frac{(-1)^{\frac{n+j-2r+2}{2}}(8)\sqrt{(2n+1)(2j+1)}}{\pi^2\sqrt{H_n^m H_j^r}(n+j)(n+j+2)\left[(n-j)^2-1\right]}$$

$$r+m=even; \qquad j+r=even; \qquad n+m=even \tag{2.51}$$

$$\Gamma_{jn}^{rm} = \frac{(-1)^{\frac{3n+j+2m-2r}{2}}(4)sign(r-m)\sqrt{(2n+1)(2j+1)}}{\pi\sqrt{H_n^m H_j^r}(n+j)(n+j+2)\left[(n-j)^2-1\right]}$$

$$r+m=odd; \qquad j+r=odd; \qquad n+m=even \tag{2.52}$$
$$r+m=odd; \qquad j+r=even; \qquad n+m=odd$$

$$\Gamma_{jn}^{rm} = \frac{1}{\sqrt{H_n^m H_j^r}\sqrt{(2n+1)(2j+1)}}\delta_{j,n\pm 1}$$

$$j+m=even; \qquad j+r=odd; \qquad n+m=even \tag{2.53}$$
$$j+m=even; \qquad j+r=even; \qquad n+m=odd$$

The potential for $m = n = 0$, has a logarithmic term, so the integral for Γ is formally infinite for the case of $m = r = n = j = 0$. However, based on [5], this integral can be expressed as a finite series that approaches infinity as the number of terms approaches infinity.

$$\Gamma_{00}^{00} = \left(\frac{4}{\pi^2} \sum_{n=1}^{N_{\max}} \frac{1}{n} \right) + \frac{1}{2} \tag{2.54}$$

where $N_{\max}$ is the largest harmonic number. In this way, the integral is finite for a truncated approximation. This also allows a solution with a finite number of terms that provides formal convergence to the exact answer.

2.5 Derived Potentials

In the previous section, a closed form representation of the dynamic equations is shown for the velocity potential expansions in terms of prime potentials. However, to overcome the limitations of prime potential, the velocity can be written in terms of derived potentials. In order to do this, one needs to relate the variables which define the two sets of basic functions over the upper hemisphere. In particular, the total velocity potential is written as

$$\left\{ \hat{a}_n^m \right\}^T \left[\Psi_n^{mc} \right] = \left\{ a_n^m \right\}^T \left\{ \sigma_n^m \Phi_{n+1}^{mc} + \varsigma_n^m \Phi_{n-1}^{mc} \right\} \tag{2.55}$$

When a Galerkin approach is applied to Eq. (2.55), then the following relationship is found

$$\left\{ \hat{a}_n^m \right\} = \left[\tilde{L}^c \right]^{-1} \left[M^c \right] \left\{ a_n^m \right\} \tag{2.56}$$

where

$$\left[M^c \right] = \left[\tilde{L}^c \right]_{\chi=0} = \left[\iint_s \frac{\partial \Phi_j^{rc}}{\partial z} \Psi_n^{mc} ds \right] \tag{2.57}$$

A similar transformation therefore exists between $\{\hat{b}_n^m\}$ and $\{b_n^m\}$ that involves $\left[L^s\right]$ and $\left[M^s\right]$, which relates to sine coefficients. With this transformation of variables, the equation of motion for a skewed flow becomes

$$\left[M^c\right]\left\{\overset{*}{a}_n^m\right\}+\left[D^c\right]\left[L^c\right]^{-1}\left[M^c\right]\left\{a_n^m\right\}=\left[D^c\right]\left\{\tau_n^{mc}\right\} \tag{2.58}$$

The equation in Eq. (2.58) is a closed form expression for all components of the velocity above and on the rotor plane.

For the special case of axial flow ($\chi = 0$), $\left[\tilde{L}^c\right]$ and $\left[M^c\right]$ are equivalent. Therefore, the momentum equation can be simplified as

$$\left[M^c\right]\left\{\overset{*}{a}_n^m\right\}+\left[D^c\right]\left\{a_n^m\right\}=\left[D^c\right]\left\{\tau_n^{mc}\right\} \tag{2.59}$$

Chapter 3: Linear Extensions of the Morillo-Duffy Model

3.1 Flow below Disk by Adjoint Theorem

One of the disadvantages of the Morillo-Duffy Model is that, because it is based on a Galerkin method, it only gives velocity in the hemisphere that includes the rotor plane and upstream of that plane. A Galerkin method for flow below the plane of the rotor disk (which would include inside of the rotor wake) is out of the question because the boundary conditions within the wake are too complicated to allow simple Galerkin shape functions. In fact, strictly speaking, the flow below the rotor wake and inside the wake is not potential flow. There are vortex sheets in the wake; and, although the flow is potential between the sheets, the entire flow field is not irrotational.

In this chapter, a way around this difficulty is offered by noting that, although the flow is not potential flow in the wake, in nonetheless satisfies the continuity and momentum equations. Thus, this opens the door for perhaps a way to utilize the solution above the disk to find the solution below the disk plane. The approach is to find a closed-form solution for flow below the disk in the frequency domain and then to use Fourier Transform arguments to convert this into a general solution. As it will be shown shortly, this will involve the adjoint variables of the system.

3.1.1 Exact Solution of Frequency Response

The linearized potential flow equations can be written in non-dimensional form as:

$$\frac{\partial \vec{v}}{\partial \tau} + \frac{\partial \vec{v}}{\partial \xi} = -\vec{\nabla} P \qquad (3.1)$$

25

where Eq. (3.1) is the momentum equation, $\vec{v}$ is the local induced velocity vector, τ is non-dimensional reduced time, ξ is the stream-wise direction (positive downstream), and P is the pressure field. It is assumed that the velocities are expressed as the gradient of a potential function, thus ensuring continuity. The derivation here is to show that, if one knows the velocity field in the upper hemisphere $\xi < 0$ (i.e., by the method of the previous chapter) then the velocity in the lower hemisphere can be found, $\xi > 0$. The derivation for the case of frequency response will first be introduced, and then Fourier Transform arguments will be used to extend the solution to the general time domain.

The solution for simple harmonic excitation is found from a complex harmonic balance applied to the momentum equation. The velocity is expressed as the real part of a complex quantity.

$$\vec{v}(x,y,z,\tau) = \vec{\upsilon}(x,y,z)e^{i\omega\tau} \tag{3.2}$$

where $\vec{\upsilon}(x,y,z)$ is a complex number and it is implicitly assumed that one takes only the real part of the right-hand side. Further assume that the complex pressure field P can be written as the summation of terms that includes both pressure discontinuities and mass injections:

$$P(x,y,z,\tau) = -\sum_{m=0}^{\infty}\sum_{n=m}^{\infty}\left[\tau_n^m\Phi_n^m(\nu,\eta,\bar{\psi})\right]e^{i\omega\tau} = \bar{P}e^{i\omega\tau} \tag{3.3}$$

where Φ_n^m are a complete set of potential functions with discontinuities across the disk, and terms with $m+n$ odd represent pressure discontinues across the disk and terms with $m+n$ even represent mass sources at the disk.

To obtain a closed-form frequency response, one can expand $\vec{\upsilon}$ into real and imaginary parts.

$$\vec{\upsilon}(x, y, z) = \vec{u}(x, y, z) + i\vec{w}(x, y, z) \tag{3.4}$$

Substitution of Eqs. (3.2) and (3.4) into Eq. (3.1) gives

$$i\omega\left[\vec{u}(x, y, z) + i\vec{w}(x, y, z)\right] + \left[\frac{\partial \vec{u}(x, y, z)}{\partial \xi} + i\frac{\partial \vec{w}(x, y, z)}{\partial \xi}\right] = -\vec{\nabla}\overline{P} \tag{3.5}$$

One can collect the real and imaginary parts of the equation to give expressions for the real and imaginary parts of the flow.

$$-\omega\vec{w} + \frac{\partial \vec{u}}{\partial \xi} = -\vec{\nabla}\overline{P} \tag{3.6}$$

$$\omega\vec{u} + \frac{\partial \vec{w}}{\partial \xi} = 0 \tag{3.7}$$

Solving for $\vec{u}$ from Eq. (3.7) and substituting it back into Eq. (3.6), it gives

$$\frac{\partial^2 \vec{w}}{\partial \xi^2} + \omega^2 \vec{w} = \omega\vec{\nabla}\overline{P} \tag{3.8}$$

Similarly, solving for $\vec{w}$ from Eq. (3.6) and substituting it back into the derivative of Eq. (3.7) gives

$$\frac{\partial^2 \vec{u}}{\partial \xi^2} + \omega^2 \vec{u} = -\frac{\partial}{\partial \xi}\vec{\nabla}\overline{P} \tag{3.9}$$

A Laplace transform in ξ of Eqs. (3.8) and (3.9) yields

27

$$\vec{U}(s) = -\frac{s}{s^2 + \omega^2}\vec{\nabla}\bar{P}(s) \tag{3.10}$$

$$\vec{W}(s) = \frac{\omega}{s^2 + \omega^2}\vec{\nabla}\bar{P}(s) \tag{3.11}$$

where $\vec{W}(s)$ is the Laplace transform of $\vec{w}$, $\vec{U}(s)$ is the Laplace transform of $\vec{u}$ and $\vec{\nabla}\bar{P}(s)$ is the Laplace transform of $\vec{\nabla}\bar{P}$.

Based on the convolution inverse of a Laplace transformation, the exact solution can be obtained

$$\begin{aligned}
\vec{u}(\omega, x_0, y_0, \xi_0) &= -\int_{-\infty}^{\xi_0}\cos\left[\omega(\xi_0 - \xi)\right]\vec{\nabla}\bar{P}(\xi)d\xi \\
\vec{w}(\omega, x_0, y_0, \xi_0) &= \int_{-\infty}^{\xi_0}\sin\left[\omega(\xi_0 - \xi)\right]\vec{\nabla}\bar{P}(\xi)d\xi
\end{aligned} \tag{3.12}$$

Note that the only boundary condition on the flow is that the flow approach zero far upstream ($\xi = -\infty$). Thus, the lower limits are set at $-\infty$. The physical meaning of Eq. (3.12) is that, to obtain the exact solution, one must integrate the gradient of the pressure field along a streamline from far upstream down to the point within the flow field for which that component of velocity is desired. For the real part of the flow, the integral includes the kernel $\cos\left[\omega(\xi_0 - \xi)\right]$, and for the imaginary part it includes the kernel $\sin\left[\omega(\xi_0 - \xi)\right]$. Note that, for axial flow, $\xi = z$.

The above approach is not tractable for use in practical rotor calculations. However, it is useful both as a way to determine an "exact" numerical solution against which to compare finite-state solutions (and this has been done in previous work) and as the theoretical basis for an exact

28

time-domain solution. Thus, the utility of Eq. (3.12) is in its usefulness in a proof of how to find the flow below the disk, as will be outlined below.

3.1.2 Velocity below Disk

Assume that the solution of the frequency response outlined above which is obtained by some method (such as the finite-state method) is known to be valid in the upper hemisphere. The next step is to show how that solution can be used to find the solution for the complex velocity in the lower hemisphere. In order to simplify the derivation to follow, one define the following quantities for $-\infty < \xi_0 < 0$. (Thus, they are defined only above the disk.)

$$
\begin{aligned}
\vec{C}(\omega, x_0, y_0, \xi_0) &\equiv -\int_{-\infty}^{\xi_0} \cos(\omega\xi) \vec{\nabla} \overline{P}(\xi) d\xi \\
\vec{S}(\omega, x_0, y_0, \xi_0) &\equiv -\int_{-\infty}^{\xi_0} \sin(\omega\xi) \vec{\nabla} \overline{P}(\xi) d\xi
\end{aligned}
\tag{3.13}
$$

Not that, for the special case $\tau_j^r = 1$, and all other $m \neq r, n \neq j$, $\tau_n^m = 0$, one can write from Eq. (3.13) with no loss of generality.

$$
\begin{aligned}
\vec{C}(\omega, r_0, \overline{\psi}_0, \xi_0) &= \vec{C}(\omega, x_0, y_0, \xi_0) \equiv -\int_{-\infty}^{\xi_0} \cos(\omega\xi) \vec{\nabla} \Phi_j^r(\xi) d\xi \\
\vec{S}(\omega, r_0, \overline{\psi}_0, \xi_0) &= \vec{S}(\omega, x_0, y_0, \xi_0) \equiv -\int_{-\infty}^{\xi_0} \sin(\omega\xi) \vec{\nabla} \Phi_j^r(\xi) d\xi
\end{aligned}
\tag{3.14}
$$

where $x_0 = -r_0 \cos\overline{\psi}_0$ and $y_0 = r_0 \sin\overline{\psi}_0$. We rewrite $\vec{u}(\omega, x_0, y_0, \xi_0)$ and $\vec{w}(\omega, x_0, y_0, \xi_0)$ as

$$
\begin{aligned}
\vec{u}(\omega, r_0, \overline{\psi}_0, \xi_0) &= -\cos(\omega\xi_0)\int_{-\infty}^{\xi_0} \cos(\omega\xi)\vec{\nabla}\overline{P}(\xi)d\xi - \sin(\omega\xi_0)\int_{-\infty}^{\xi_0}\sin(\omega\xi)\vec{\nabla}\overline{P}(\xi)d\xi \\
&= \cos(\omega\xi_0)\vec{C}(\omega, x_0, y_0, \xi_0) + \sin(\omega\xi_0)\vec{S}(\omega, x_0, y_0, \xi_0) \\
\vec{w}(\omega, r_0, \overline{\psi}_0, \xi_0) &= \sin(\omega\xi_0)\int_{-\infty}^{\xi_0} \cos(\omega\xi)\vec{\nabla}\overline{P}(\xi)d\xi - \cos(\omega\xi_0)\int_{-\infty}^{\xi_0}\sin(\omega\xi)\vec{\nabla}\overline{P}(\xi)d\xi \\
&= -\sin(\omega\xi_0)C(\omega, x_0, y_0, \xi_0) + \cos(\omega\xi_0)S(\omega, x_0, y_0, \xi_0)
\end{aligned}
\tag{3.15}
$$

The induced velocity above the disk is then

29

$$\vec{v}\left(r_0,\bar{\psi}_0,\xi_0,\tau\right)=\vec{u}\left(\omega,r_0,\bar{\psi}_0,\xi_0\right)\cos\left(\omega\tau\right)-\vec{w}\left(\omega,r_0,\bar{\psi}_0,\xi_0\right)\sin\left(\omega\tau\right)$$
$$=\cos\left(\omega\xi_0\right)\vec{C}\left(\omega,r_0,\bar{\psi}_0,\xi_0\right)\cos\left(\omega\tau\right)+\sin\left(\omega\xi_0\right)\vec{S}\left(\omega,r_0,\bar{\psi}_0,\xi_0\right)\cos\left(\omega\tau\right)$$
$$+\sin\left(\omega\xi_0\right)\vec{C}\left(\omega,r_0,\bar{\psi}_0,\xi_0\right)\sin\left(\omega\tau\right)$$
$$-\cos\left(\omega\xi_0\right)\vec{S}\left(\omega,r_0,\bar{\psi}_0,\xi_0\right)\sin\left(\omega\tau\right)$$

(3.16)

which is equivalent to

$$\vec{v}\left(r_0,\bar{\psi}_0,\xi_0,\tau\right)=\cos\left[\omega\left(\tau-\xi_0\right)\right]\vec{C}\left(\omega,r_0,\bar{\psi}_0,\xi_0\right)-\sin\left[\omega\left(\tau-\xi_0\right)\right]\vec{S}\left(\omega,r_0,\bar{\psi}_0,\xi_0\right)$$

(3.17)

In preparation for the solution of the flow below the disk, one need to compute $\vec{C}$ and $\vec{S}$ from the finite-state solution above the disk. Since the Morillo states are complex for a frequency response, they are broken into real and imaginary parts $\bar{a}_n^m$ and $\bar{b}_n^m$. This gives:

$$\vec{u}\left(\omega,r_0,\bar{\psi}_0,\xi_0\right)=\sum_{m=0}^{\infty}\sum_{n=m}^{\infty}\bar{a}_n^m\vec{\nabla}\hat{\Psi}_n^m\left(\nu,\eta,\bar{\psi}\right)$$
$$=\cos\left(\omega\xi_0\right)\vec{C}\left(\omega,r_0,\bar{\psi}_0,\xi_0\right)+\sin\left(\omega\xi_0\right)\vec{S}\left(\omega,r_0,\bar{\psi}_0,\xi_0\right)$$
$$\vec{w}\left(\omega,r_0,\bar{\psi}_0,\xi_0\right)=\sum_{m=0}^{\infty}\sum_{n=m}^{\infty}\bar{b}_n^m\vec{\nabla}\hat{\Psi}_n^m\left(\nu,\eta,\bar{\psi}\right)$$
$$=-\sin\left(\omega\xi_0\right)\vec{C}\left(\omega,r_0,\bar{\psi}_0,\xi_0\right)+\cos\left(\omega\xi_0\right)\vec{S}\left(\omega,r_0,\bar{\psi}_0,\xi_0\right)$$

(3.18)

where $\nu,\eta,\bar{\psi}$ is the ellipsoidal coordinate location of $r_0,\bar{\psi}_0,\xi_0$; and $\hat{\Psi}_n^m$ is the derived Morillo velocity potential.

Therefore, Eq. (3.18) allows us to express the $\vec{C}$ and $\vec{S}$ integrals in terms of the known finite-state result.

$$\vec{C}\left(\omega, r_0, \bar{\psi}_0, \xi_0\right) = \sum_{m=0}^{\infty} \sum_{n=m}^{\infty} \bar{a}_n^m \cos\left(\omega\xi_0\right) \vec{\nabla}\hat{\Psi}_n^m\left(v, \eta, \bar{\psi}\right) - \sum_{m=0}^{\infty} \sum_{n=m}^{\infty} \bar{b}_n^m \sin\left(\omega\xi_0\right) \vec{\nabla}\hat{\Psi}_n^m\left(v, \eta, \bar{\psi}\right)$$

$$\vec{S}\left(\omega, r_0, \bar{\psi}_0, \xi_0\right) = \sum_{m=0}^{\infty} \sum_{n=m}^{\infty} \bar{a}_n^m \sin\left(\omega\xi_0\right) \vec{\nabla}\hat{\Psi}_n^m\left(v, \eta, \bar{\psi}\right) + \sum_{m=0}^{\infty} \sum_{n=m}^{\infty} \bar{b}_n^m \cos\left(\omega\xi_0\right) \vec{\nabla}\hat{\Psi}_n^m\left(v, \eta, \bar{\psi}\right)$$

(3.19)

The above are valid above the disk plane which is for $-\infty < \xi_0 < 0$. However, below the disk, where $\xi_0 > 0$, one must integrate Eq. (3.14) from upstream down to the disk of the rotor plane and then below the plane. For simplicity, we will assume the single term $P = -\Phi_j^r$, where $\Phi_j^r = \bar{P}_j^r\left(v\right)\bar{Q}_j^r\left(i\eta\right)\cos\left(r\bar{\psi}\right)$. Since any pressure can be represented as a sum of these, as in Eq. (3.3), this assumption poses no restriction on generality. The below-plane result is:

$$\vec{u}\left(\omega, r_0, \bar{\psi}_0, \xi_0\right)$$
$$= \int_{-\infty}^{\xi_0} \cos\left[\omega\left(\xi_0 - \xi\right)\right] \vec{\nabla}\Phi_j^r\left(\xi\right) d\xi$$
$$= \cos\left(\omega\xi_0\right) \int_{-\infty}^{0} \cos\left(\omega\xi\right) \vec{\nabla}\Phi_j^r\left(\xi\right) d\xi + \sin\left(\omega\tilde{\xi}_0\right) \int_{-\infty}^{0} \sin\left(\omega\xi\right) \vec{\nabla}\Phi_j^r\left(\xi\right) d\xi$$
$$\quad + \cos\left(\omega\xi_0\right) \int_{0}^{\xi_0} \cos\left(\omega\xi\right) \vec{\nabla}\Phi_j^r\left(\xi\right) d\xi + \sin\left(\omega\tilde{\xi}_0\right) \int_{0}^{\xi_0} \sin\left(\omega\xi\right) \vec{\nabla}\Phi_j^r\left(\xi\right) d\xi$$
$$= \cos\left(\omega\xi_0\right) \vec{C}\left(\omega, r_0, \bar{\psi}_0, 0\right) + \sin\left(\omega\xi_0\right) \vec{S}\left(\omega, r_0, \bar{\psi}_0, 0\right)$$
$$\quad + \cos\left(\omega\xi_0\right) \int_{0}^{\xi_0} \cos\left(\omega\xi\right) \vec{\nabla}\Phi_j^r\left(\xi\right) d\xi + \sin\left(\omega\xi_0\right) \int_{0}^{\xi_0} \sin\left(\omega\xi\right) \vec{\nabla}\Phi_j^r\left(\xi\right) d\xi$$

$$\vec{w}\left(\omega, r_0, \bar{\psi}_0, \xi_0\right)$$
$$= -\int_{-\infty}^{\xi_0} \sin\left[\omega\left(\xi_0 - \xi\right)\right] \vec{\nabla}\Phi_j^r\left(\xi\right) d\xi$$
$$= -\sin\left(\omega\xi_0\right) \int_{-\infty}^{0} \cos\left(\omega\xi\right) \vec{\nabla}\Phi_j^r\left(\xi\right) d\xi + \cos\left(\omega\xi_0\right) \int_{-\infty}^{0} \sin\left(\omega\xi\right) \vec{\nabla}\Phi_j^r\left(\xi\right) d\xi$$
$$\quad - \sin\left(\omega\xi_0\right) \int_{0}^{\xi_0} \cos\left(\omega\xi\right) \vec{\nabla}\Phi_j^r\left(\xi\right) d\xi + \cos\left(\omega\xi_0\right) \int_{0}^{\xi_0} \sin\left(\omega\xi\right) \vec{\nabla}\Phi_j^r\left(\xi\right) d\xi$$
$$= -\sin\left(\omega\xi_0\right) \vec{C}\left(\omega, r_0, \bar{\psi}_0, 0\right) + \cos\left(\omega\xi_0\right) \vec{S}\left(\omega, r_0, \bar{\psi}_0, 0\right)$$
$$\quad - \sin\left(\omega\xi_0\right) \int_{0}^{\xi_0} \cos\left(\omega\xi\right) \vec{\nabla}\Phi_j^r\left(\xi\right) d\xi + \cos\left(\omega\xi_0\right) \int_{0}^{\xi_0} \sin\left(\omega\xi\right) \vec{\nabla}\Phi_j^r\left(\xi\right) d\xi$$

(3.20)

where the integrals are broken into two parts: one from downstream infinity to the disk, and one from the disk to the desired point below the disk. However, due to the symmetries in the system, the integral segments below the disk can be written in terms of integral segments above the disk. Thus, for $\xi_0 > 0$:

$$
\begin{aligned}
\int_0^{\xi_0} \cos(\omega\xi)\vec{\nabla}\Phi_j^r(\xi)d\xi &= (-1)^{j+1}\int_{-\xi_0}^0 \cos(\omega\xi)\vec{\nabla}\Phi_j^r(\xi)d\xi \\
&= (-1)^{j+1}\left[\vec{C}(\omega,r_0,\tilde{\psi}_0,0) - \vec{C}(\omega,r_0,\tilde{\psi}_0,-\xi_0)\right] \\
\int_0^{\xi_0} \sin(\omega\xi)\vec{\nabla}\Phi_j^r(\xi)d\xi &= (-1)^{j}\int_{-\xi_0}^0 \sin(\omega\xi)\vec{\nabla}\Phi_j^r(\xi)d\xi \\
&= (-1)^{j}\left[\vec{S}(\omega,r_0,\tilde{\psi}_0,0) - \vec{S}(\omega,r_0,\tilde{\psi}_0,-\xi_0)\right]
\end{aligned}
\tag{3.21}
$$

The reasons for the form of Eq. (3.21) are as follows. First, with the exception of sign, the downstream streamline emanating from $r_0,\bar{\psi}_0$ is identical in functionality to the upstream streamline emanating from $r_0,\tilde{\psi}_0$ (where $\tilde{\psi}_0 = \bar{\psi}_0 + \pi$). The differences in sign are due to the following:

a) For $r+j$ odd, the pressure potential is of opposite sign above and below the disk, whereas the gradient of pressure is the same sign above and below the disk. For $r+j$ even, the opposite is true. Since the integrals involve gradient of pressure, there is a factor of $(-1)^{r+j+1}$.
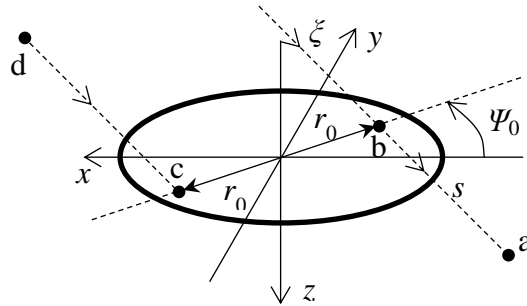

Figure 3.1 3-D perspective of co-states

32

b) The fact that $\tilde{\psi}_0$ is on the opposite side of disk as $\bar{\psi}_0$ implies that every $\tilde{\psi}$ along the upstream streamline will differ by π from $\bar{\psi}$ along the downstream streamline. Therefore, the $\sin(r\bar{\psi})$ and $\cos(r\bar{\psi})$ terms in Φ_j^r will yield a factor of $(-1)^r$.

Consequently, we have a total sign change for the cosine integral of:

$$\text{sign} = (-1)^{r+j+1}(-1)^r = (-1)^{2r+j+1} = (-1)^{j+1} \tag{3.22}$$

An extra (-1) appears in the sine integral because $\sin(\omega\xi) = -\sin(-\omega\xi)$. Thus, the terms $(-1)^{j+1}$ and $(-1)^j$ appear in the last lines of Eq. (3.21). Then, from Eqs. (3.19) and (3.20), the $\vec{u}$ and $\vec{w}$ for $\xi_0 > 0$ can be obtained as:

$$
\begin{aligned}
&\vec{u}(\omega, r_0, \bar{\psi}_0, \xi_0) \\
&\quad = \cos(\omega\xi_0)\left\{\vec{C}(\omega, r_0, \bar{\psi}_0, 0) + (-1)^{j+1}\left[\vec{C}(\omega, r_0, \tilde{\psi}_0, 0) - \vec{C}(\omega, r_0, \tilde{\psi}_0, -\xi_0)\right]\right\} \\
&\qquad + \sin(\omega\xi_0)\left\{\vec{S}(\omega, r_0, \bar{\psi}_0, 0) + (-1)^{j}\left[\vec{S}(\omega, r_0, \tilde{\psi}_0, 0) - \vec{S}(\omega, r_0, \tilde{\psi}_0, -\xi_0)\right]\right\} \\
&\vec{w}(\omega, r_0, \bar{\psi}_0, \xi_0) \\
&\quad = -\sin(\omega\xi_0)\left\{\vec{C}(\omega, r_0, \bar{\psi}_0, 0) + (-1)^{j+1}\left[\vec{C}(\omega, r_0, \tilde{\psi}_0, 0) - \vec{C}(\omega, r_0, \tilde{\psi}_0, -\xi_0)\right]\right\} \\
&\qquad + \cos(\omega\xi_0)\left\{\vec{S}(\omega, r_0, \bar{\psi}_0, 0) + (-1)^{j}\left[\vec{S}(\omega, r_0, \tilde{\psi}_0, 0) - \vec{S}(\omega, r_0, \tilde{\psi}_0, -\xi_0)\right]\right\}
\end{aligned}
$$

$$\tag{3.23}$$

Note that the above terms from the integrals below the disk are rewritten in terms of integrals above the disk (i.e., the terms with $(-1)^j$ or $(-1)^{j+1}$ which are functions of $\tilde{\psi}_0$ rather than of $\bar{\psi}_0$). These mirror the $\bar{\psi}_0$ terms with the exception that the $\vec{C}$ terms are multiplied by $(-1)^{j+1}$ while the $\vec{S}$ terms are multiplied by $(-1)^j$. As a result of these sign differences, when the

33

complex below-disk velocity from Eq. (3.23) is put back into the time domain—as was done for the above-disk velocity in Eq. (3.16)—the terms involving $\sin\left[\omega(\tau-\xi_0)\right]$ are of the opposite sign from those in Eq. (3.17).

$$
\begin{aligned}
\vec{v}\left(r_0,\bar{\psi}_0,\xi_0,\tau\right) \\
&= \cos\left[\omega(\tau-\xi_0)\right]\vec{C}\left(\omega,r_0,\bar{\psi}_0,\xi_0\right)-\sin\left[\omega(\tau-\xi_0)\right]\vec{S}\left(\omega,r_0,\bar{\psi}_0,\xi_0\right) \\
&\quad +(-1)^{j+1}\left\{\cos\left[\omega(\tau-\xi_0)\right]\vec{C}\left(\omega,r_0,\tilde{\psi}_0,0\right)+\sin\left[\omega(\tau-\xi_0)\right]\vec{S}\left(\omega,r_0,\tilde{\psi}_0,0\right)\right\} \\
&\quad -(-1)^{j+1}\left\{\cos\left[\omega(\tau-\xi_0)\right]\vec{C}\left(\omega,r_0,\tilde{\psi}_0,-\xi_0\right)+\sin\left[\omega(\tau-\xi_0)\right]\vec{S}\left(\omega,r_0,\tilde{\psi}_0,-\xi_0\right)\right\}
\end{aligned}
$$

$$(3.24)$$

From Eq. (3.24), one can write the general, time-domain version of the induced flow below the rotor disk.

$$
\vec{v}\left(r_0,\bar{\psi}_0,\xi_0,\tau\right)=\vec{v}\left(r_0,\bar{\psi}_0,0,\tau-\xi_0\right)+\vec{v}^{\,*}\left(r_0,\tilde{\psi}_0,0,\tau-\xi_0\right)-\vec{v}^{\,*}\left(r_0,\tilde{\psi}_0,-\xi_0,\tau\right) \qquad (3.25)
$$

where $\vec{v}^{\,*}$ is $(-1)^{j+1}$ times the velocity that would be obtained from the adjoint equations (i.e., the equations with a negative sign on the time derivatives). Equation (3.25) is the fundamental result of this derivation and represents the general form of the velocity below the disk in the time domain and/or frequency domain. $\vec{v}\left(r_0,\bar{\psi}_0,\xi_0,\tau\right)$ is the velocity below the rotor disk at point a along the streamline; $\vec{v}\left(r_0,\bar{\psi}_0,0,\tau-\xi_0\right)$ is the velocity at point b where the free streamline intersect the rotor plane; $\vec{v}^{\,*}\left(r_0,\tilde{\psi}_0,0,\tau-\xi_0\right)$ is the adjoint velocity at point c which is centro-symmetric to point b; $\vec{v}^{\,*}\left(r_0,\tilde{\psi}_0,-\xi_0,\tau\right)$ is the adjoint velocity at point d which is centro-symmetric to point a. In other words, it is:

$$\vec{v}^*\left(r,\bar{\psi},\xi,\tau\right)=\left(-1\right)^{j+1}\left[\vec{u}\cos\left(\omega\tau\right)+\vec{w}\sin\left(\omega\tau\right)\right]$$
$$=\left(-1\right)^{j+1}\vec{\tilde{v}}\left(r,\bar{\psi},\xi,\tau\right)$$

(3.26)

where $\vec{\tilde{v}}$ is defined in Eq. (3.26) as conjugate velocity.

The reason that Eq. (3.24) can be generalized to Eq. (3.25) is that any general time-domain solution can be expressed as a Fourier Transform in terms of frequency components. Since Eq. (3.24) would be true for any frequency in that transform, then it is true in general for the inverse transform when written in terms of $\vec{v}^*$ as in Eq. (3.25). In the general time-domain solution, $\vec{v}^*$ is defined as the solution to the adjoint equations—i.e., the solution of the differential equations in which the time derivative terms are multiplied by $\left(-1\right)$. In addition, this adjoint velocity is defined for the condition in which each forcing function in those time-domain equations—i.e., each $\tau_n^m\left(\tau\right)$ in Eq. (3.3)—is multiplied by $\left(-1\right)^{n+1}$ in the forcing functions of the adjoint equations, which is exactly as the following equation:

$$-\left[M^c\right]\left\{\overset{*}{\bar{\Delta}}_n^m\right\}+\left[D^c\right]\left[\tilde{L}^c\right]^{-1}\left[M^c\right]\left\{\bar{\Delta}_n^m\right\}=\left[D^c\right]\begin{bmatrix}\ddots&&\\&\left(-1\right)^{n+1}&\\&&\ddots\end{bmatrix}\left\{\tau_n^{mc}\right\}$$

(3.27)

Then the conjugate velocity could be expressed as

$$\vec{\tilde{v}}^*\left(r,\bar{\psi},\xi,\tau\right)=\sum_{m=0}^{\infty}\sum_{n=m}^{\infty}\bar{\Delta}_n^m\vec{\nabla}\hat{\Psi}_n^{mc}\left(v,\eta,\bar{\psi}\right)$$

(3.28)

It should be noted that the solution in Eq. (3.25) does not include the jump in velocity across the actuator disk due to the mass sources.

3.2 Nowak-He Solution

In the previous section, the drawback of the Moriilo-Duffy solution (that is for flow only above the disk plane) has been removed. Now, one needs to correct the second drawback—that the method is not well converged on the disk. A change of variable will be used to make the Morillo-Duffy solution more like the well-converged Peters-He solution. Recall that the Peters-He solution is in terms of the expansion functions $P(v)/v$ (which are polynomials in r) whereas the Morillo-Duffy solution is in terms of $P(v)$ which all go to zero at the rotor edge for $m+n$ odd. The question now is, can the odd Morillo-Duffy variables be converted into Peters-He variables?

In the previous chapter, Eq. (2.58) is given in order to calculate the Morillo-Duffy variables. The influence coefficient matrix [M] can be also written as

$$\left[M^c \right] = \begin{bmatrix} M_{oo} & M_{oe} \\ M_{eo} & M_{ee} \end{bmatrix} \tag{3.29}$$

Through the method of changing variable, a new [M] matrix can be obtained which is given in Eq. (3.30).

$$\left[M^c \right]_{\text{new}} = \begin{bmatrix} I & M_{oe} \\ M_{eo} A^{-1} & M_{ee} \end{bmatrix} \tag{3.30}$$

where

$$[A_{nj}^m] = \frac{(-1)^{\frac{n+j-2r}{2}} 2\sqrt{2n+1}\sqrt{2j+1}}{\sqrt{H_n^r}\sqrt{H_j^r}(n+j)(n+j+2)\left[(n-j)^2-1\right]} \tag{3.31}$$

36

$$H_n^m = \frac{(n+m-1)!!(n-m-1)!!}{(n+m)!!(n-m)!!}$$

(3.32)

Then the Nowak-He variables $\{\alpha_n^m\}$ can be computed from the following set of linear differential equations.

$$\left[M^c\right]_{\text{new}} \left\{\overset{*}{\alpha_n^m}\right\} + \left[D^c\right]\left[L^c\right]^{-1}\left[M^c\right]_{\text{new}} \left\{\alpha_n^m\right\} = \left[D^c\right]\left\{\tau_n^m\right\}$$

(3.33)

Therefore, the axial induced velocity based on the Nowak-He variables and its adjoint state will be

$$V_{NH} = \sum_{\substack{m,n \\ odd}}^{\infty} \alpha_n^m \frac{1}{v} P_n^m(v)Q_{m+1}^m(i\eta)\cos(m\psi)$$
$$+ \sum_{\substack{m,n \\ even}}^{\infty} a_n^m P_n^m(v)Q_{m+1}^m(i\eta)\cos(m\psi)$$

(3.34)

$$V_{NH}^* = \sum_{\substack{m,n \\ odd}}^{\infty} \Lambda_n^m \frac{1}{v} P_n^m(v)Q_{m+1}^m(i\eta)\cos(m\psi)$$
$$+ \sum_{\substack{m,n \\ even}}^{\infty} \Delta_n^m P_n^m(v)Q_{m+1}^m(i\eta)\cos(m\psi)$$

(3.35)

where $\{\Delta_n^m\}$ and $\{\Lambda_n^m\}$ are Morillo-Duffy adjoint variables and Nowak-He adjoint variables, respectively. For the special case ($\omega = 0$), it has

$$\{\Delta_n^m\} = \{a_j^m\} \text{ and } \{\Lambda_n^m\} = \{\alpha_n^m\}$$

(3.36)

The beauty of this approach is that both the Morillo-Duffy variables and the Peters-He variables can be obtained from a single set of state-variable questions. No new states are required to have both representations available to the user. The combination of odd Peters-He and even Morillo-Duffy will be called as the Huang-He variables.

3.3 Huang-He Solution

The previous section allows all z-components of velocity on the disk to be expanded in terms of the $P(\nu)/\nu$ which are polynomials in the radial coordinate r (rather than in the z derivative of the potentials). It makes sense that it would be good also to expand the x and y velocity components in terms of $P(\nu)/\nu$ (rather than in terms of the x and y derivatives of the potentials). Unlike the z component, however, the x and y derivatives involve a shift of harmonic number due to the $\sin(\psi)$ and $\cos(\psi)$ that appear in the change of variable. Thus, a change of variable to give well-converged x and y velocities will involve a coupling between harmonics in the transform. In this section, an appropriate transform is derived. The new variables will be called Huang-He variables.

The Huang-He variables can be transformed from the Morillo-Duffy variables with another transform matrix $[S]$, as is shown in Eq. (3.37).

$$\left\{\alpha_j^r\right\} = \left[S_{jn}^{rm}\right]\left\{a_n^m\right\} \tag{3.37}$$

where

$$S_{jn}^{rm} = 0, \text{ for } r \neq |m \pm 1|$$

$$\text{for } m = 0, \ S_{jn}^{10} = \begin{cases} \sigma_n^0 \sqrt{j(j+1)}, \text{ for } j = n+1 \\ \varsigma_n^0 \sqrt{j(j+1)}, \text{ for } j = n-1 \\ 0, \text{ for } j \neq n \pm 1 \end{cases}$$

$$\text{for } m > 0, \ S_{jn}^{rm} = \begin{cases} \dfrac{1}{2} \sigma_n^m \sqrt{(j+m+1)(j-m)}, \text{ for } j = n+1 \\ \dfrac{1}{2} \varsigma_n^m \sqrt{(j+m+1)(j-m)}, \text{ for } j = n-1 \\ 0, \text{ for } j \neq n \pm 1 \end{cases}$$

Then the x component of the induced velocity above the rotor disk ($z < 0$) based on Huang-He variables can be expressed as

$$V_{HH} = \begin{cases} \displaystyle\sum_{m,n} a_n^m v_{nx}^m, \text{ for } x \geq 0 \\ \displaystyle\sum_{\substack{m,n \\ odd}} \alpha_n^m \cos(m\psi) Q_{m+1}^m (i\eta) \frac{1}{v} \bar{P}_n^m (v) + \sum_{\substack{m,n \\ even}} a_n^m v_{nx}^m, \text{ for } x < 0 \end{cases} \tag{3.38}$$

where

$$v_{nx}^m = \left[\sigma_n^m F_{n+1}^m + \varsigma_n^m F_{n-1}^m \right] \cos\left[(m-1)\psi \right] Q_{|m-1|+1}^{|m-1|} (i\eta) \\ + \left[\sigma_n^m G_{n+1}^m + \varsigma_n^m G_{n-1}^m \right] \cos\left[(m+1)\psi \right] Q_{m+2}^{m+1} (i\eta) \text{, for } m \neq n \tag{3.39}$$

and where

$$F_k^m \equiv \sqrt{1-v^2} \, \frac{1}{2v} \frac{d\bar{P}_k^m}{dv} - \frac{m}{2\sqrt{1-v^2}} \bar{P}_k^m \tag{3.40}$$

$$G_k^m \equiv \sqrt{1-v^2} \, \frac{1}{2v} \frac{d\bar{P}_k^m}{dv} + \frac{m}{2\sqrt{1-v^2}} \bar{P}_k^m \tag{3.41}$$

39

$$\frac{1}{v}\frac{\partial P_k^m(v)}{\partial v} = \frac{1}{1-v^2}\left[\sqrt{(k+m+1)(k-m)}\sqrt{1-v^2}\,\frac{P_k^{m+1}(v)}{v} - mP_k^m(v)\right] \quad (3.42)$$

For the special case $m = n \neq 0$,

$$v_{nx}^m = \left[\sigma_m^m F_{m+1}^m + F_{m-1}^m\right]\cos\left[(m-1)\psi\right]Q_{|m-1|+1}^{|m-1|}(i\eta)$$
$$+ \left[\sigma_m^m G_{m+1}^m + G_{m-1}^m\right]\cos\left[(m+1)\psi\right]Q_{m+2}^{m+1}(i\eta) \quad (3.43)$$

For $m = n = 0$,

$$v_{nx}^m = \frac{2}{\pi}\sqrt{\frac{1-v}{1+v}}\cos(\psi)Q_2^1(i\eta) \quad (3.44)$$

Chapter 4: Blending of Solutions

4.1 Blending Function

Since the change of variable solution such as Nowak-He solution for the axial induced velocity and Huang-He solution for x component of the induced velocity behaves well on the disk and the Morillo-Duffy solution is more accurate away from the disk, the blending function is designed to transition from the change of variable solution on the disk quickly to Morillo-Duffy solution off the disk. Such a blending function should be such that it gives the pure Huang-He solution on the disk and the pure Morillo-Duffy solution once one is significantly away from the disk. A simple, convex, linear blend seems to be the most logical choice for such a blend.

Equations (4.1) and (4.2) give the blending function for the axial induced velocity, and Eqs. (4.3) and (4.4) are for x component of the induced velocity.

$$V_{BL} = \frac{1}{1+bh} V_{NH} + \frac{bh}{1+bh} V_{MD} \tag{4.1}$$

$$V^{*}_{BL} = \frac{1}{1+bh} V^{*}_{NH} + \frac{bh}{1+bh} V^{*}_{MD} \tag{4.2}$$

$$V_{BL} = \frac{1}{1+bh} V_{HH} + \frac{bh}{1+bh} V_{MD} \tag{4.3}$$

$$V^{*}_{BL} = \frac{1}{1+bh} V^{*}_{HH} + \frac{bh}{1+bh} V^{*}_{MD} \tag{4.4}$$

where

41

$$\begin{cases} h = 0, \text{ if } \eta < \varepsilon \\ h = \eta - \varepsilon, \text{ if } \eta \geq \varepsilon \end{cases} \tag{4.5}$$

The concept of Eqs. (4.1)−(4.4) is that there is a simple blend with a gain factor b based on some measure of the distance from the disk, which is called as "h". Since the variable η is a measure of the distance from the disk in ellipsoidal coordinates, η represents a natural measure for h. However, because there is a singularity in the Morillo-Duffy equations at $\eta = 0$, there needs to be a small area around the disk where no blending is done. Eq. (4.5) gives one method of representing the distance h by utilization of a buffer zone ε to be determined later.

This form of the equation was tested against exact solutions for various values of ε and b over a wide range of frequencies and pressure inputs. A fixed value of ε was decided upon, and the best b was plotted as a function of η for various skew angles χ. These optimum values were then fit by the following approximate functions.

$$\begin{aligned} x \leq 0, |y| \leq 1, b &= 20\left[1 - \frac{y^2 \sin(\chi)}{1 + \eta^2}\right] \\ x \leq 0, |y| > 1, b &= 20\left[1 - \frac{y^2 \sin(\chi)}{1 + \eta^2 + 0.615(y^2 - 1)}\right] \\ x > 0, |y| \leq 1, b &= 20\left[1 - \frac{(x^2 + y^2)\sin(\chi)}{1 + \eta^2}\right] \\ x > 0, |y| > 1, b &= 20\left[1 - \frac{(x^2 + y^2)\sin(\chi)}{1 + \eta^2 + 0.615(y^2 - 1)}\right] \end{aligned} \tag{4.6}$$

One needs not to calculate Morillo-Duffy velocity either on the disk or close to the disk edge ($\varepsilon = 0.01$) where it is ill-conditioned.

4.2 Downstream Adjoint Theorem

Now, two issues of the Morillo-Duffy Model have been addressed: 1.) the flow below the disk, and 2.) the poor convergence on the rotor disk. The third drawback to be addressed is the divergence downstream as the skew angle goes to 90°. The issue is that, as the flow becomes edgewise, the induced flow downstream does not decay because the trailing wake effect then remains in the rotor plane even far behind the disk. The Galerkin test functions, however, naturally decay; and thus they cannot converge to a non-decaying value of induced flow. The approach which is taken for this third drawback is to note that, for perfectly edgewise flow, one can utilize the same adjoint theorem−that was used to find the flow below the disk in terms of the flow above the disk−to find the flow downstream for edgewise flow from the flow upstream. In this section, the adjoint theorem is extended to the case of perfectly edgewise flow.

Let s_0 be the x-distance downstream in edgewise flow at which the flow is converged by the blended method. This distance is taken to be on a sphere of radius ρ or else to be zero if $y^2 + z^2 \geq \rho^2$. For computing the axial induced velocity, $\rho = 1$; for the in-plane components of the induced velocity, $\rho = \sqrt{\cos(\chi)}$

$$\begin{cases} s_0 = \sqrt{\rho^2 - y^2 - z^2}, \text{ for } y^2 + z^2 < \rho^2 \\ s_0 = 0, \text{ for } y^2 + z^2 \geq \rho^2 \end{cases} \tag{4.7}$$

Let x be a point (further downstream than $-s_0$) at which the velocity is desired. Let the distance along the x-axis from $(-s_0)$ to that point at which the velocity is desired be called $\sigma = (-x - s_0)$. It follows that the distance along the streamline going through $-s_0$ to the point on the streamline

that is closest to x (i.e., perpendicular) is then given by $\sigma \sin(\chi)$. Then the time delay for adjoint theorem is defined to be $\sigma \sin(\chi)$.

Thus, in the plane of the disk, $z = 0$ and $\rho < y < -\rho$, one should place s_0 at the trailing edge of the disk (region ①); $s_0 = 0$ for $z = 0$ and $|y| > \rho$ (region ②) which is illustrated in Fig. 4.1. The thick solid curve denotes the trailing edge of the rotor disk.
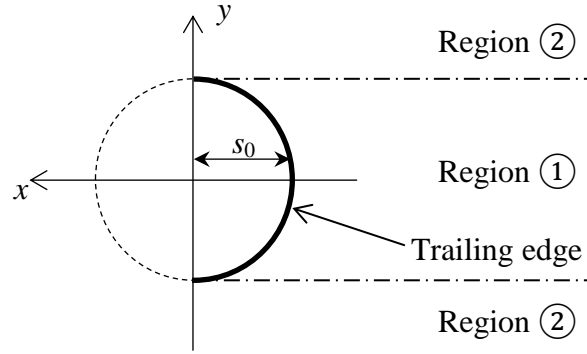
Figure 4.1 Illustration of downstream in edgewise flow at the rotor disk.

Then the downstream velocity ($x \leq 0$ and $\left| x^2 + y^2 + z^2 \right| \geq \rho^2$) can be found from the adjoint theorem. Eqs. (4.8) and (4.9) are for the axial velocity; Eqs. (4.10) and (4.11) are used for the swirl velocity.

$$
\begin{aligned}
V_{DS}(x, y, z, t) &= V_{DS}(-\sigma - s_0, y, z, t) \\
&= V_{BL}(-s_0, y, z, t - \sigma \sin(\chi)) \\
&\quad + V_{BL}^*(+s_0, -y, z, t - \sigma \sin(\chi)) - V_{BL}^*(\sigma + s_0, -y, z, t)
\end{aligned}
\tag{4.8}
$$

$$
\begin{aligned}
V_{DS}^*(x, y, z, t) &= V_{DS}^*(-\sigma - s_0, y, z, t) \\
&= V_{BL}^*(-s_0, y, z, t + \sigma \sin(\chi)) \\
&\quad + V_{BL}(+s_0, -y, z, t + \sigma \sin(\chi)) - V_{BL}(\sigma + s_0, -y, z, t)
\end{aligned}
\tag{4.9}
$$

44

$$V_{DS}(x,y,z,t) = V_{DS}(-\sigma - s_0, y, z, t)$$
$$= V_{BL}(-s_0, y, z, t - \sigma\sin(\chi)) \tag{4.10}$$
$$-V_{BL}^*(+s_0, -y, z, t - \sigma\sin(\chi)) + V_{BL}^*(\sigma + s_0, -y, z, t)$$

$$V_{DS}^*(x,y,z,t) = V_{DS}^*(-\sigma - s_0, y, z, t)$$
$$= V_{BL}^*(-s_0, y, z, t + \sigma\sin(\chi)) \tag{4.11}$$
$$-V_{BL}(+s_0, -y, z, t + \sigma\sin(\chi)) + V_{BL}(\sigma + s_0, -y, z, t)$$

These formulas can be used for perfectly edgewise flow, but a model is needed that will work not just at $\chi = 90^o$ but at all skew angles as one approaches 90°. Once again, the concept of a blending will be utilized. The velocity from the downstream adjoint theorem will be blended with the previously blended Morillo-Duffy and Huang-He velocity. The blend will be designed so that, at perfectly edgewise flow, it will be all downstream velocity; while as one moves away from edgewise, it will revert to the previous blend. This will be done in the next section.

4.3 Final Downstream Velocity

The final piece of the blending is to combine the blending velocity V_{BL} and the downstream velocity V_{DS} to get the final downstream velocity V_F, which is given in Eq. (4.12). As with the previous blend, a convex linear blending function is utilized. In this case, the function is assumed to be dependent on the distance downstream from a known convergent point (this distance is called σ') and the skew angle. The formula for either the regular velocity or the adjoint velocity V_F^* is given in Eqs. (4.12)–(4.13).

$$V_F = V_{BL}[1 - f(\sigma', \chi)] + V_{DS}[f(\sigma', \chi)] \tag{4.12}$$

$$V_F^* = V_{BL}^*[1 - f(\sigma', \chi)] + V_{DS}^*[f(\sigma', \chi)] \tag{4.13}$$

For the axial induced velocity, $\sigma' = \sigma$, which is already defined in the previous section. [Note that for both on the disk and upstream ($x > -s_0$), $V_F = V_{BL}$.] Originally, many cases were run with an optimum value of f found for each case. These were then plotted as functions of χ at various values of y. The following functions were then found to be a good fit for these optimum data at all frequencies and inputs.

$$f(\sigma', \chi) = \begin{cases} \dfrac{\sin^2(\chi)}{\sin^2(\chi) + \sigma' g(\chi)}, & \text{for } |y| \le 1 \\[4mm] \dfrac{\sin^2(\chi)}{\sin^2(\chi) + \left(\sigma' + 1.5\sqrt{y^2 - 1}\right) g(\chi)}, & \text{for } |y| > 1 \end{cases} \tag{4.14}$$

where

$$g(\chi) = 1.84\cos^{1/2}(\chi) - 4.06\cos(\chi) + 11.84\cos^{3/2}(\chi) \tag{4.15}$$

For the swirl velocity (the x and y velocity components), a slightly different form was found to be optimum:

$$f(\sigma', \chi) = \frac{\left[1 - \cos(\chi)\right]^{5/3} \sin^2(\chi)}{\sin^2(\chi) + \sigma'\left\{1.84\cos^{1/2}(\chi) - 4.06\cos(\chi) + 11.84\cos^{3/2}(\chi)\right\}} \tag{4.16}$$

where

$$\sigma' = \begin{cases} 0, & \text{for } \rho^2 < x^2 + y^2 + z^2 < 1 \text{ and } y^2 + z^2 < \rho^2 \\ -x - \sqrt{1 - y^2 - z^2}, & \text{for } x^2 + y^2 + z^2 > 1 \text{ and } y^2 + z^2 < \rho^2 \\ -x, & \text{for } y^2 + z^2 > \rho^2 \end{cases} \tag{4.17}$$

For the special case when $|y| > 1$, $v_x = 0$ and $v_y = 0$.

46

4.4 Numerical Results

4.4.1 Axial Induced Velocity

With the blending method discussed above, some typical results (four skew angles, two frequencies, and various cuts through the flow field) are presented to show the degree of accuracy of the solution. Results are for the z-component (normal component) of velocity. Some results have 6 harmonic for the odd terms and 4 harmonics for the even terms (25 states). Other results have 12 harmonics for the odd terms and 8 harmonics for even terms (74 states). For example:

m-odd = 12, m-even = 8 for $\omega = 0$

m-odd = 12, m-even = 8 for $\omega = 4$ and $0° < \chi \le 45°$

m-odd = 6, m-even = 4 for $\omega = 4$ and $45° < \chi \le 90°$

The axial coordinate is z, with $z > 0$ downstream. The fore-aft coordinate is x, with $x < 0$ being downstream. The lateral coordinate is y. The rotor is given an elliptical pressure distribution for the first 20 plots. The results for $\omega = 0$ (constant loading) and $\omega = 4$ (frequency = $4V_\infty / R$) are illustrated in Figs. 4.2−4.21. The open circles on the plots are the exact solution for each case, which can be found from a convolution integral from upstream infinity along a streamline down to that particular point. The solid lines are the new, blended solutions. For comparison, each figure shows the various velocities that are blended together to obtain the final solution. The dashed-dot blue line is the Morillo-Duffy solution. The long-dash green curve is the velocity from the Nowak-He variables.

Figures 4.2−4.5 give induced velocity at the rotor disk (y = 0.0 and z = 0.0), for ω = 0, and

there are no imaginary parts in the solution. The skew angle is varied from 0° to 85°. Figures

4.6 and 4.7 show the results for two cuts along the y axis (y = 0.5 and 1.26). Since the flow is

symmetric about the y axis, only the induced velocity for $y \geq 0$ needs to be computed. Figure 4.8

presents a y-traverse, and the blended solution catches the spike of exact solution accurately

around the edge of the rotor disk due to the vortex. Results above the disk (z = −0.4) are directly

above the disk and are plotted versus x in Fig. 4.9. In Fig. 4.10, results below the disk (z = +0.4)

are plotted from the center of the skewed wake versus x_0, which is the x location on the rotor disk

through which a streamline would pass. Thus, x_0 = 0 is the streamline going through the rotor

center.

Figure 4.2, which shows flow on the disk, shows axial flow so that the Morillo-Duffy and

Nowak-He variables work equally well on the disk, and the "downstream" correction has no

physical meaning (and is not blended). As skew angle is increased (Figs. 4.2−4.5), one can see

the increase of downstream flow. The Nowak-He change of variable becomes more and more

accurate (with respect to Morillo-Duffy) as skew angle increases, and the velocity begins to

approach the "downstream" solution (which becomes the exact solution as skew angle

approaches 90). Notice that the blending function does an excellent job of combining the three

solutions together to match the exact solution (from a convolution integral).

Figure 4.7 is an x-plot located at 0.26 radii laterally from the edge of the disk. Although this

is very close to the trailing vortex that comes of off the disk edge, the velocity is still quite good.

Figure 4.8 sheds further insight on this correlation by giving a plot of velocity versus lateral

coordinate y off the edge of the disk. The point y = 1.26 marks the location of the cross-plot in

Fig. 4.7. One can see that the peak due to the trailing vortex is well-captured with the appropriate decay off of the disk.

Figures 4.9−4.10 give velocity 0.4 radii above the disk and 0.4 radii below the disk, respectively. The same good convergence at the disk is seen above the disk. Here, the Nowak-He variables have less effect; and it is basically a blending of downstream and Morillo-Duffy variables. Below the disk, the improvement of the downstream blending at the disk is magnified. This is because the flow below the disk (in the adjoint method) is sensitive to the flow at the disk. Figure 4.11, which is a traverse above the disk, illustrates that this above disk correlation is good not simply at $z = -0.4$ but continues at all locations.

Ten similar cases for $\omega = 4$ are demonstrated in Figs. 4.12−4.21. The real part and imaginary part of the induced velocity are given in the separate plots. The results obtained through the blended method match the exact solution perfectly both upstream and downstream, above the rotor disk and below the disk.

The same trends as were seen for $\omega = 0$ in Figs 4.2−4.11 are repeated at $\omega = 4$ in Figs. 4.12−4.21. In this second set of figures, there are both real and imaginary plots (for the in-phase and out-of-phase velocities); but the same trends persist as were found for the steady case. Figures 4.15, 4.16, and 4.20 clearly show the oscillations in the induced flow behind the disk. This is due to the fact that vorticity is being shed into the wake at a frequency of 4.0. Thus, there are oscillations in the velocity downstream that decay slowly (and which cease to decay at all as the skew angle approaches 90). Neither the Morillo-Duffy variables nor the Nowak-He variables can predict such oscillations, but the adjoint velocity gives the precise oscillations that

are needed. After blending, the solution is virtually exact at all skew angles. This accuracy naturally persists downstream from the rotor disk, which is shown in Fig. 4.20.

To demonstrate that the method of blending still works well for other pressure distribution cases, the results with second collective mode (τ_3^0) and cyclic pressure distribution (τ_2^1) are illustrated in Figs. 4.22−4.25 and 4.26−4.29, respectively. For both of those cases, the blending results still show excellent correlation with the exact solution either on the rotor ($z = 0$) or 0.4 radii below the rotor ($z = 0.4$) for static loading and dynamic loading.
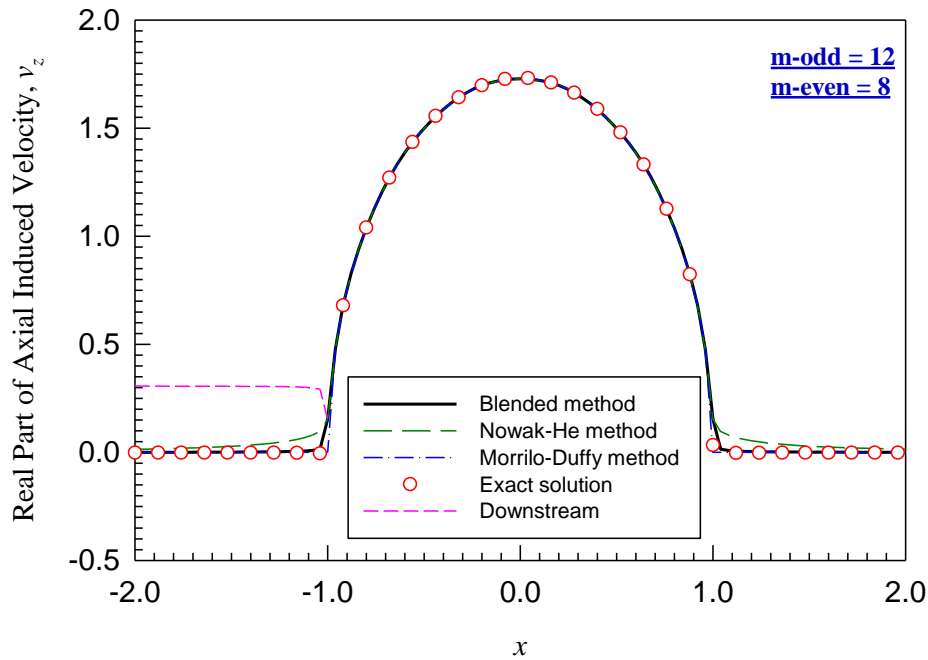
Figure 4.2 Real part of axial velocity v_z for $y = 0.0$, $z = 0.0$ with τ_1^0 for $\omega = 0$, $\chi = 0°$. (m-odd = 12, m-even = 8)

50
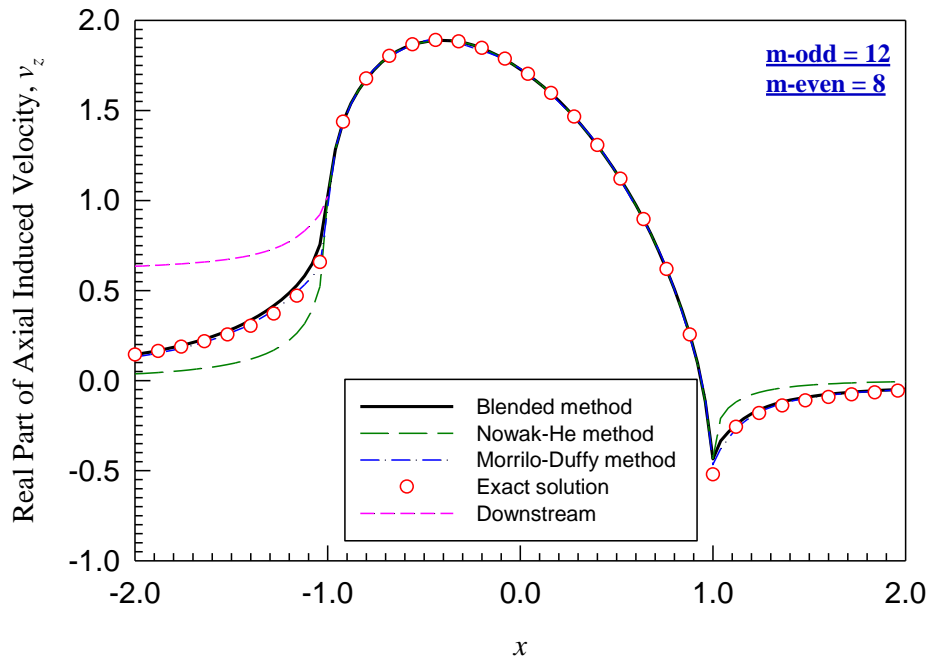
Figure 4.3 Real part of axial velocity v_z for $y = 0.0$, $z = 0.0$ with τ_1^0 for $\omega = 0$, $\chi = 30^\circ$. (m-odd = 12, m-even = 8)
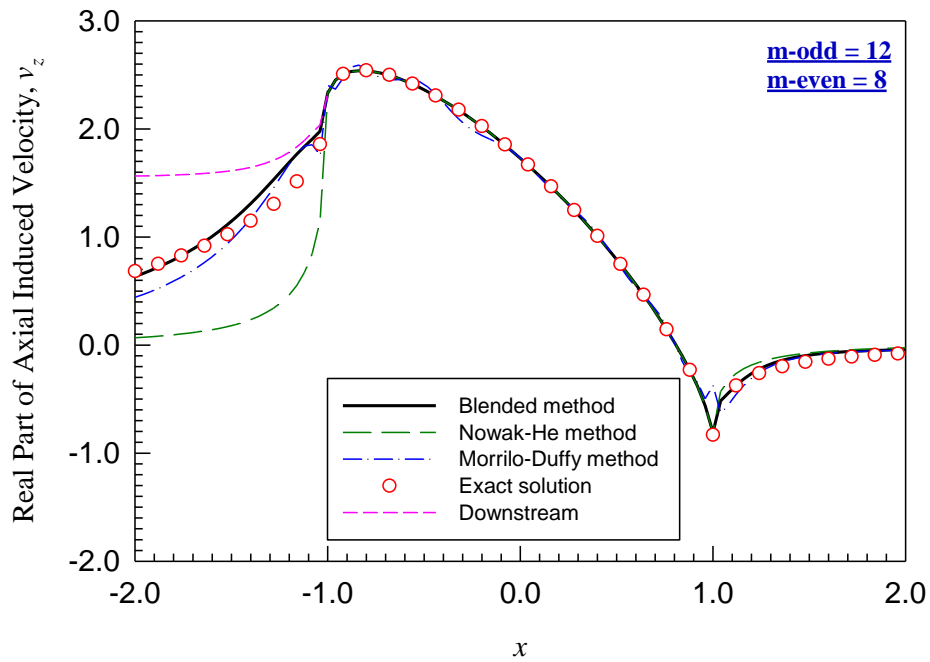
Figure 4.4 Real part of axial velocity v_z for $y = 0.0$, $z = 0.0$ with τ_1^0 for $\omega = 0$, $\chi = 60^\circ$. (m-odd = 12, m-even = 8)

51
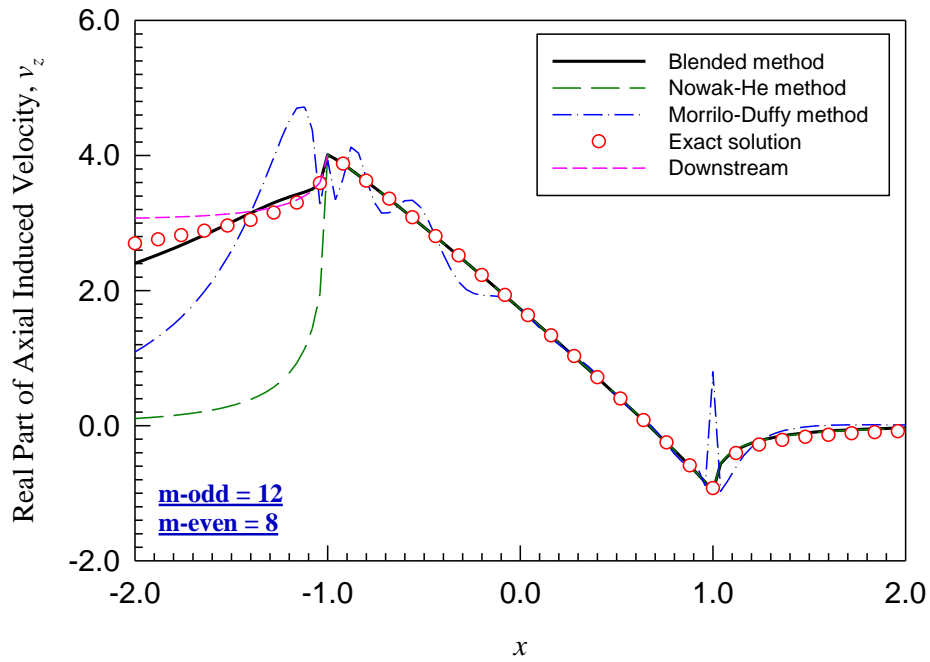
Figure 4.5 Real part of axial velocity v_z for $y = 0.0$, $z = 0.0$ with τ_1^0 for $\omega = 0$, $\chi = 85^o$. (m-odd = 12, m-even = 8)
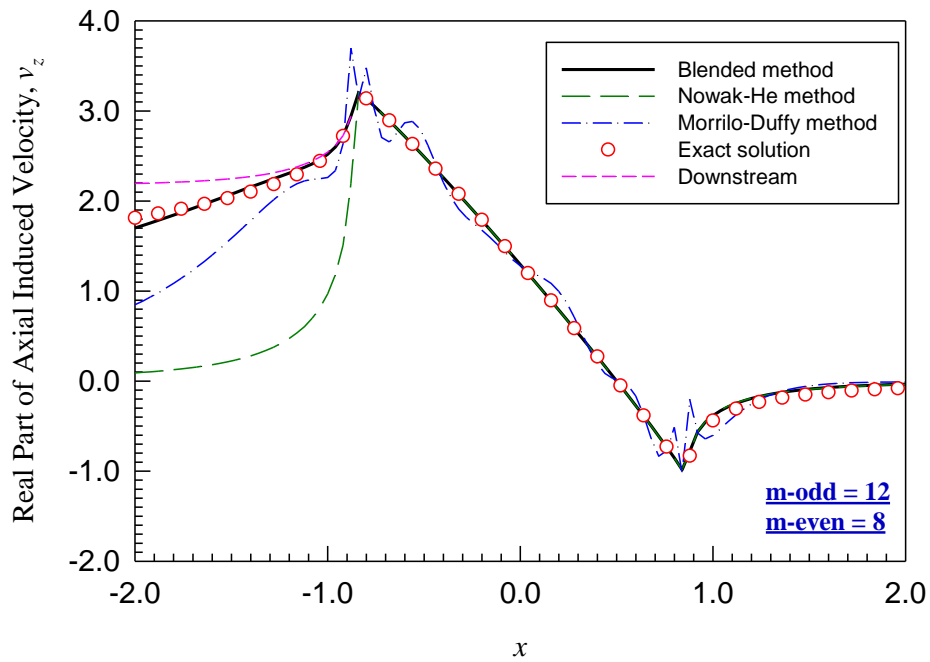
Figure 4.6 Real part of axial velocity v_z for $y = 0.5$, $z = 0.0$ with τ_1^0 for $\omega = 0$, $\chi = 85^o$. (m-odd = 12, m-even = 8)
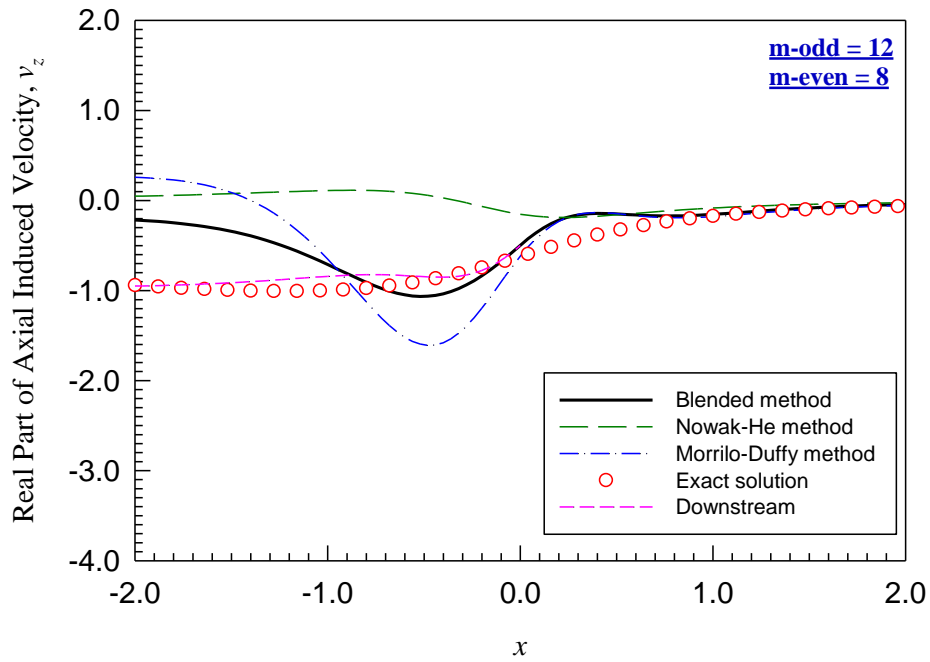
Figure 4.7 Real part of axial velocity v_z for $y = 1.26$, $z = 0.0$ with τ_1^0 for $\omega = 0$, $\chi = 85^o$. (m-odd = 12, m-even = 8)
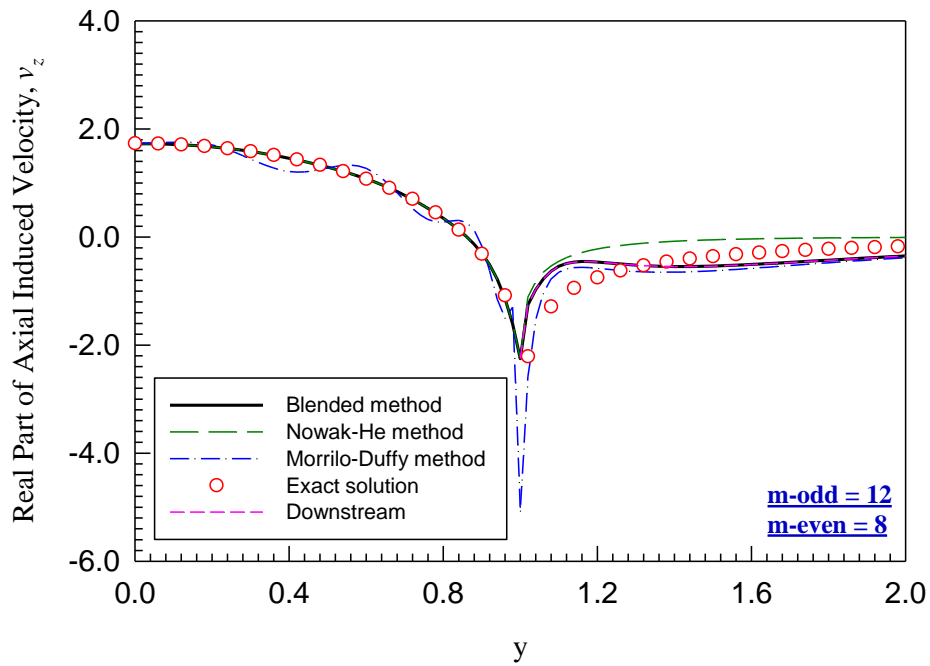
Figure 4.8 Real part of axial velocity v_z for $x = 0.0$, $z = 0.0$ with τ_1^0 for $\omega = 0$, $\chi = 85^o$. (m-odd = 12, m-even = 8)
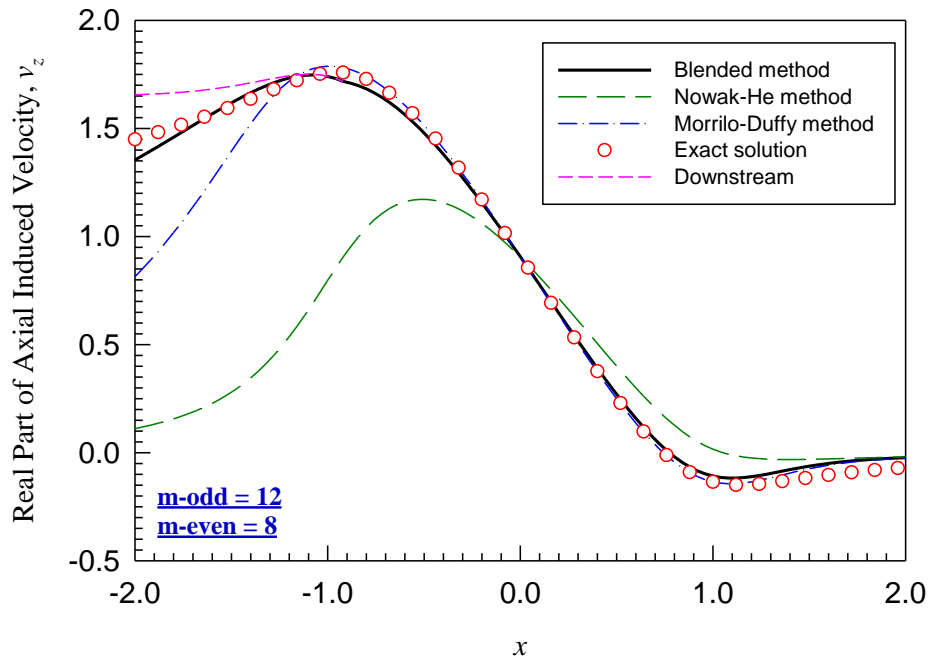
Figure 4.9 Real part of axial velocity v_z for $y = 0.0$, $z = -0.4$ with τ_1^0 for $\omega = 0$, $\chi = 85^o$. (m-odd = 12, m-even = 8)
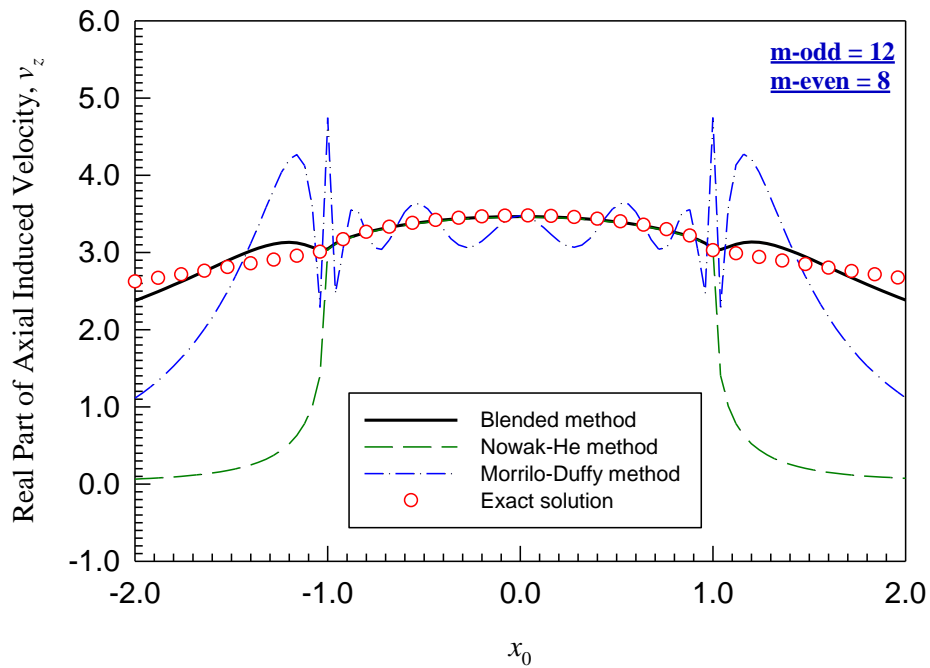
Figure 4.10 Real part of axial velocity v_z for $y = 0.0$, $z = 0.4$ with τ_1^0 for $\omega = 0$, $\chi = 85^o$. (m-odd = 12, m-even = 8)
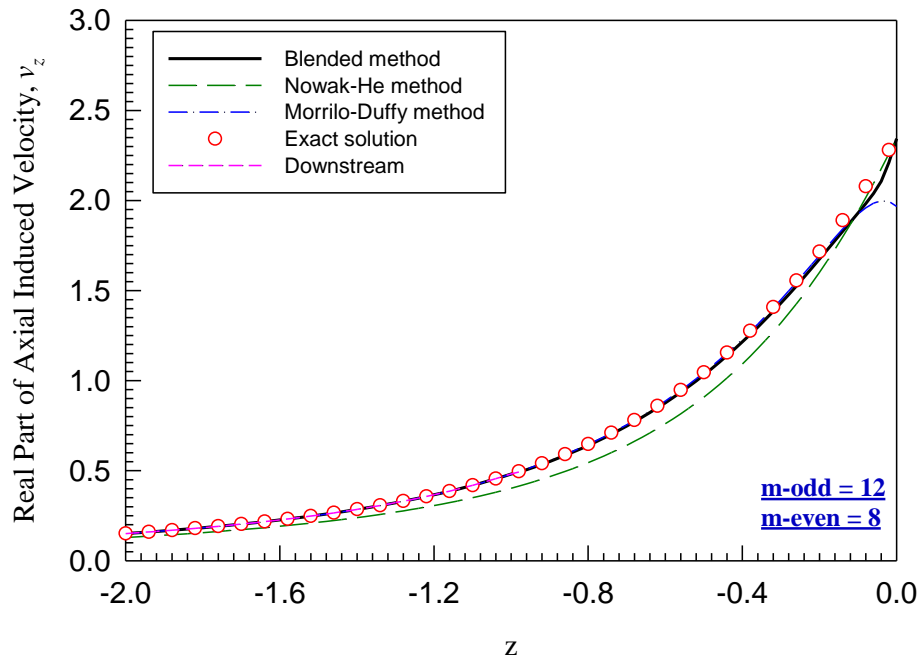
Figure 4.11 Real part of axial velocity v_z for $x = -0.25$, $y = 0.0$ with τ_1^0 for $\omega = 0$, $\chi = 85^o$. (m-odd = 12, m-even = 8)
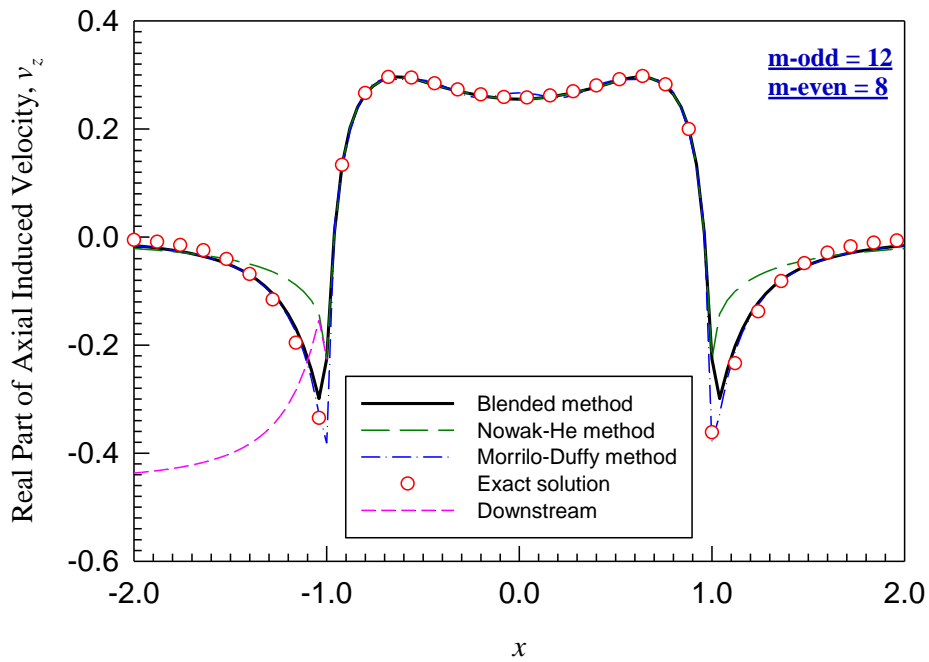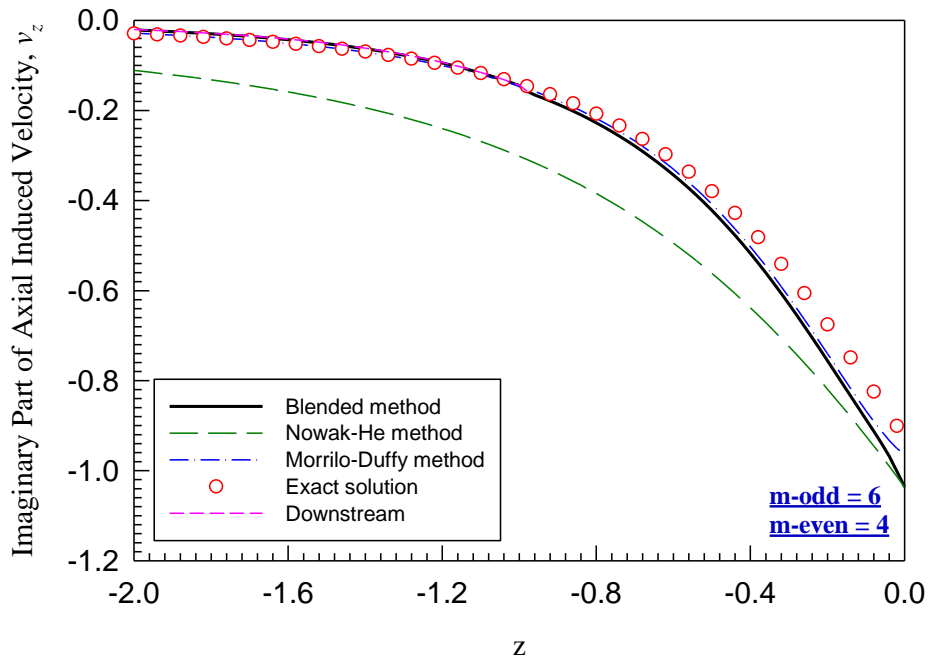

(a)
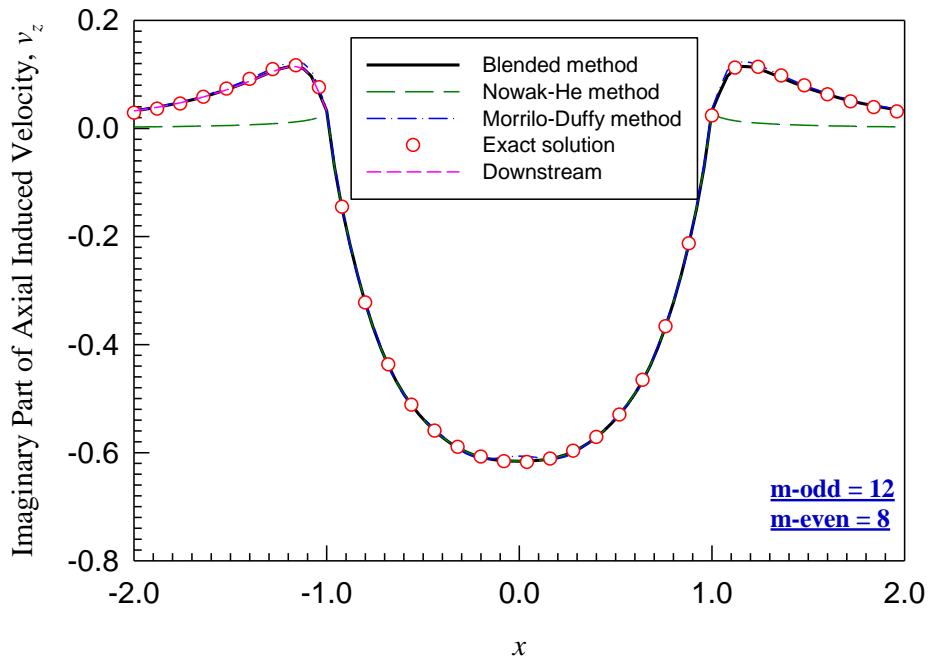
(b)

Figure 4.12 Axial velocity v_z for $y = 0.0$, $z = 0.0$ with τ_1^0 for $\omega = 4$, $\chi = 0^\circ$: (a) real part and (b) imaginary part. (m-odd = 12, m-even = 8)
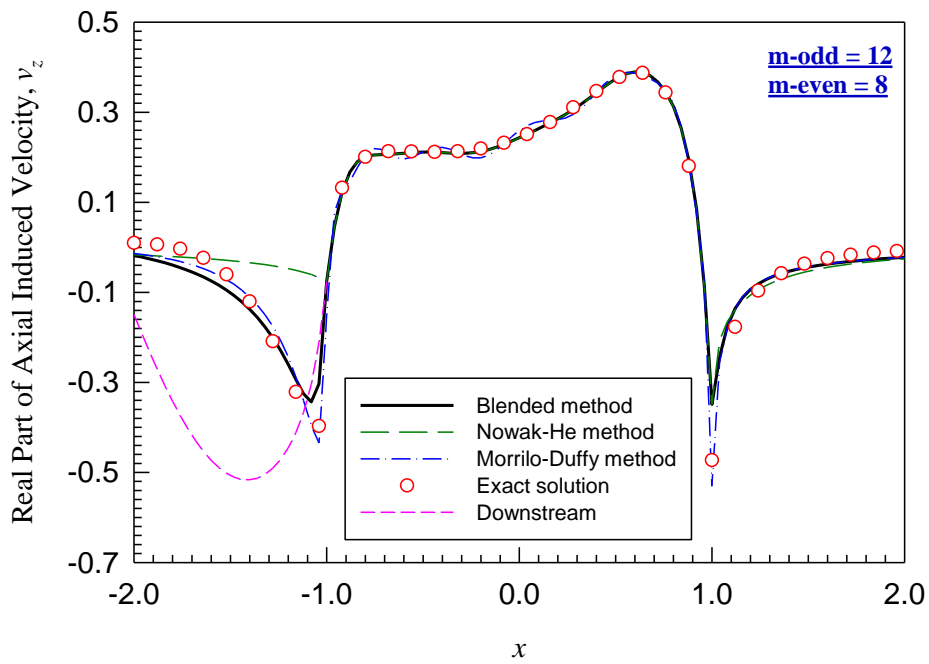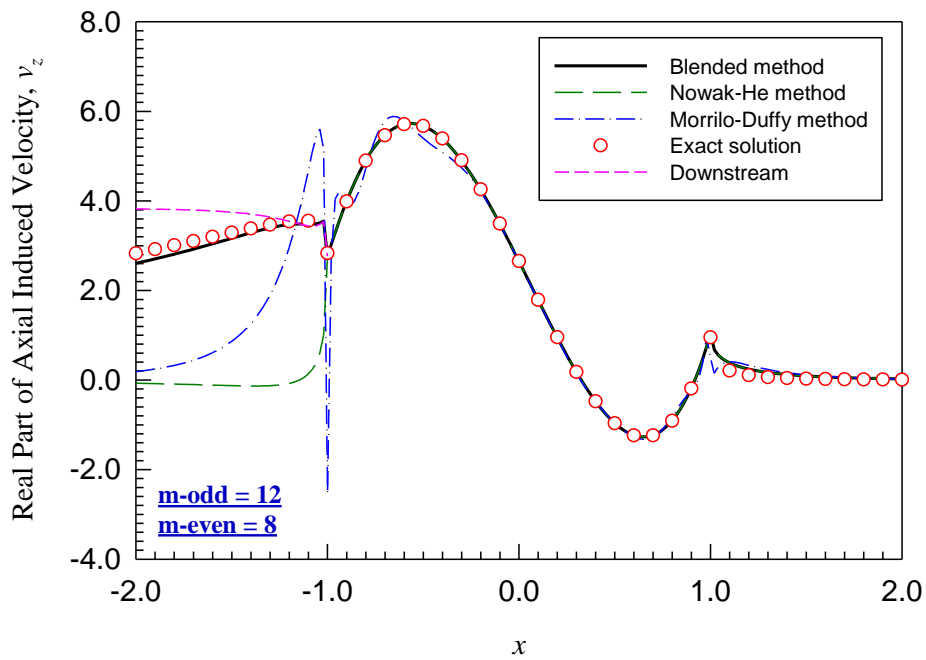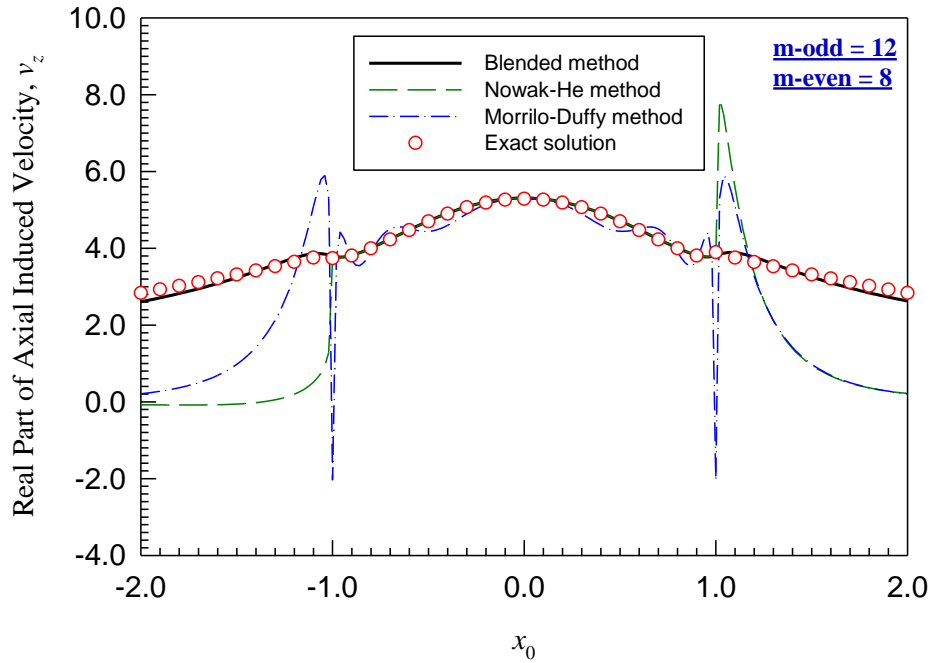

(a)
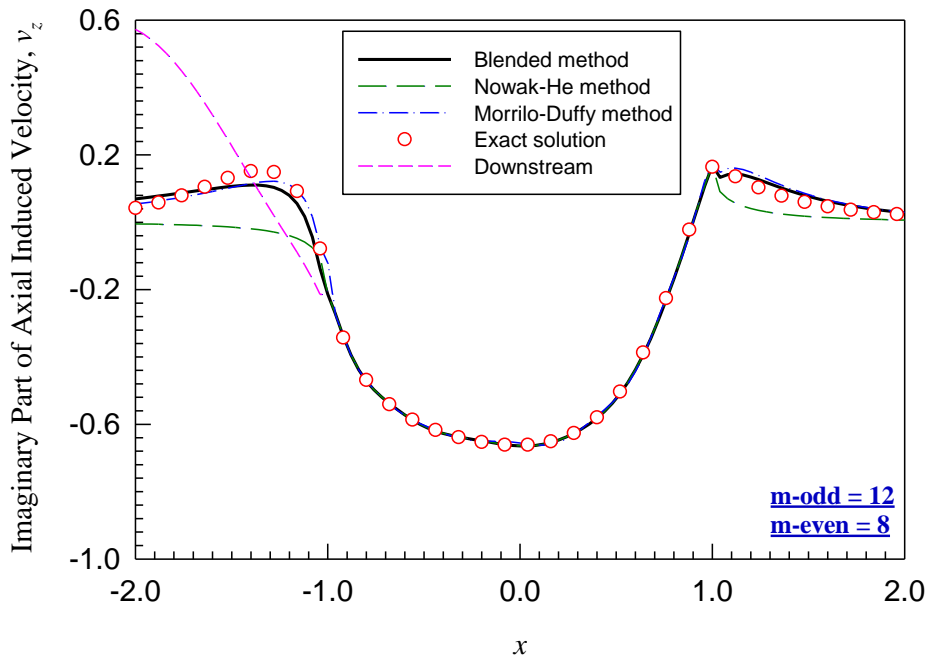
(b)

Figure 4.13 Axial velocity v_z for $y = 0.0$, $z = 0.0$ with τ_1^0 for $\omega = 4$, $\chi = 30^o$: (a) real part and (b) imaginary part. (m-odd = 12, m-even = 8)
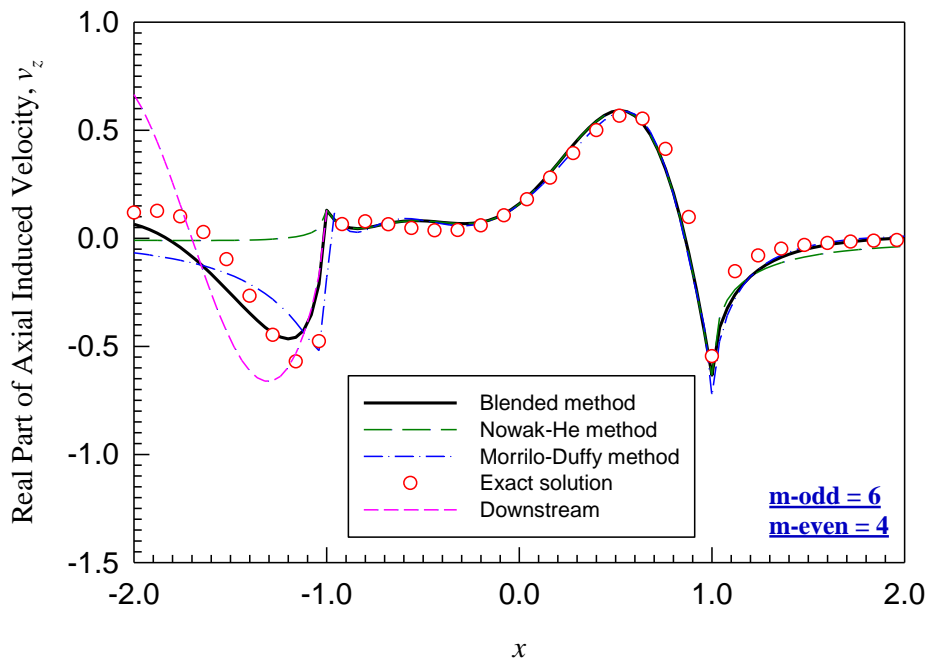
(a)
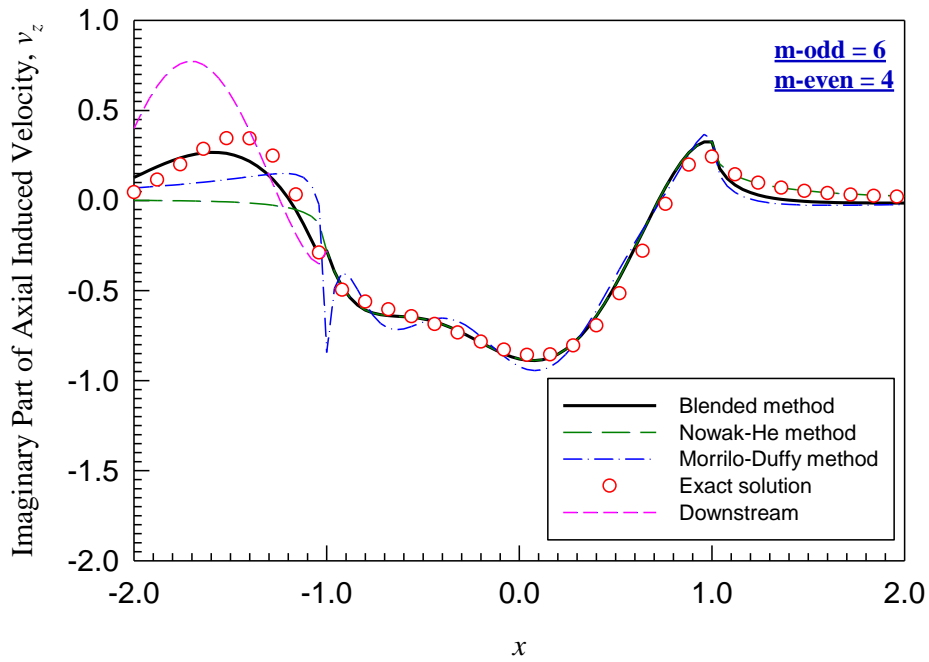
(b)

Figure 4.14 Axial velocity v_z for $y = 0.0$, $z = 0.0$ with τ_1^0 for $\omega = 4$, $\chi = 60^\circ$: (a) real part and (b) imaginary part. (m-odd = 6, m-even = 4)
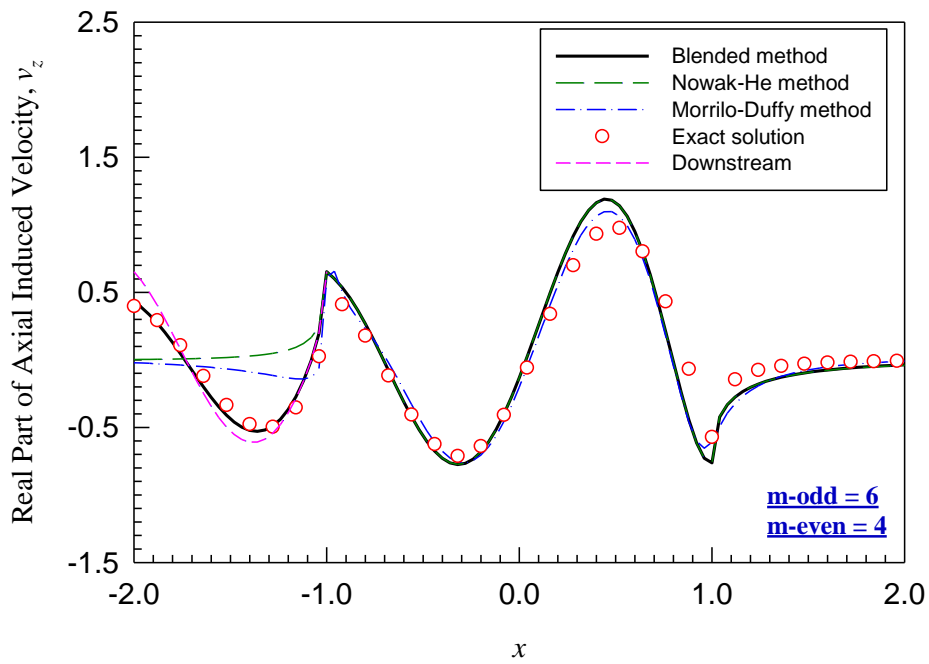
(a)
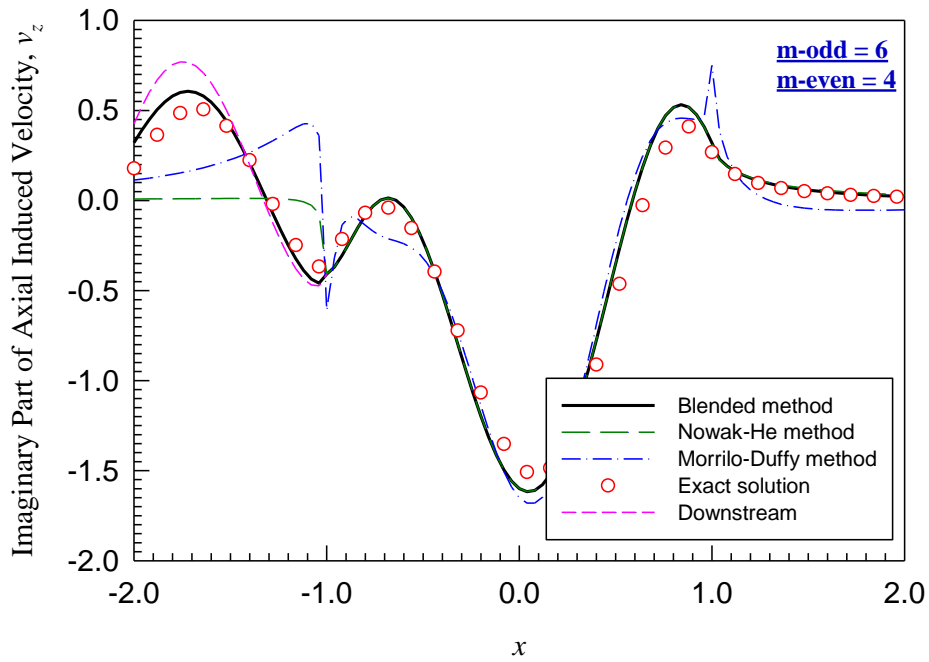
(b)

Figure 4.15 Axial velocity v_z for $y = 0.0$, $z = 0.0$ with τ_1^0 for $\omega = 4$, $\chi = 85^o$: (a) real part and (b) imaginary part. (m-odd = 6, m-even = 4)
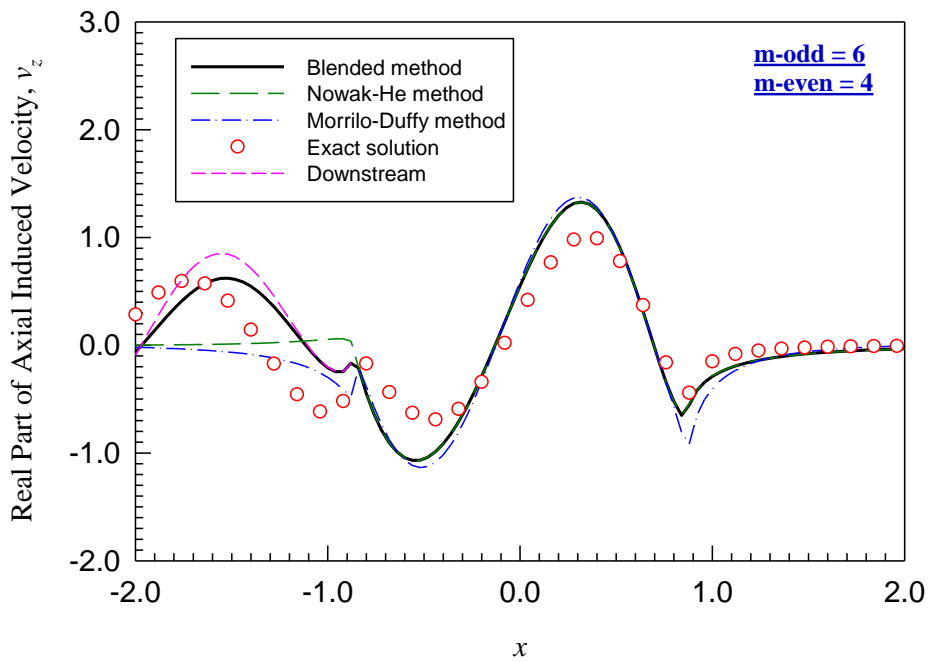
(a)
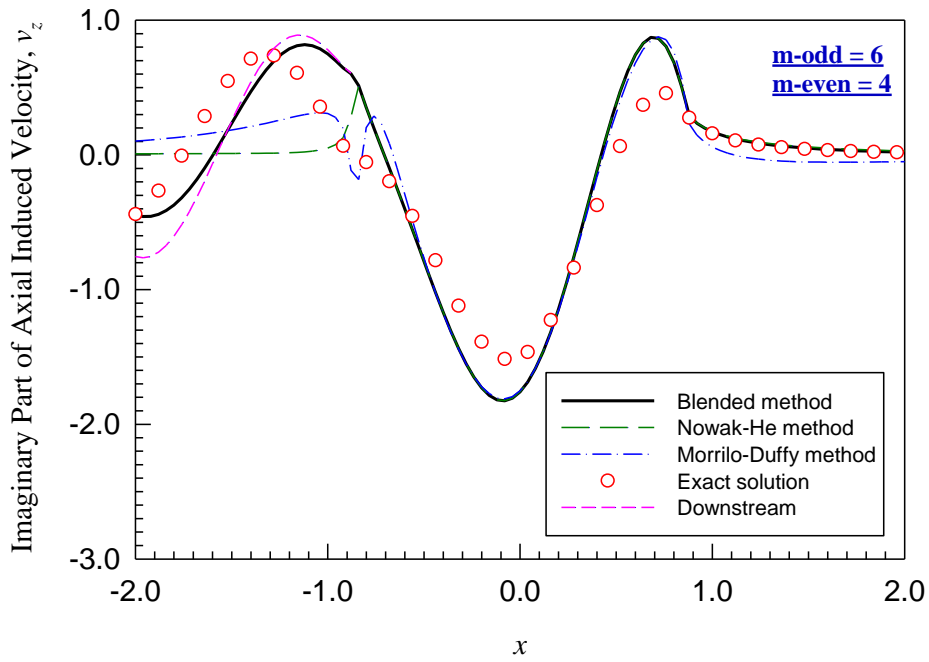
(b)

Figure 4.16 Axial velocity v_z for $y = 0.5$, $z = 0.0$ with τ_1^0 for $\omega = 4$, $\chi = 85^\circ$: (a) real part and (b) imaginary part. (m-odd = 6, m-even = 4)

(a)

(b)
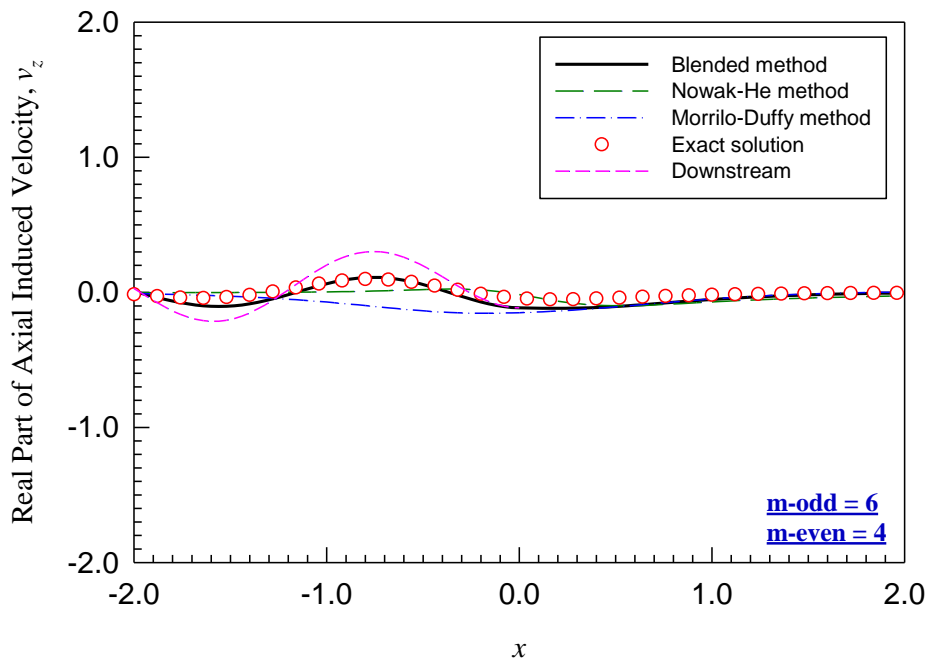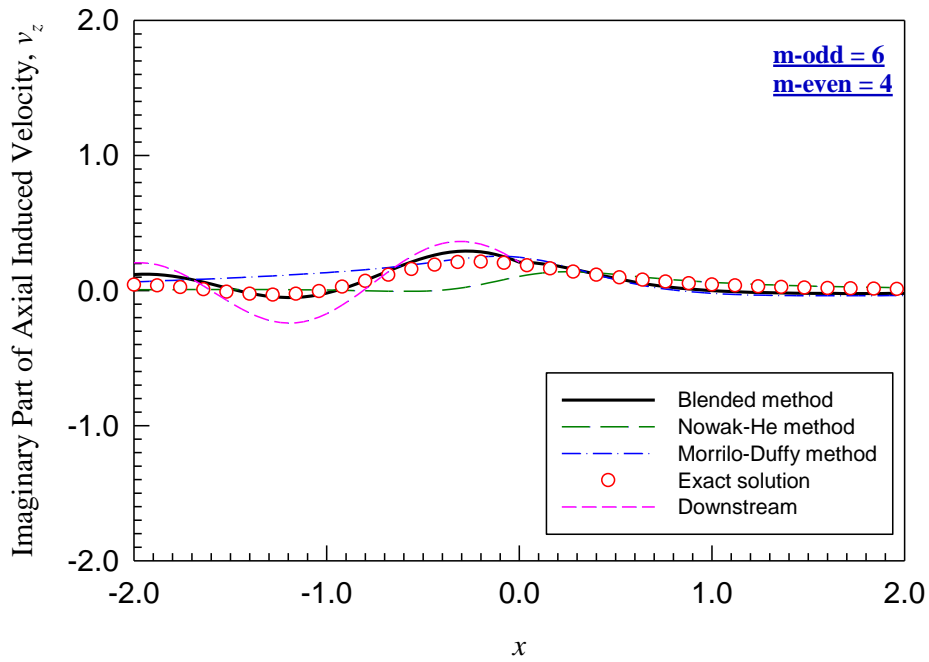
Figure 4.17 Axial velocity v_z for $y = 1.26$, $z = 0.0$ with τ_1^0 for $\omega = 4$, $\chi = 85^\circ$: (a) real part and (b) imaginary part. (m-odd = 6, m-even = 4)
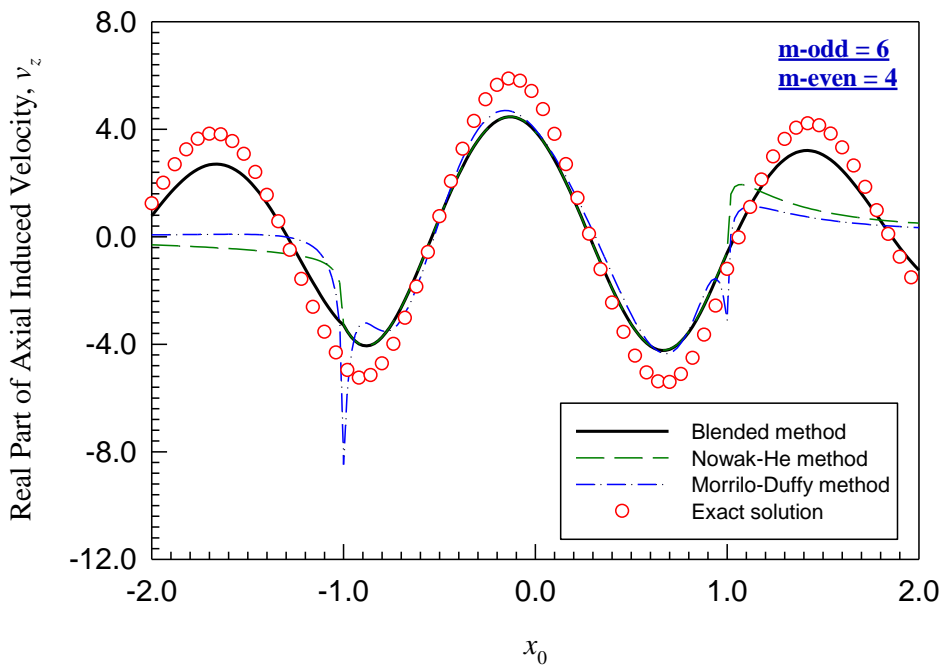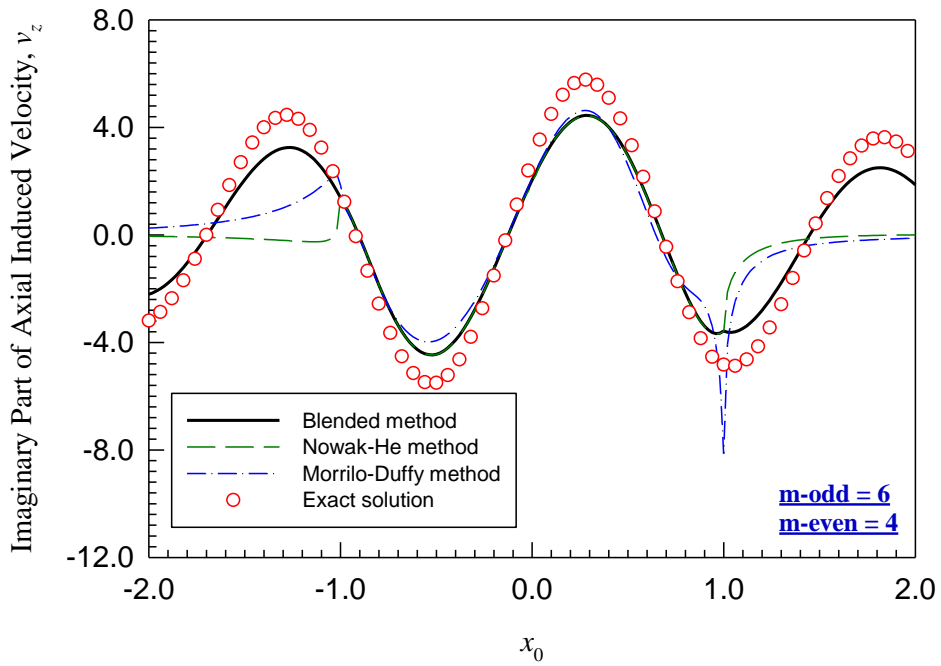

(a)
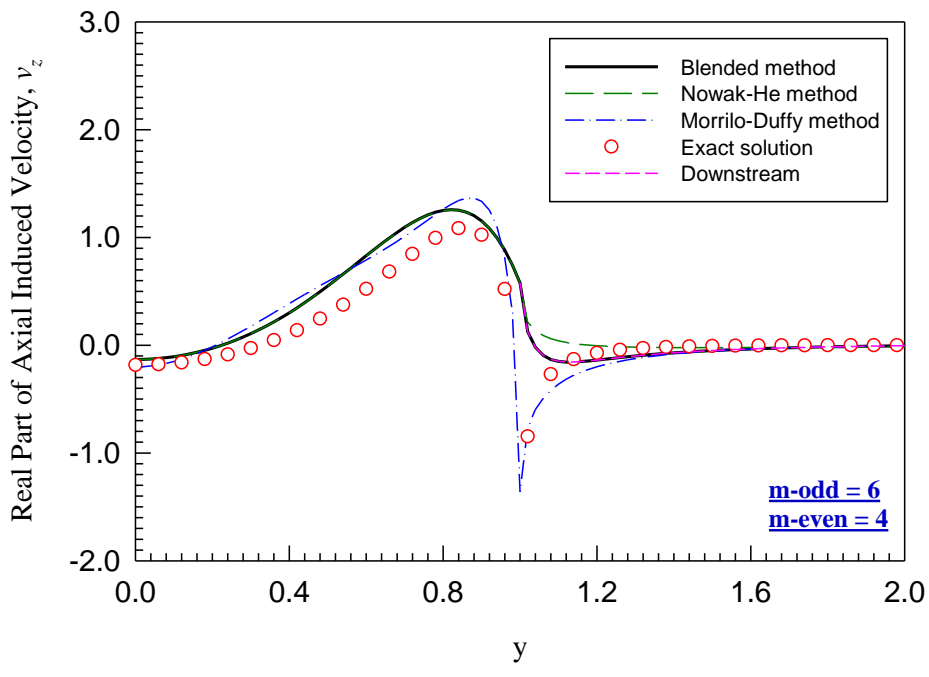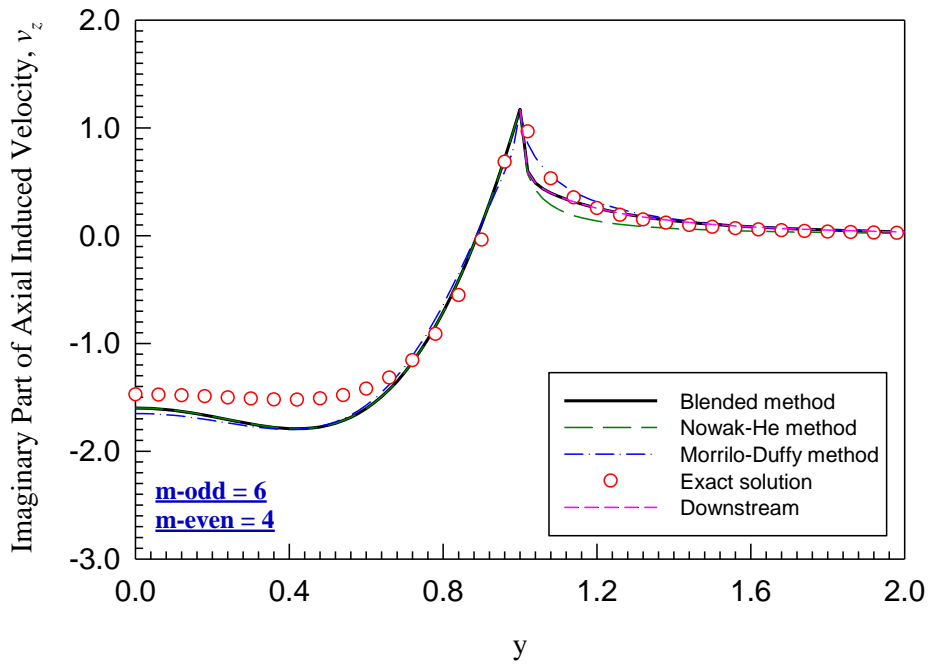
(b)

Figure 4.18 Axial velocity v_z for $x = 0.0$, $z = 0.0$ with τ_1^0 for $\omega = 4$, $\chi = 85°$: (a) real part and (b) imaginary part. (m-odd = 6, m-even = 4)
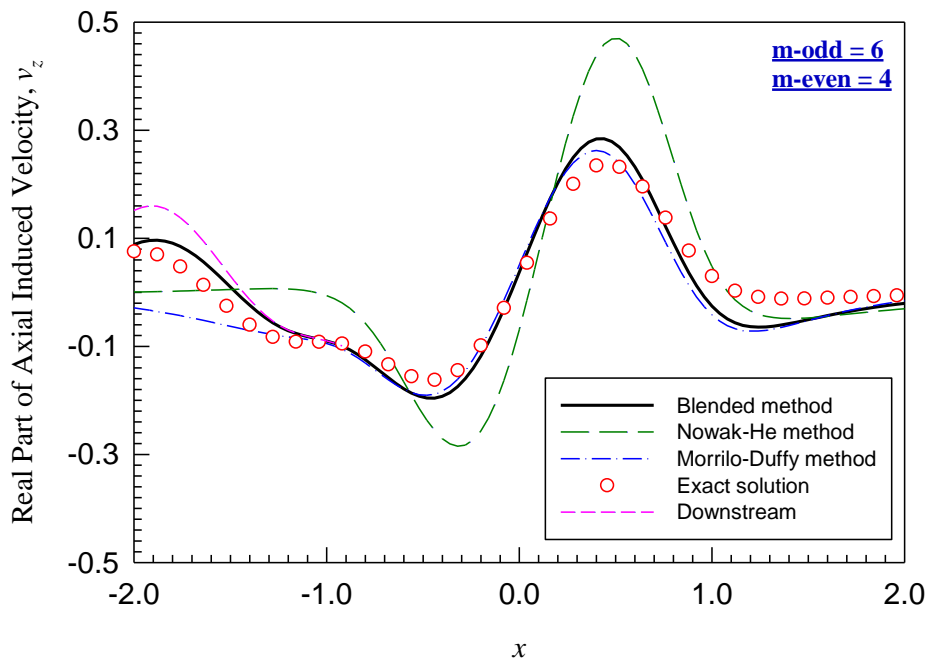
(a)
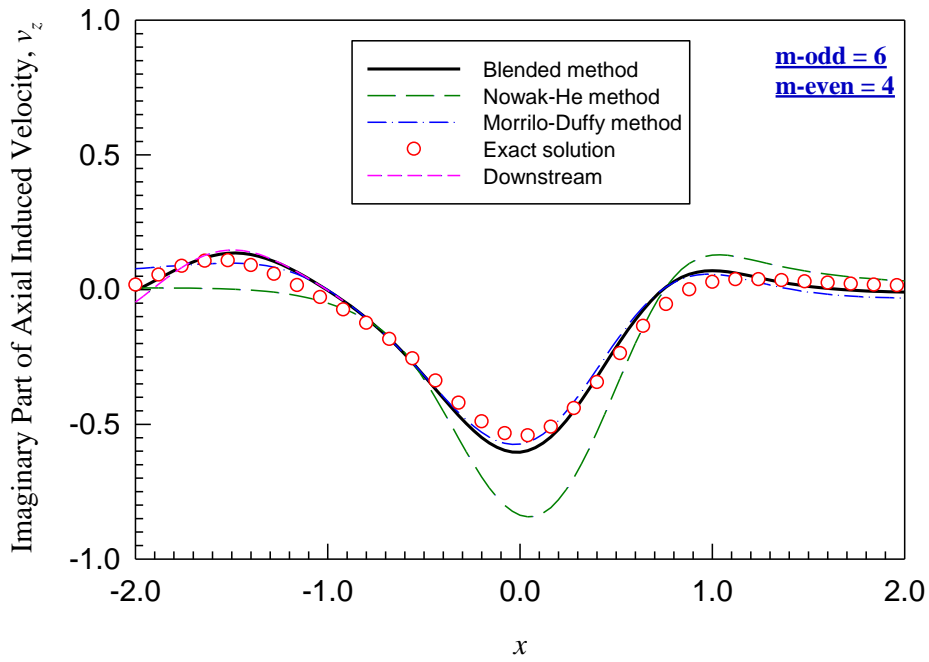
(b)

Figure 4.19 Axial velocity v_z for $y = 0.0$, $z = -0.4$ with τ_1^0 for $\omega = 4$, $\chi = 85^{\circ}$: (a) real part and (b) imaginary part. (m-odd = 6, m-even = 4)
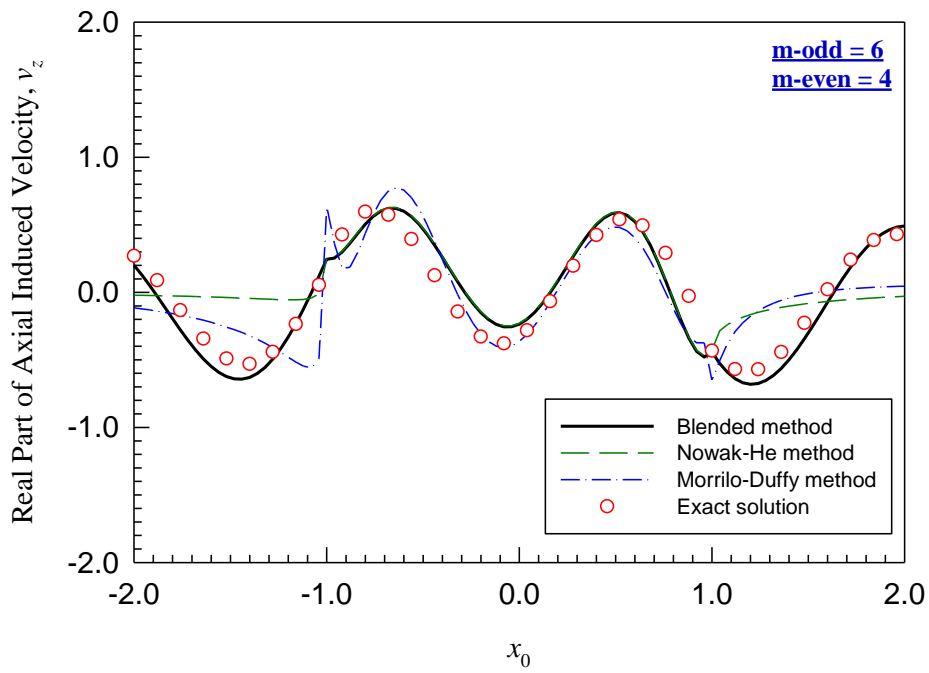
(a)
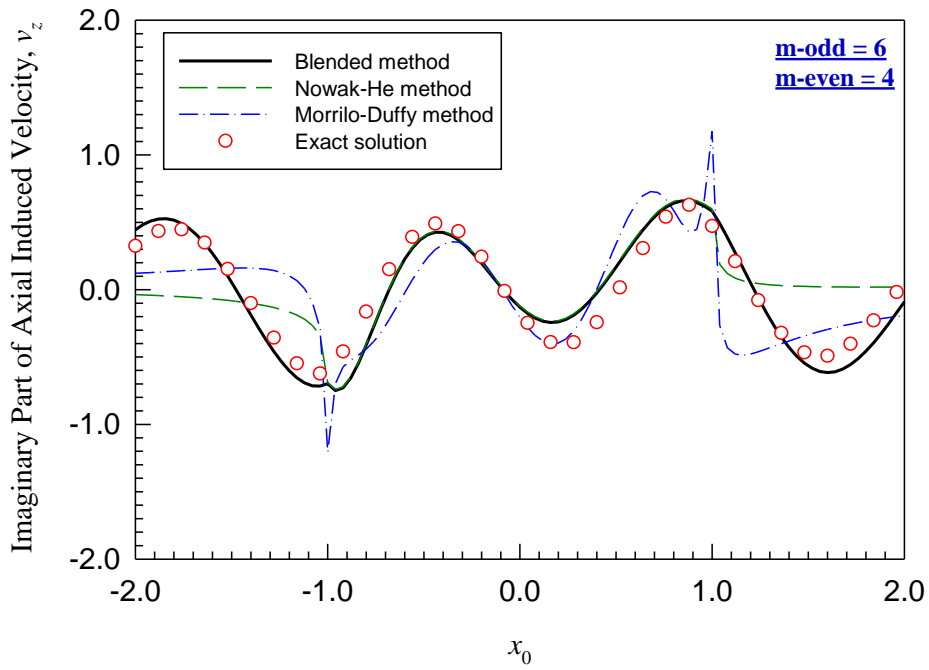
(b)

Figure 4.20 Axial velocity v_z for $y = 0.0$, $z = 0.4$ with τ_1^0 for $\omega = 4$, $\chi = 85^\circ$: (a) real part and (b) imaginary part. (m-odd = 6, m-even = 4)
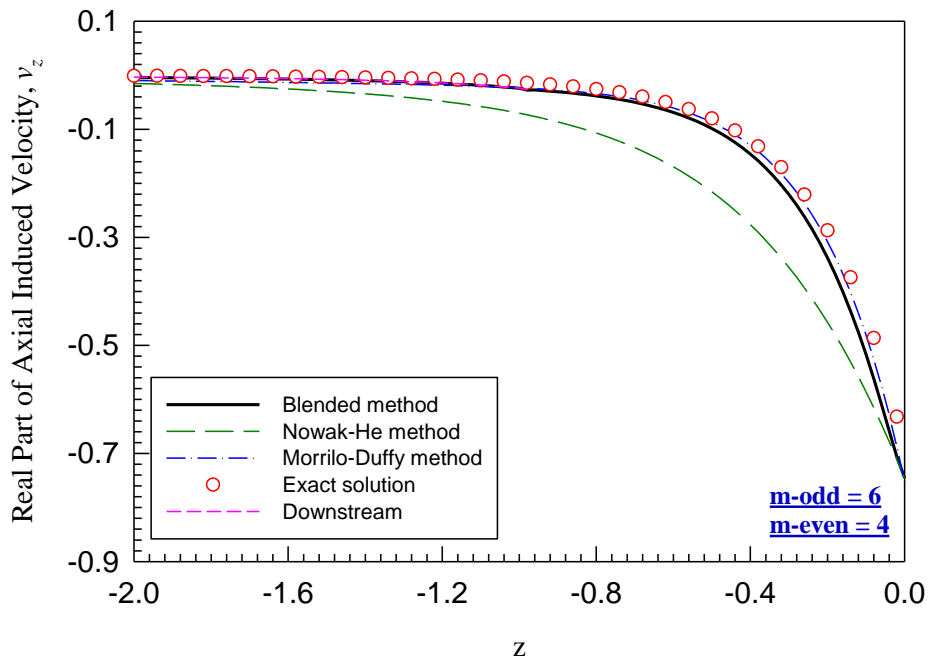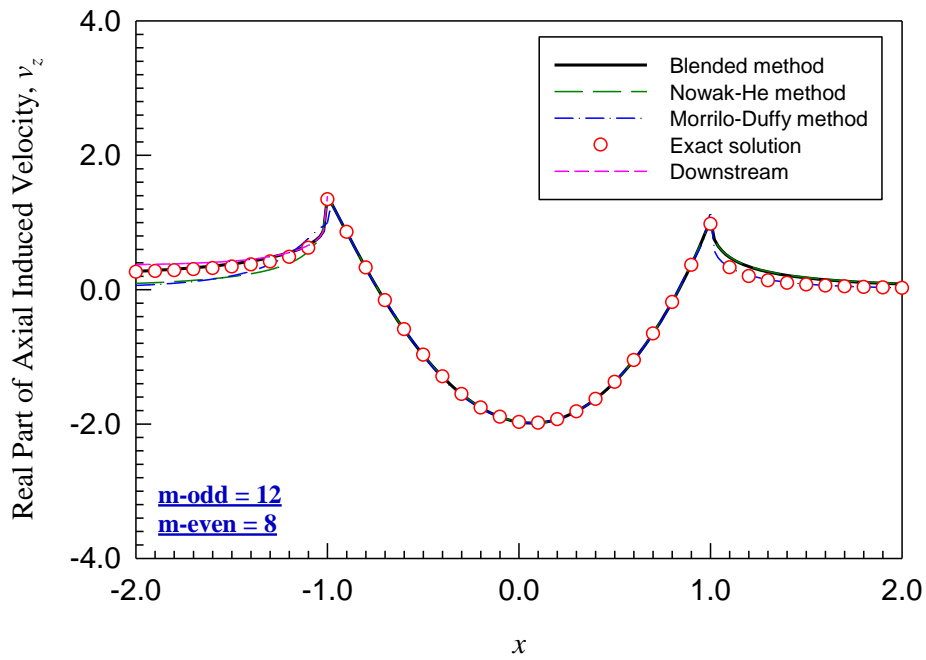

(a)

(b)

Figure 4.21 Axial velocity v_z for $x = -0.25$, $y = 0.0$ with τ_1^0 for $\omega = 4$, $\chi = 85^\circ$: (a) real part and (b) imaginary part. (m-odd = 6, m-even = 4)

Figure 4.22 Real part of axial velocity v_z for y = 0.0, $z = 0.0$ with τ_3^0 for $\omega = 0$, $\chi = 85^\circ$. (m-odd = 12, m-even = 8)
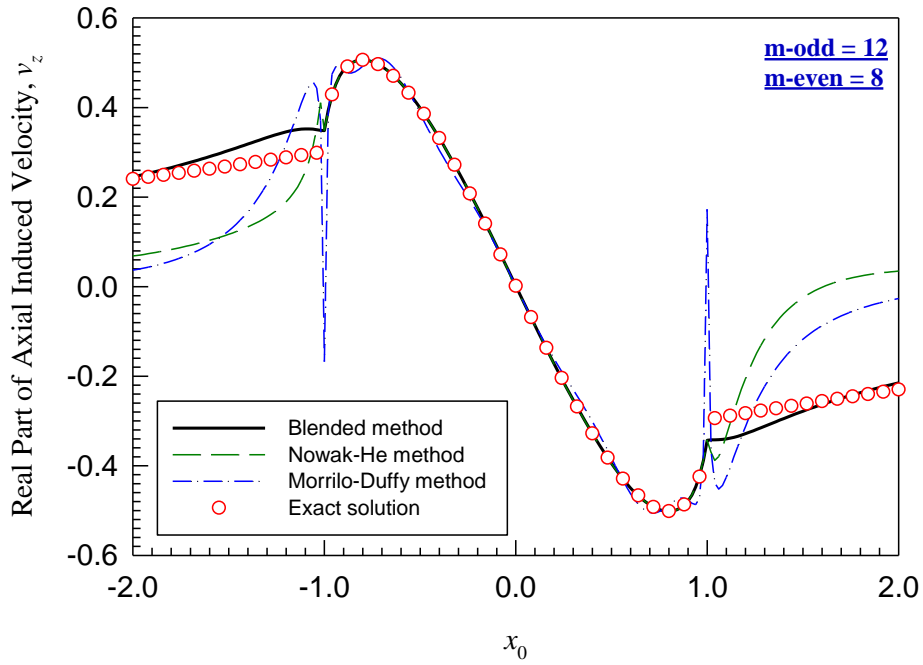
65

Figure 4.23 Real part of axial velocity v_z for y = 0.0, z = 0.4 with τ_3^0 for $\omega = 0$, $\chi = 85^o$. (m-odd = 12, m-even = 8)

(a)

66
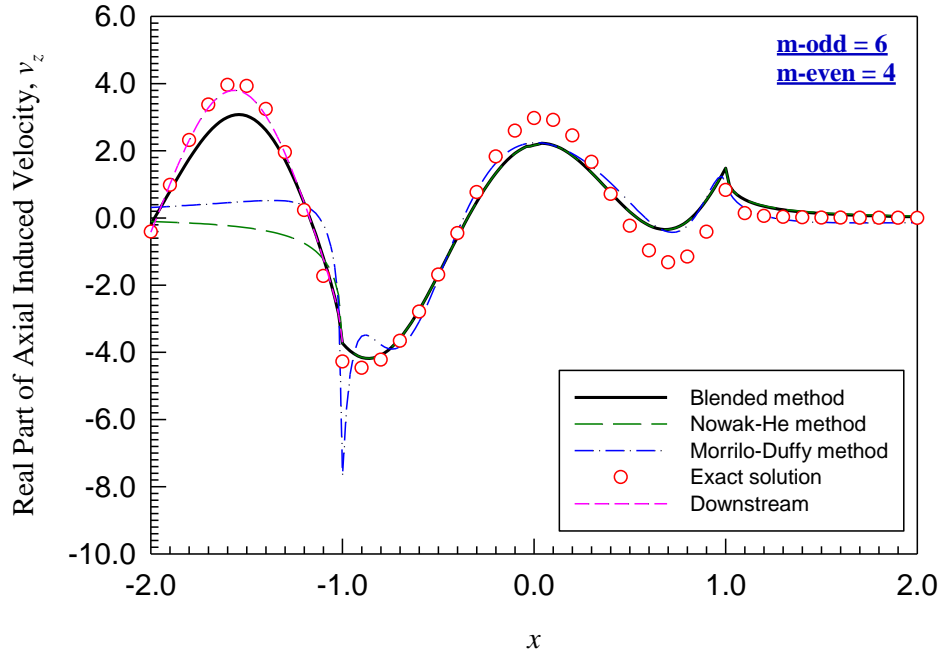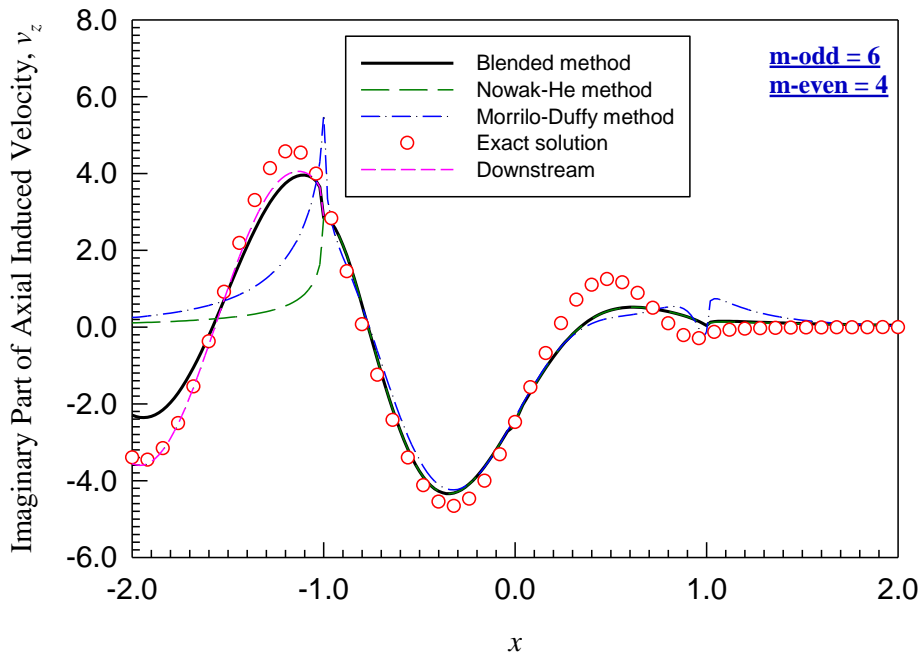
(b)

Figure 4.24 Axial velocity v_z for y = 0.0, z = 0.0 with τ_3^0 for $\omega = 4$, $\chi = 85^\circ$: (a) real part and (b) imaginary part. (m-odd = 6, m-even = 4)
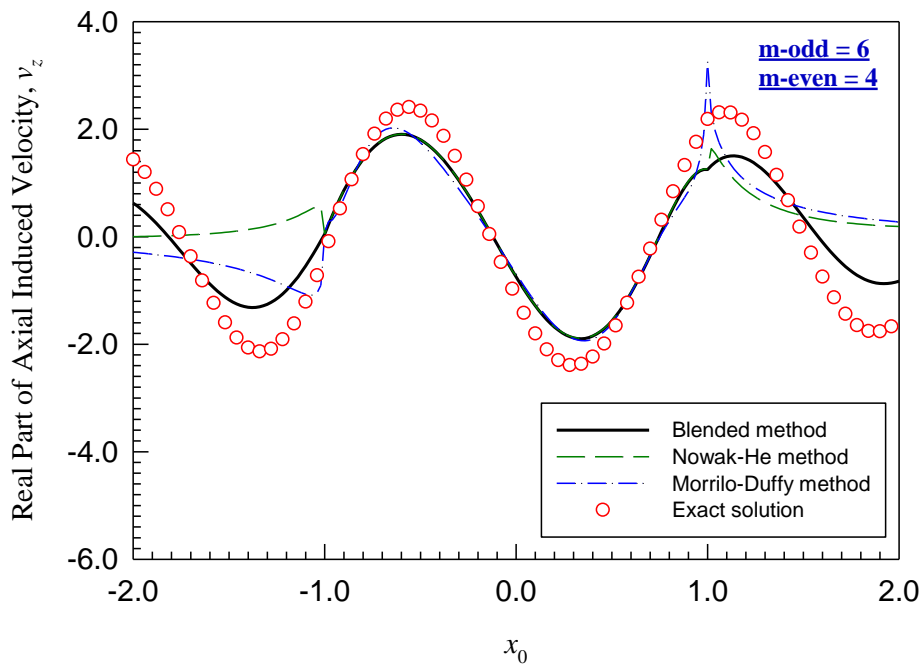

(a)

(b)

Figure 4.25 Axial velocity v_z for y = 0.0, z = 0.4 with τ_3^0 for $\omega = 4$, $\chi = 85^o$: (a) real part and (b) imaginary part. (m-odd = 6, m-even = 4)

Figure 4.26 Real part of axial velocity v_z for y = 0.0, z = 0.0 with τ_2^1 for $\omega = 0$, $\chi = 85^o$. (m-odd = 12, m-even = 8)

Figure 4.27 Real part of axial velocity v_z for y = 0.0, $z = 0.4$ with τ_2^1 for $\omega = 0$, $\chi = 85^o$. (m-odd = 12, m-even = 8)
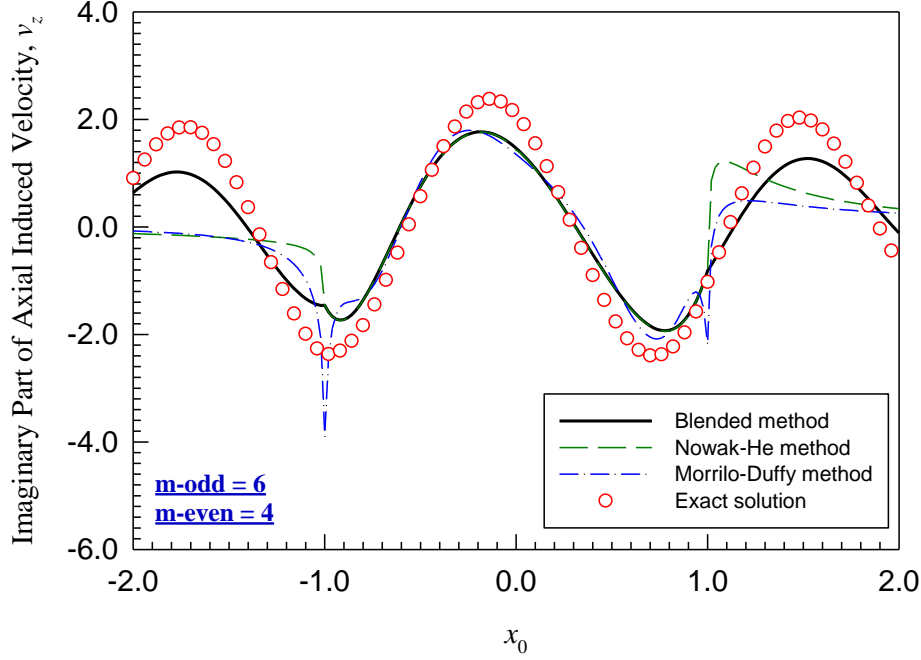

(a)

69
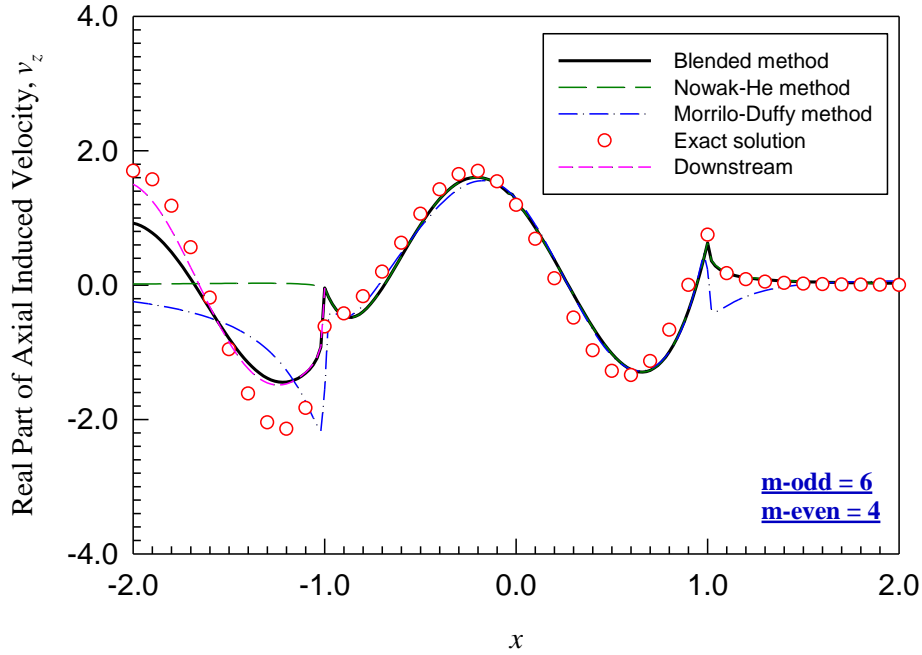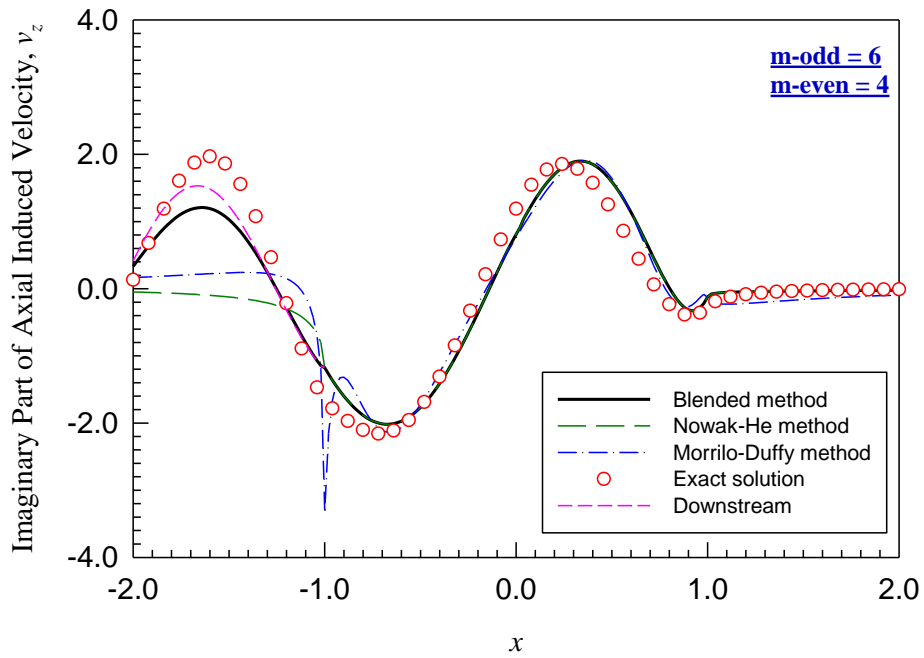
(b)

Figure 4.28 Axial velocity v_z for y = 0.0, z = 0.0 with τ_2^1 for ω = 4, χ = 85°: (a) real part and (b) imaginary part. (m-odd = 6, m-even = 4)

(a)

(b)

Figure 4.29 Axial velocity v_z for y = 0.0, z = 0.4 with τ_2^1 for ω = 4, χ = 85°: (a) real part and (b) imaginary part. (m-odd = 6, m-even = 4)

4.4.2 In-plane Component of the Induced Velocity

Since the x and y component of the induced velocity are computed in a similar manner, only the x component of the in-plane induced velocity will be illustrated herein. With the blending method discussed in the previous sections, some typical results which the pressure distribution on the rotor disk is elliptical are presented in Figs. 4.30−4.39. All of the results are obtained with 12 harmonics for the odd terms and 8 harmonics for the even terms, except for the results with ω = 4 and χ = 85°. For ω = 4 and χ = 85°, 6 harmonics for the odd terms and 4 harmonics for the even terms will be adopted.

In Figs. 4.30−4.34, the results for ω = 0 (constant loading) are illustrated. For ω = 0, the solutions have no imaginary part. Figures 4.30 and 4.31 give the x component of induced velocity at the rotor disk (y = 0 and z = 0) for skew angle at 30° and 85°. For χ = 85° in Fig.

71

4.31, the Morillo-Duffy solution has large discrepancy away from the rotor disk compared with the exact solution, and it has spike around the edge of disk. The Huang-He solution has less oscillation within on-disk region, and the downstream velocity is more accurate away the disk for such skew angle. While those three solution are combined together, the results get improved obviously everywhere. Figure 4.32 presents a y-transverse, and for $|y| \geq 1$, the induced velocity is zero. In Fig. 4.33, the velocity above the disk ($z = -0.4$) varying x is plotted. Results below the disk ($z = 0.4$) are plotted from the center of the skewed wake versus x_0, which is the x location on the rotor disk through which a streamline would pass. Therefore, $x_0 = 0$ is the streamline going through the rotor center. All of these results give good convergence compared with the exact solution.

Similarly, another five cases for $\omega = 4$ (frequency $= 4V_\infty / R$) are presented in Figs. 4.35−4.39. The results for both real part (in-phase velocity) and imaginary part (out-of-phase velocity) of the induced velocity computed via the blended method agree with the exact solution very well both upstream and downstream, above the rotor disk and below the disk. The same trend persists as were found for the steady case.

For other pressure distribution τ_3^0 and τ_2^1, the results with blending method proposed above which is shown in Figs. 4.40−4.47 also perform very well. Therefore, it is evident that the blending is robust in all situations.
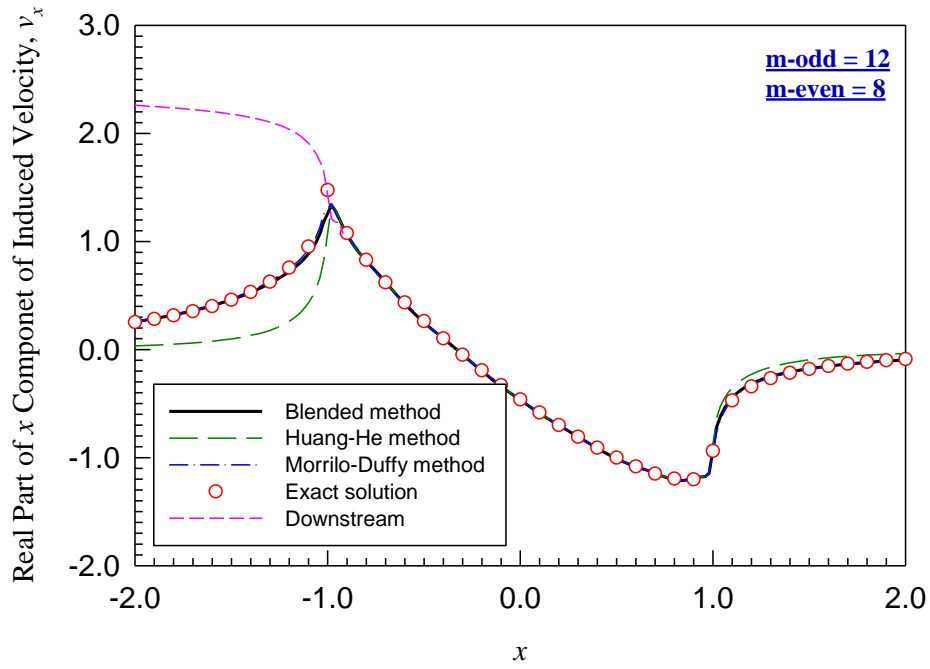
Figure 4.30 Real part of x component of induced velocity v_x for y = 0.0, z = 0.0 with τ_1^0 for $\omega = 0$, $\chi = 30^\circ$. (m-odd = 12, m-even = 8)
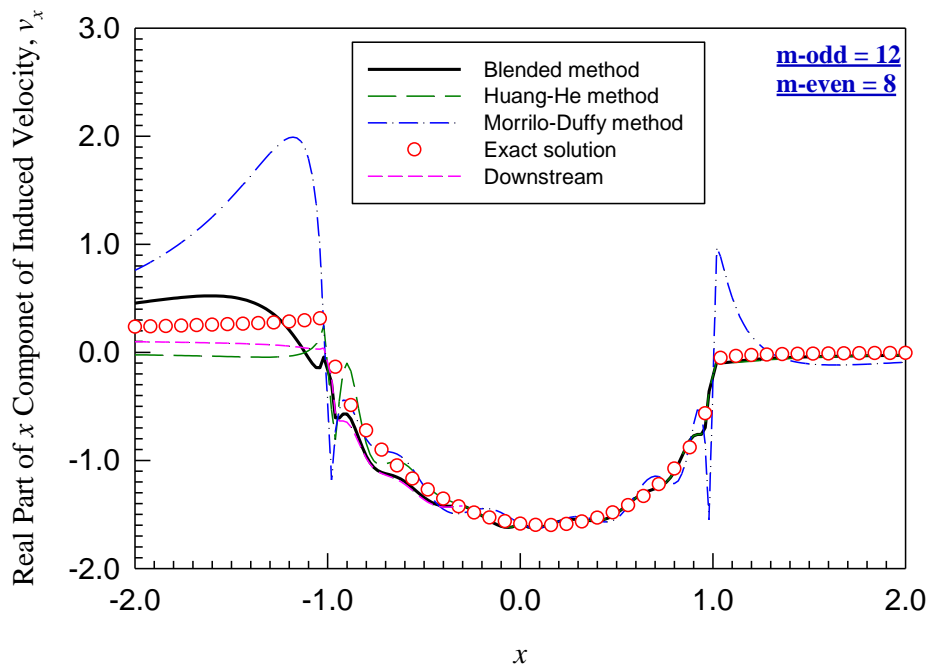

Figure 4.31 Real part of x component of induced velocity v_x for y = 0.0, z = 0.0 with τ_1^0 for $\omega = 0$, $\chi = 85^\circ$. (m-odd = 12, m-even = 8)
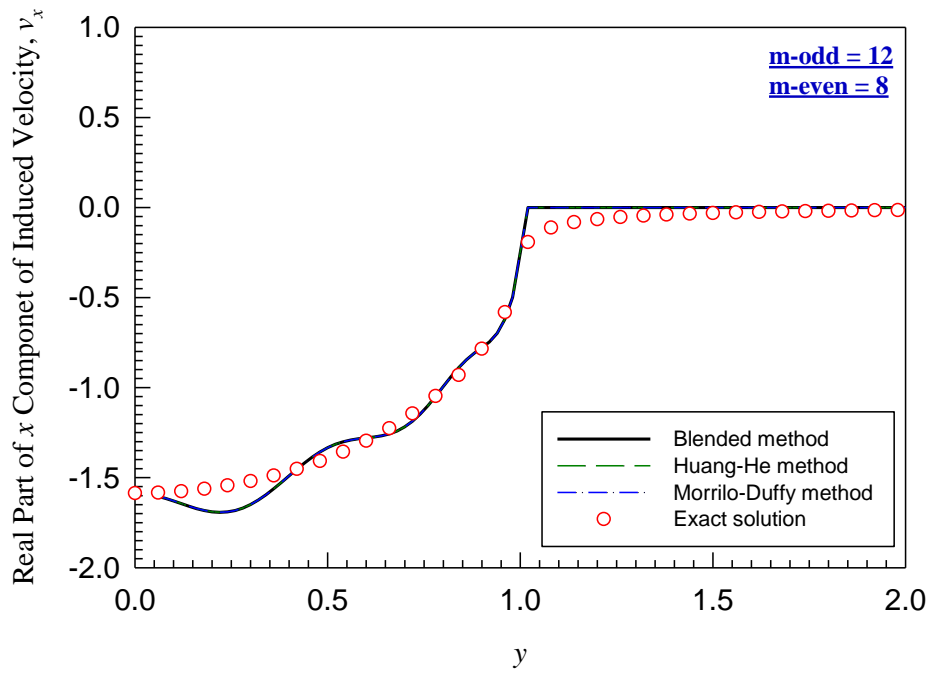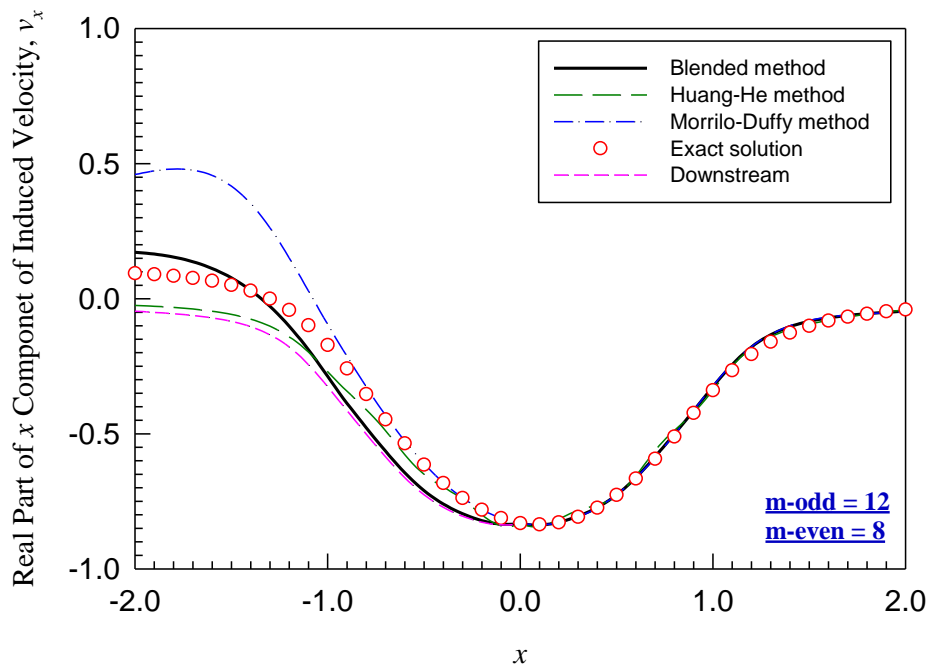
Figure 4.32 Real part of x component of induced velocity v_x for x = 0.0, z = 0.0 with τ_1^0 for $\omega = 0$, $\chi = 85^\circ$. (m-odd = 12, m-even = 8)

Figure 4.33 Real part of x component of induced velocity v_x for y = 0.0, z = -0.4 with τ_1^0 for $\omega = 0$, $\chi = 85^\circ$. (m-odd = 12, m-even = 8)
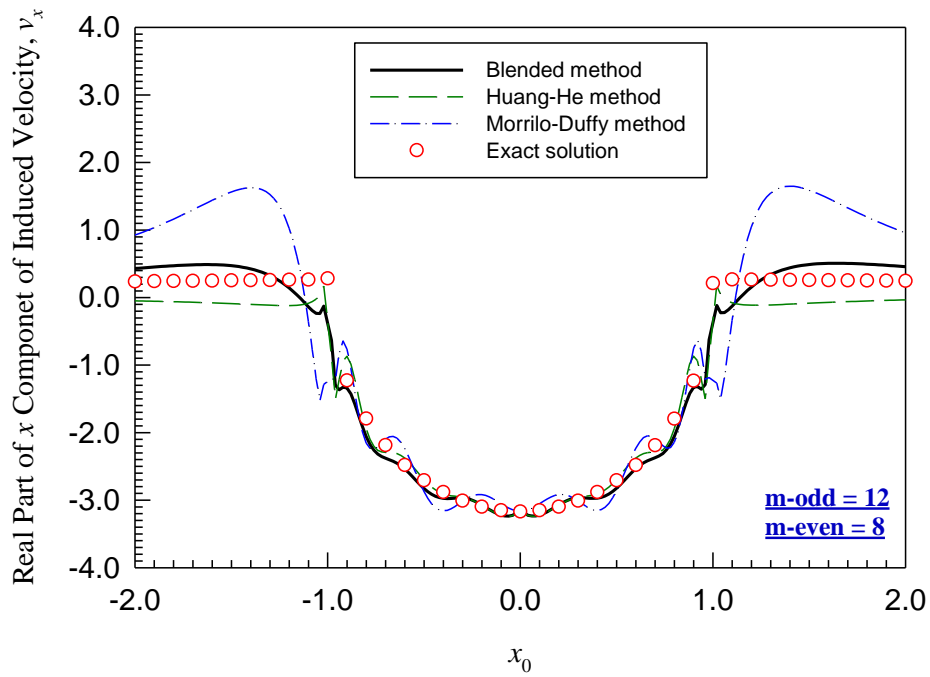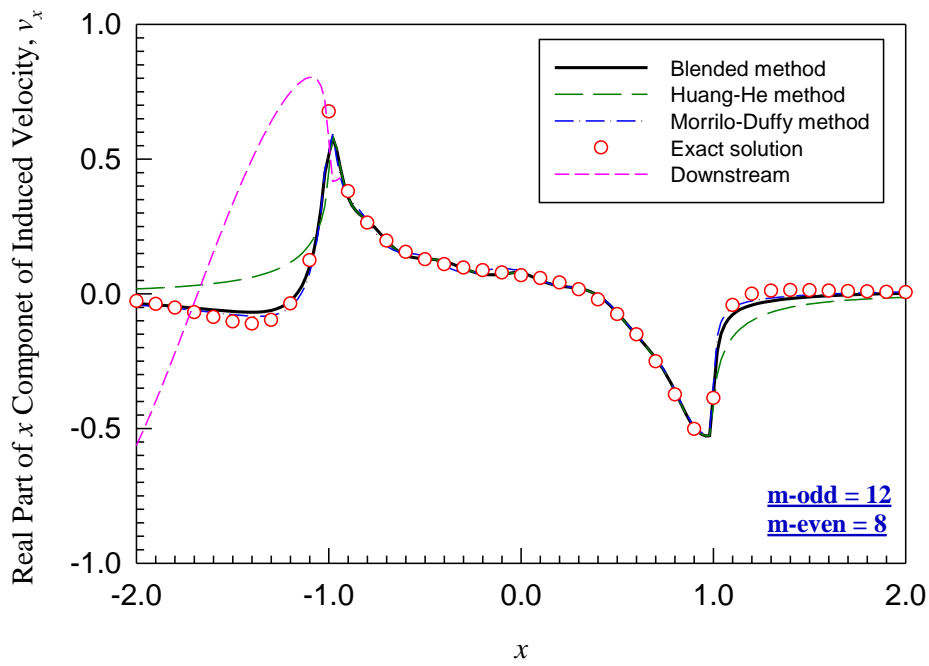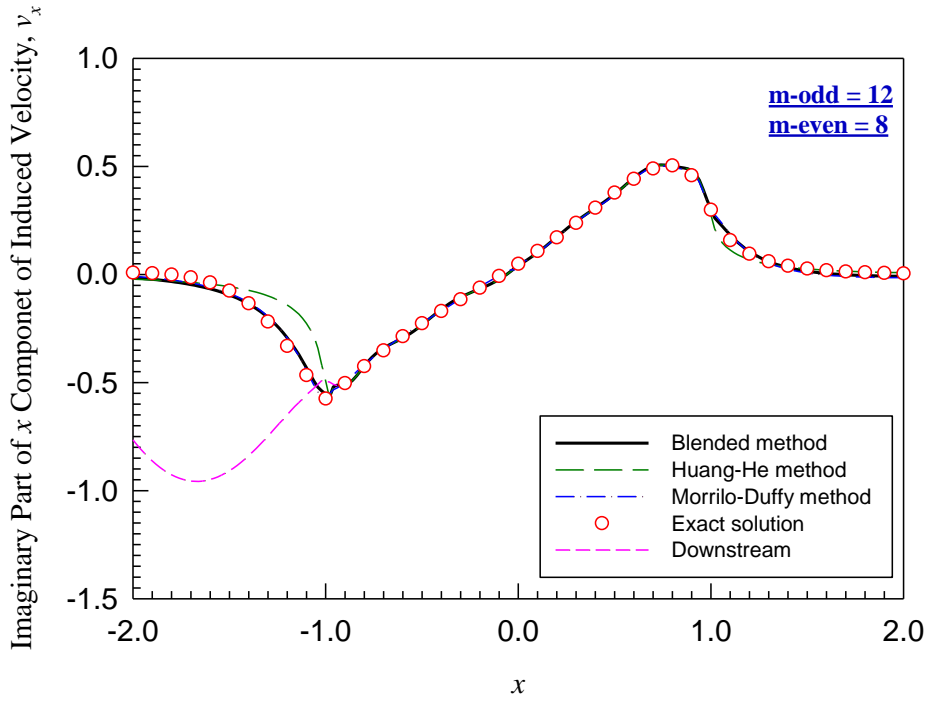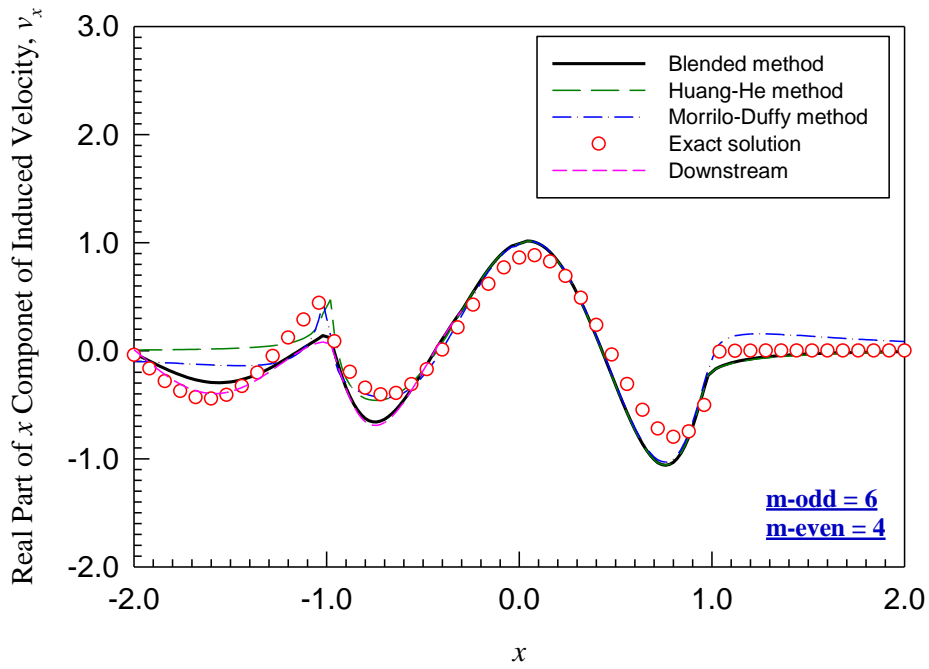
Figure 4.34 Real part of x component of induced velocity v_x for y = 0.0, z = 0.4 with τ_1^0 for ω = 0, χ = 85°. (m-odd = 12, m-even = 8)
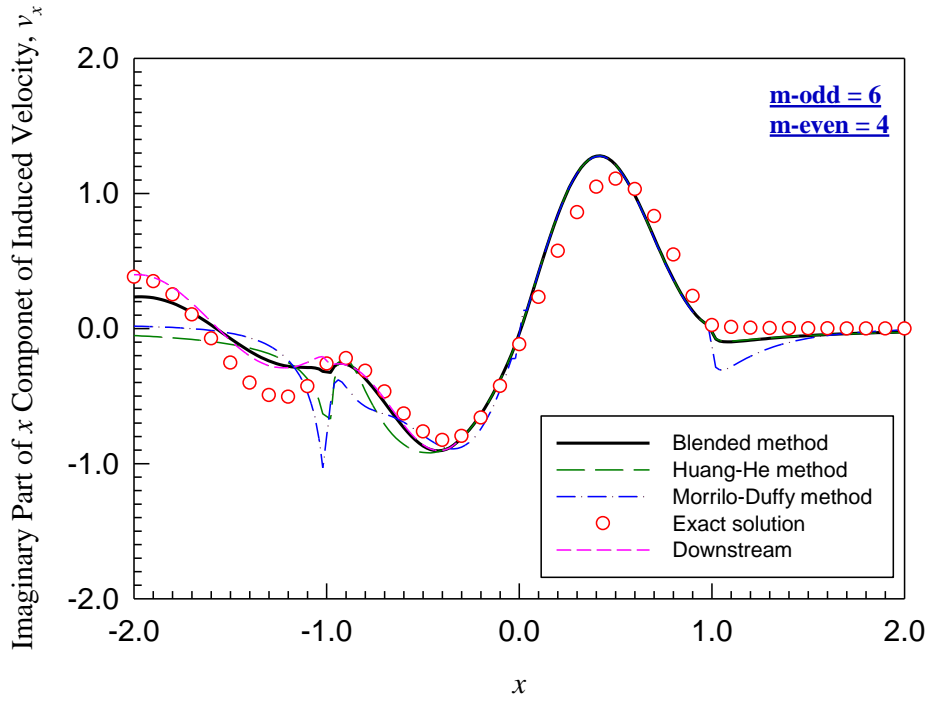

(a)

(b)

Figure 4.35 x component of induced velocity v_x for y = 0.0, z = 0.0 with τ_1^0 for ω = 4, χ = 30°: (a) real part and (b) imaginary part. (m-odd = 12, m-even = 8)

(a)

(b)

Figure 4.36 x component of induced velocity v_x for y = 0.0, z = 0.0 with τ_1^0 for ω = 4, χ = 85°: (a) real part and (b) imaginary part. (m-odd = 6, m-even = 4)

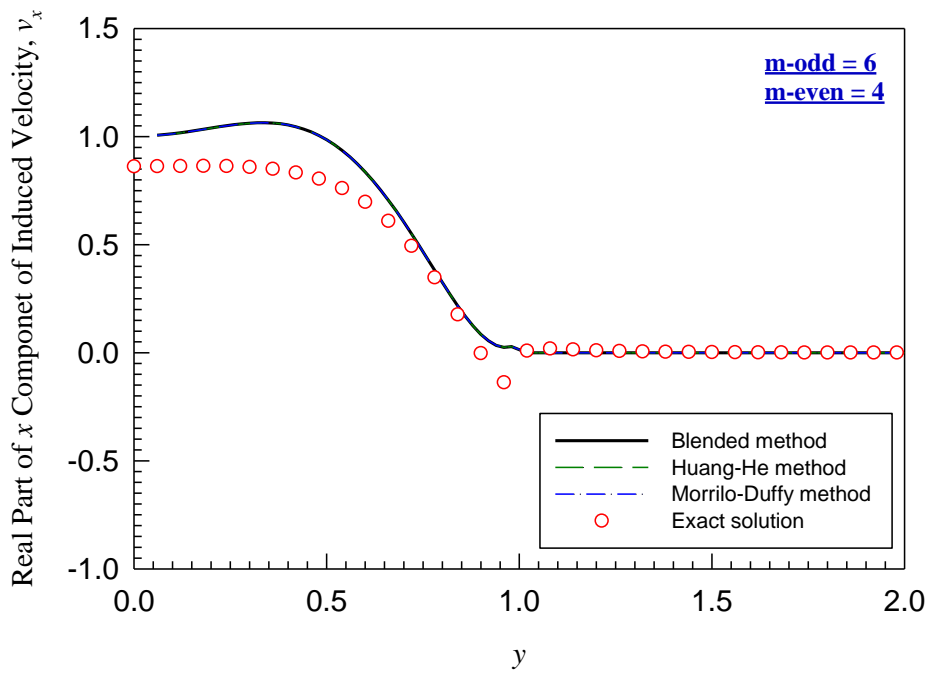

(a)

(b)

Figure 4.37 x component of induced velocity V_x for x = 0.0, z = 0.0 with τ_1^0 for ω = 4, χ = 85$^\text{o}$: (a) real part and (b) imaginary part. (m-odd = 6, m-even = 4)

(a)

(b)

Figure 4.38 x component of induced velocity v_x for y = 0.0, z = -0.4 with τ_1^0 for ω = 4, χ = 85°: (a) real part and (b) imaginary part. (m-odd = 6, m-even = 4)
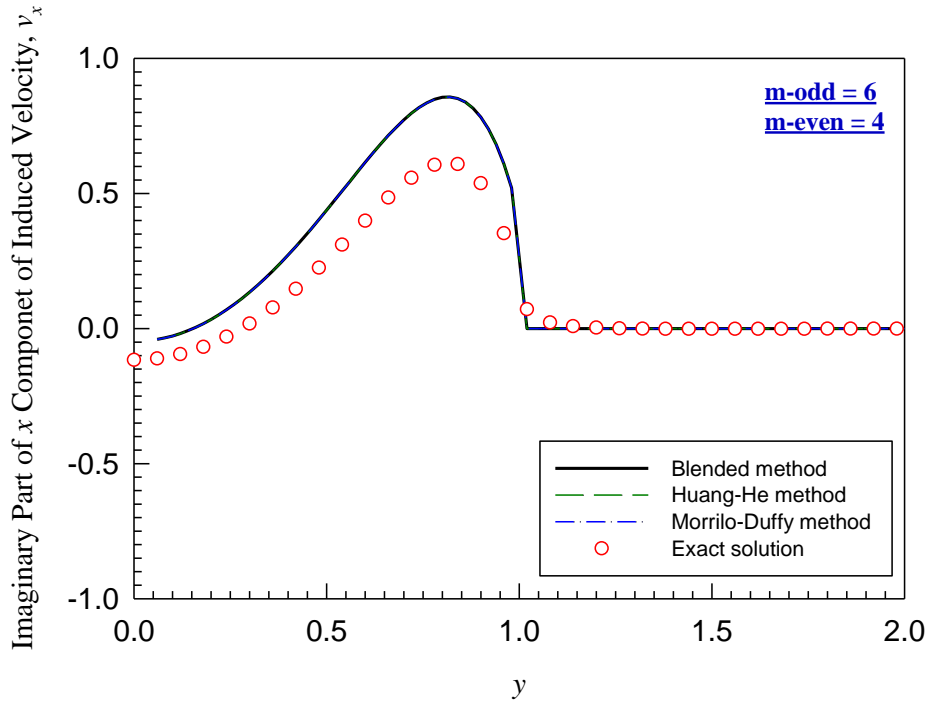

(a)

(b)

Figure 4.39 x component of induced velocity v_x for y = 0.0, z = 0.4 with τ_1^0 for ω = 4, χ = 85°: (a) real part and (b) imaginary part. (m-odd = 6, m-even = 4)
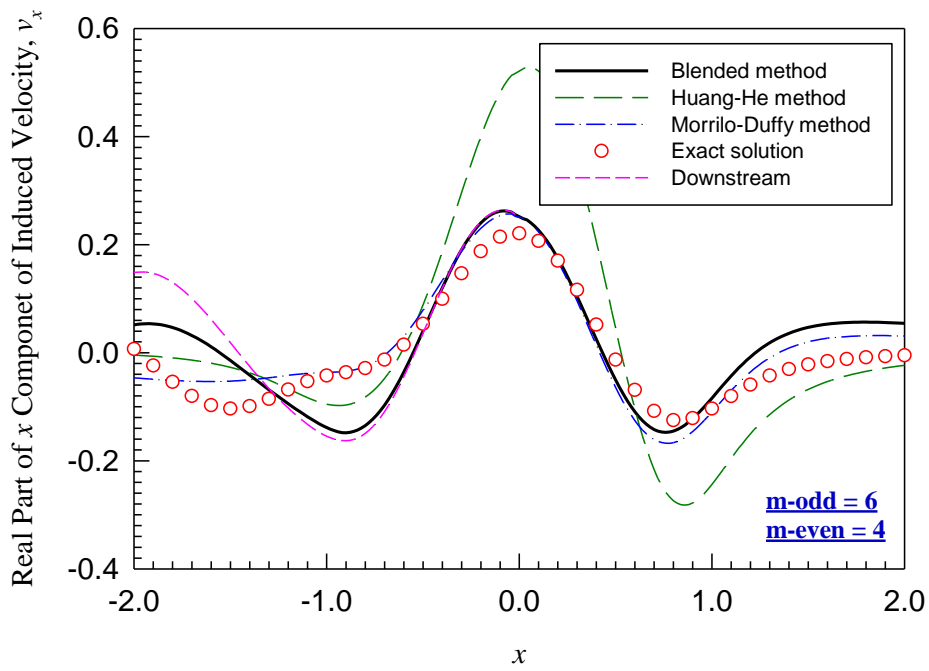

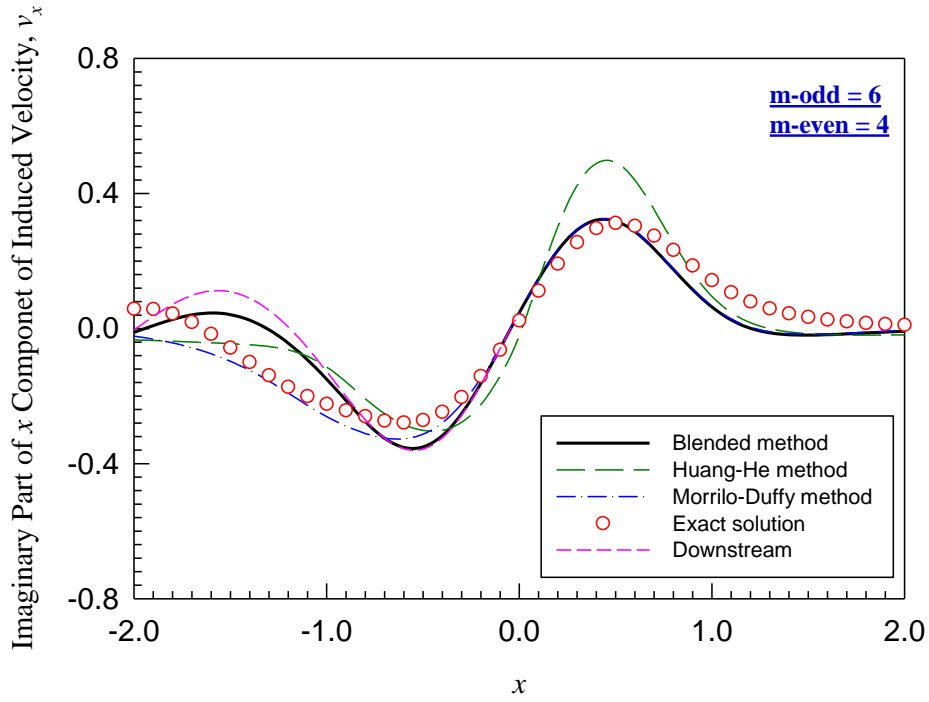Figure 4.40 Real part of x component of induced velocity v_x for y = 0.0, z = 0.0 with τ_3^0 for ω = 0, χ = 85°. (m-odd = 12, m-even = 8)

Figure 4.41 Real part of x component of induced velocity v_x for y = 0.0, z = 0.4 with τ_3^0 for ω = 0, χ = 85°. (m-odd = 12, m-even = 8)

(a)

(b)

Figure 4.42 x component of induced velocity v_x for y = 0.0, z = 0.0 with τ_3^0 for ω = 4, χ = 85°: (a) real part and (b) imaginary part. (m-odd = 6, m-even = 4)

(a)

(b)

Figure 4.43 x component of induced velocity v_x for y = 0.0, $z = 0.4$ with τ_3^0 for $\omega = 4$, $\chi = 85°$: (a) real part and (b) imaginary part. (m-odd = 6, m-even = 4)
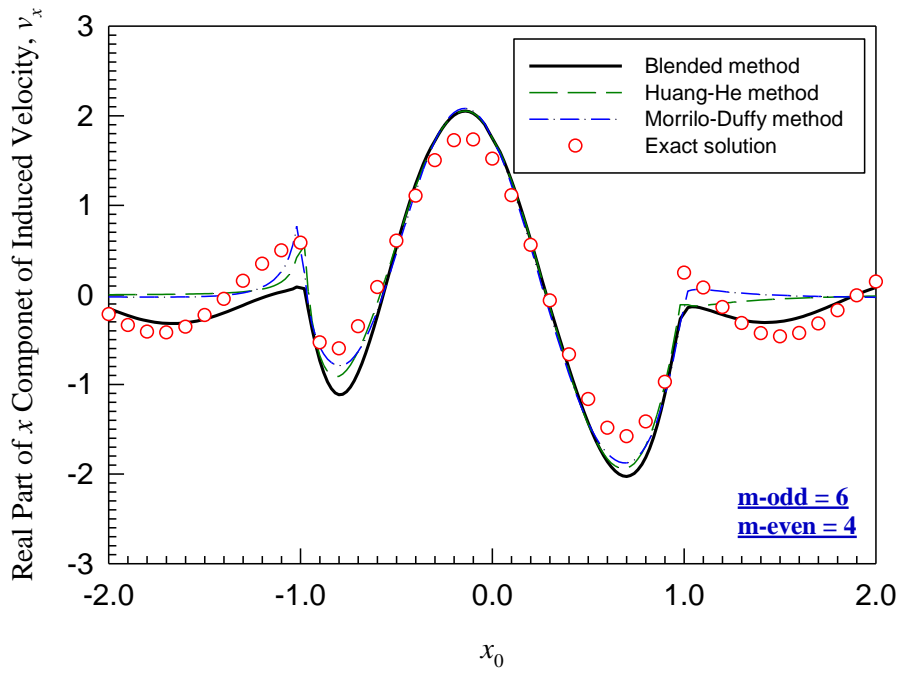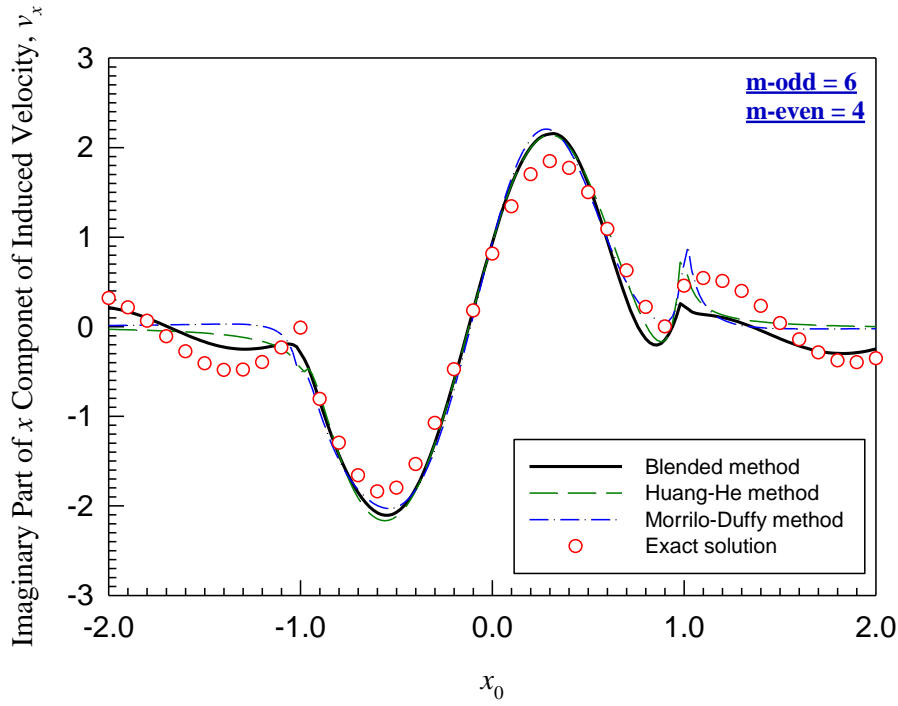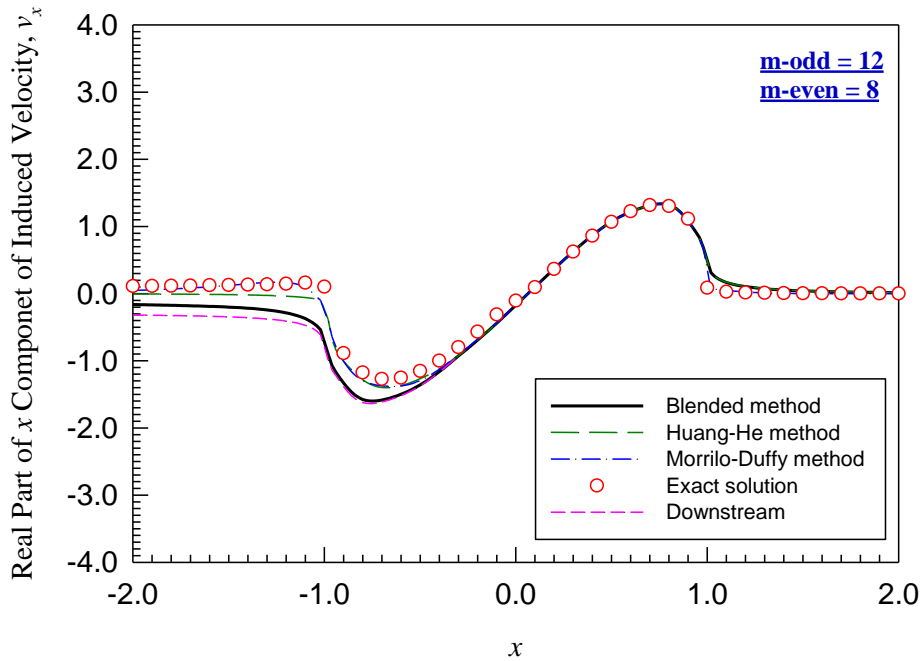

Figure 4.44 Real part of x component of induced velocity v_x for y = 0.0, $z = 0.0$ with τ_2^1 for $\omega = 0$, $\chi = 85°$. (m-odd = 12, m-even = 8)
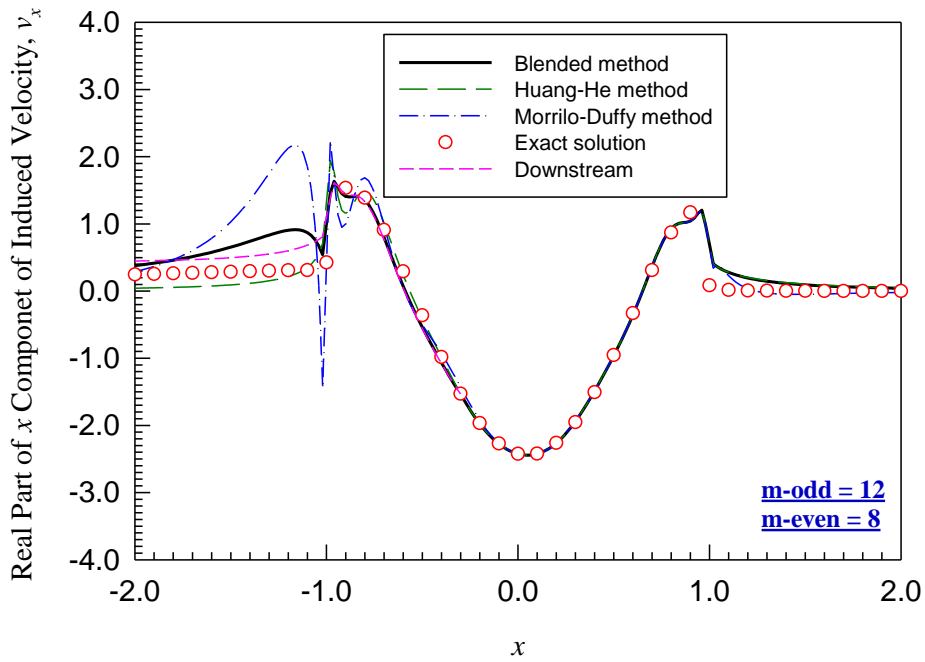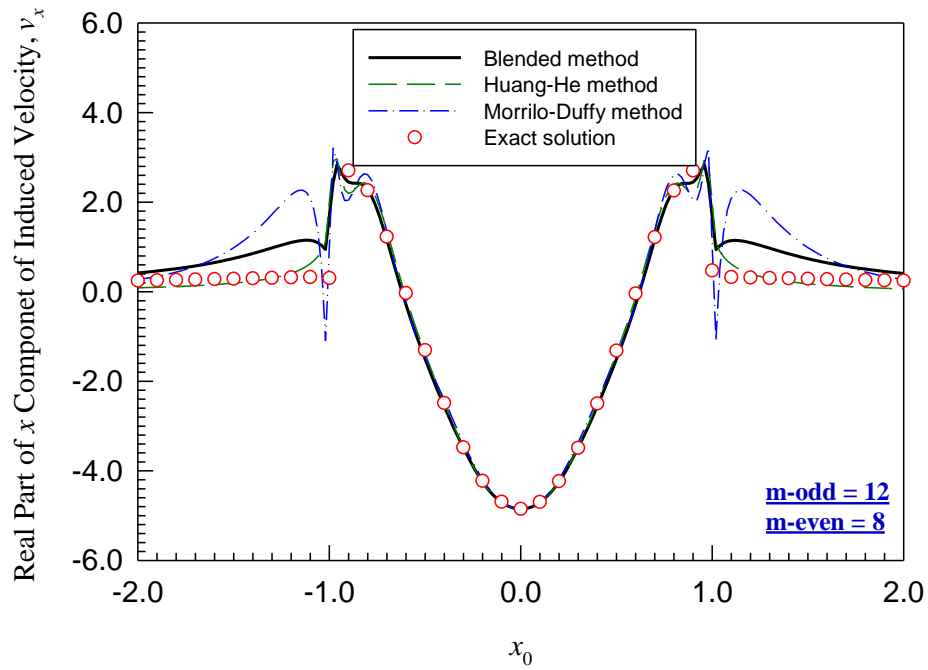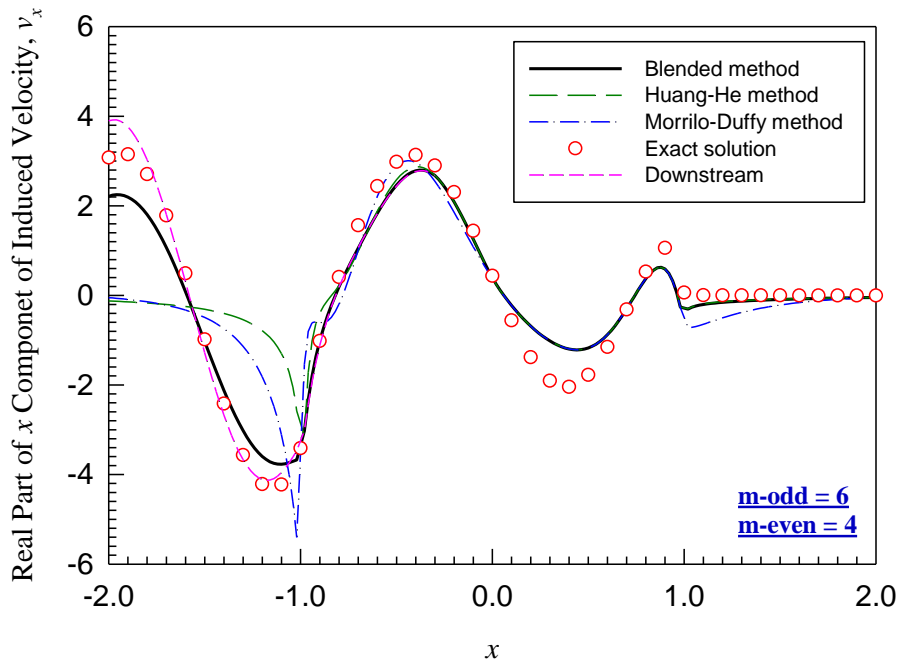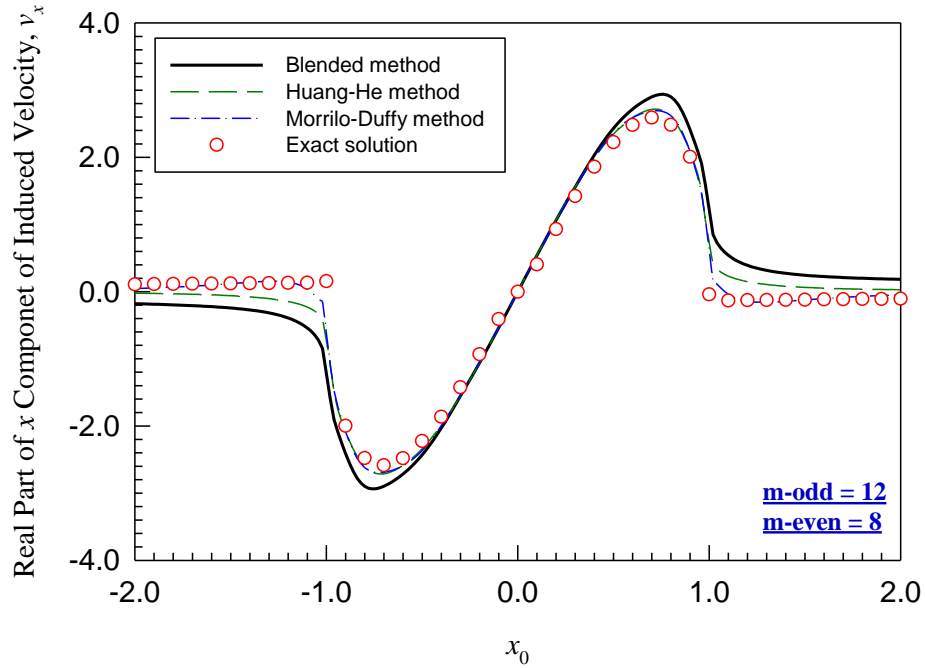
Figure 4.45 Real part of x component of induced velocity v_x for y = 0.0, $z = 0.4$ with τ_2^1 for $\omega = 0$, $\chi = 85^\circ$. (m-odd = 12, m-even = 8)
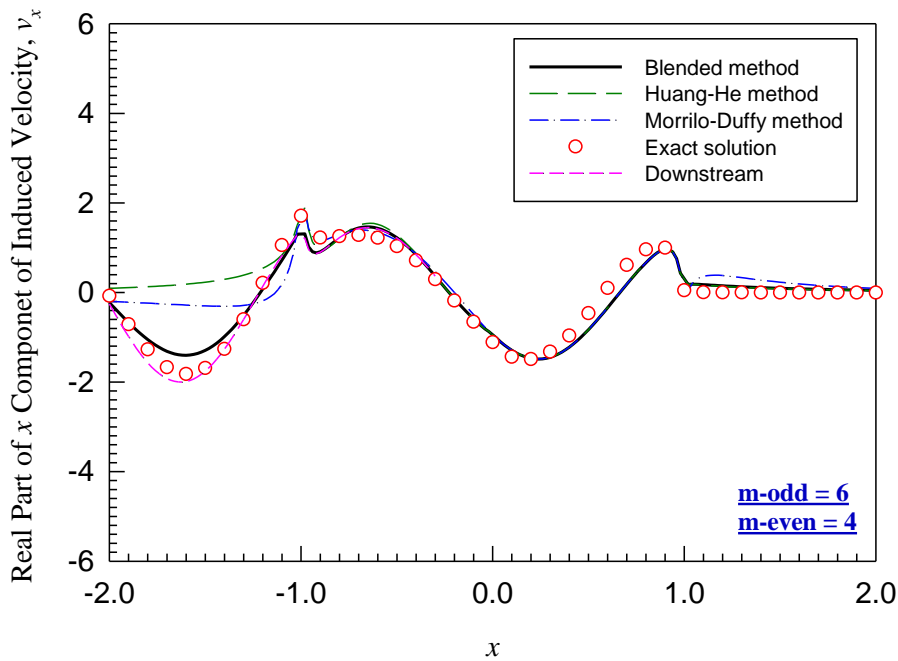
(a)
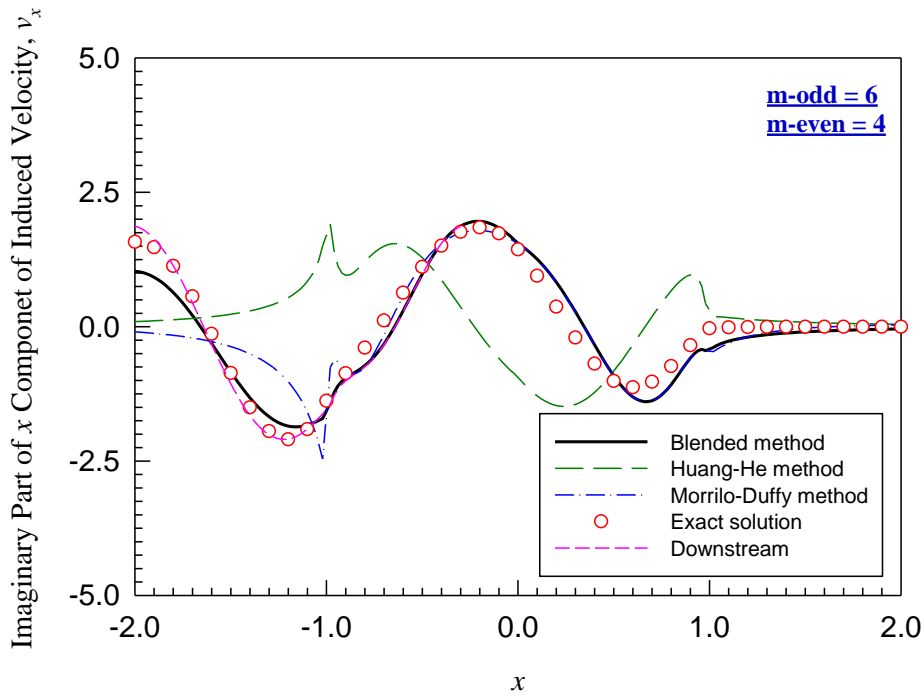
(b)

Figure 4.46 x component of induced velocity v_x for y = 0.0, z = 0.0 with τ_2^1 for ω = 4, χ = 85°: (a) real part and (b) imaginary part. (m-odd = 6, m-even = 4)
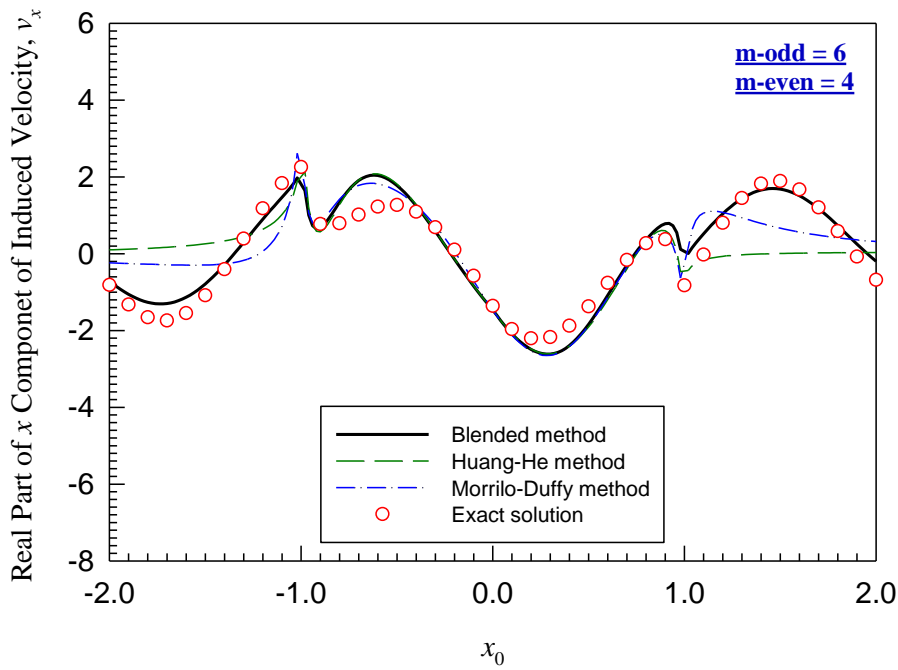
(a)
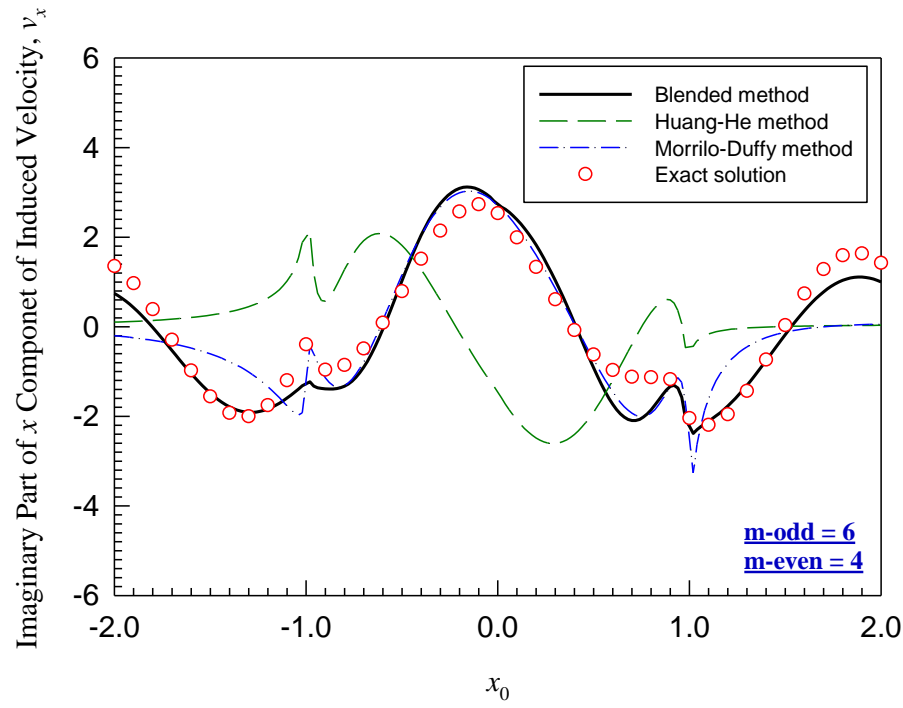
(b)
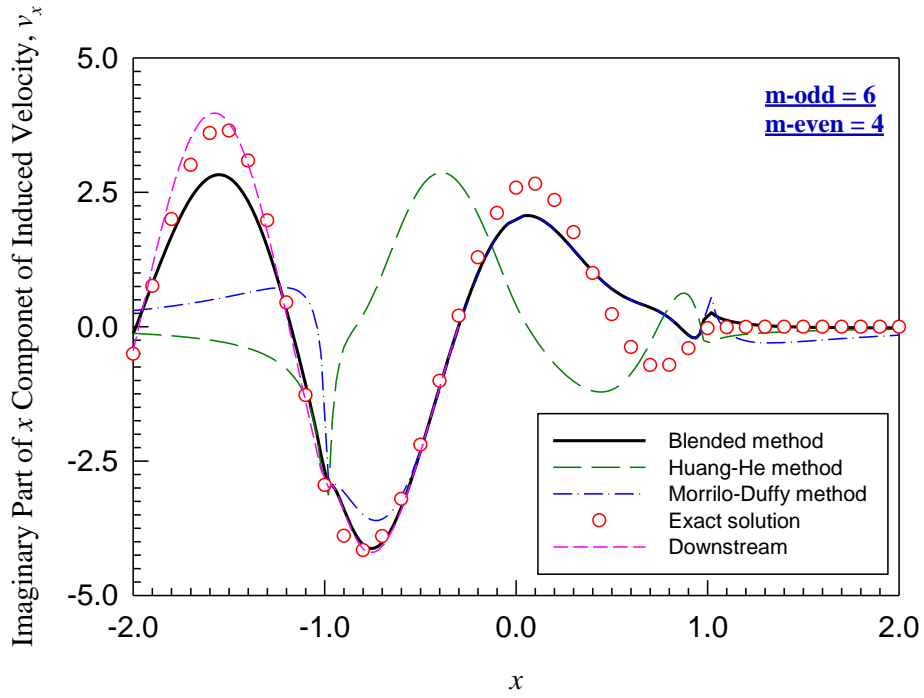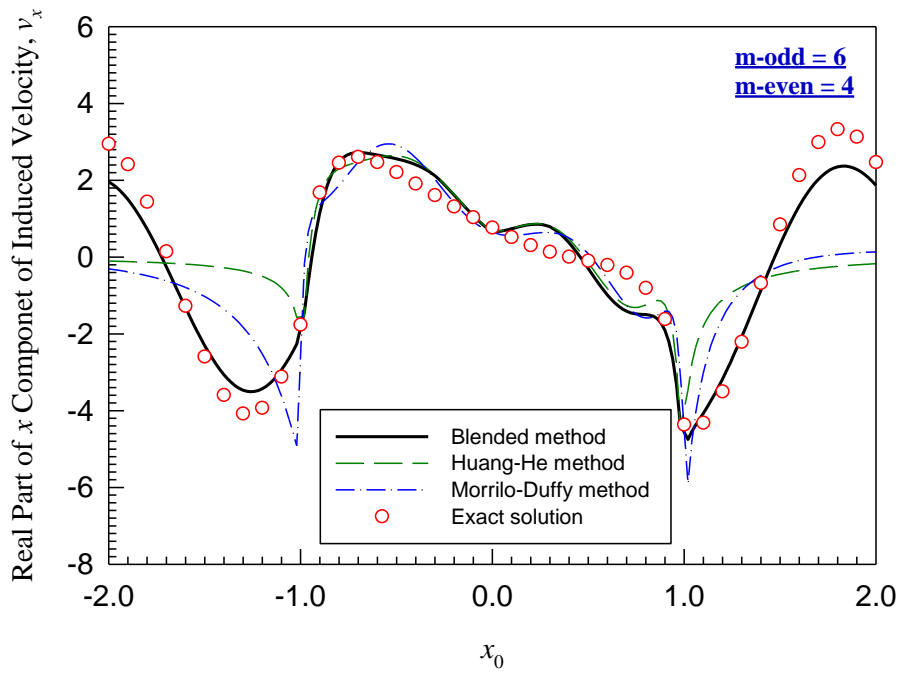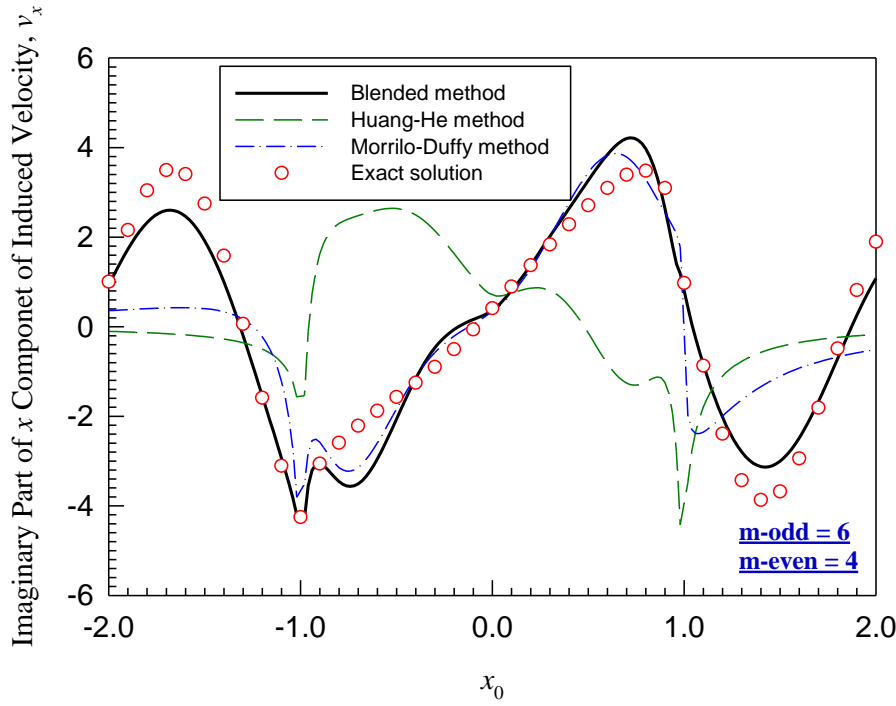
Figure 4.47 x component of induced velocity v_x for y = 0.0, z = 0.4 with τ_2^1 for ω = 4, χ = 85°: (a) real part and (b) imaginary part. (m-odd = 6, m-even = 4)

Chapter 5: Reduced Number of States

For the results in Chapter 4, either 25 states or 74 states are used. A large number of states were employed in order to verify that the present methodology does converge to the exact solution. For many applications of real-time simulation, it is valuable to be able to produce low-fidelity results with many fewer states−but still with sufficient accuracy for valid flight mechanics. Therefore, it is necessary to seek a solution with many fewer states and acceptable accuracy. Many runs have been done in this research that involve varying both the number of even states and the number of odd states in order to find the lower bound of the number of states necessary for a realistic solution for the average and gradients of flow over the disk. This chapter presents the results of that search.

For the test case, the pressure distribution is considered to be elliptical. This is because this is the first-order approximation to disk loading. All of the results have 2 harmonics for the odd terms (enough to give minimal spatial resolution) and 1 harmonic for the even terms (enough to give gradients in the x and y directions). This model has only six states, which is comparable to the Pitt model used in most flight simulators. Results are shown in Figs. 5.1−5.16. Figures 5.1−5.2 give the axial velocity with constant loading ($\omega = 0$), and the induced velocity on the disk ($z = 0.0$) and below the disk ($z = 0.4$) are calculated. The results with dynamic loading with different frequencies ($\omega = 2, 3, 4$) are also investigated in Figs. 5.3−5.8. For the axial velocity with $\omega = 0$, the 6-state solution (m-odd = 2, m-even = 1) both on the disk and below the disk still show great correlation with the exact solution. For the dynamic loading which $\omega = 2$, the 6-state solution still gives good prediction, and it has the same oscillation compared with the exact solution. However, the result start to deteriorate when $\omega > 3$. Figures 5.9−5.16 are the x

component of the induced velocity with 6 states. The same phenomena can be observed that the result with reduced number of states matches the exact solution only if $\omega < 3$.
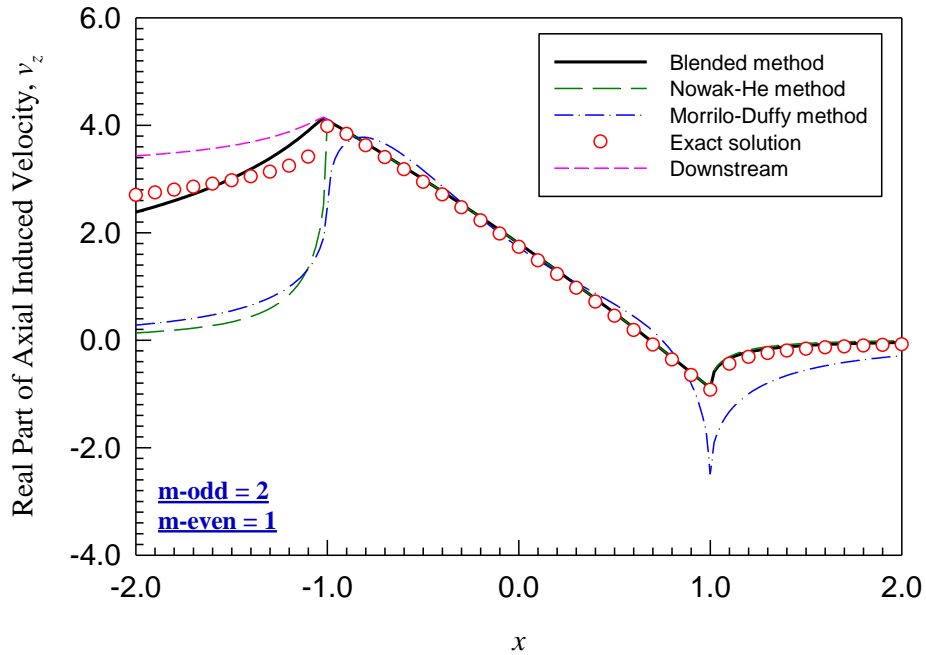
Figure 5.1 Real part of axial velocity v_z for $y = 0.0$, $z = 0.0$ with τ_1^0 for $\omega = 0$, $\chi = 85^o$. (m-odd = 2, m-even = 1)
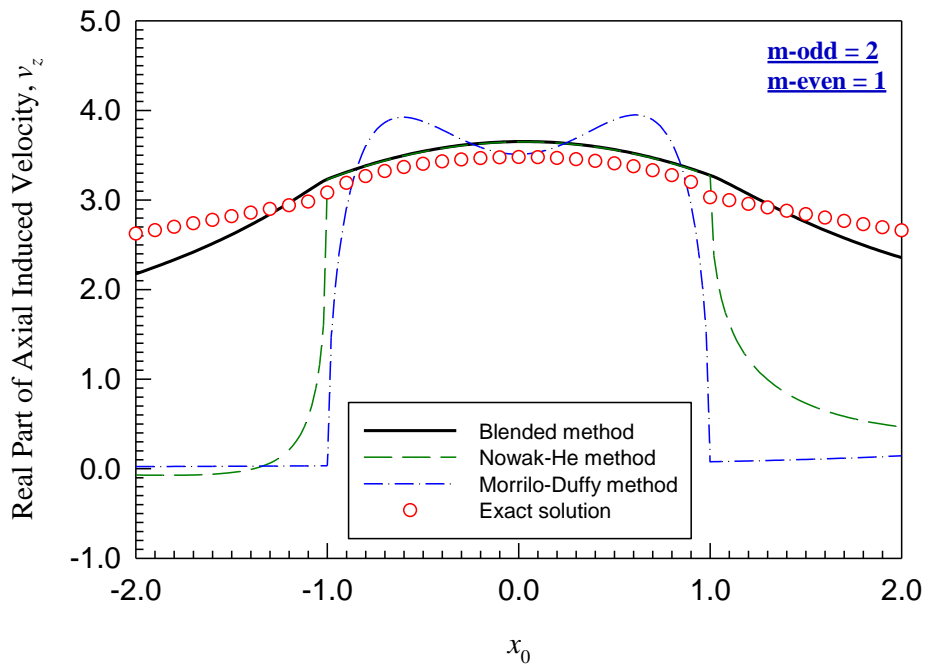

Figure 5.2 Real part of axial velocity v_z for $y = 0.0$, $z = 0.4$ with τ_1^0 for $\omega = 0$, $\chi = 85^o$. (m-odd = 2, m-even = 1)

88
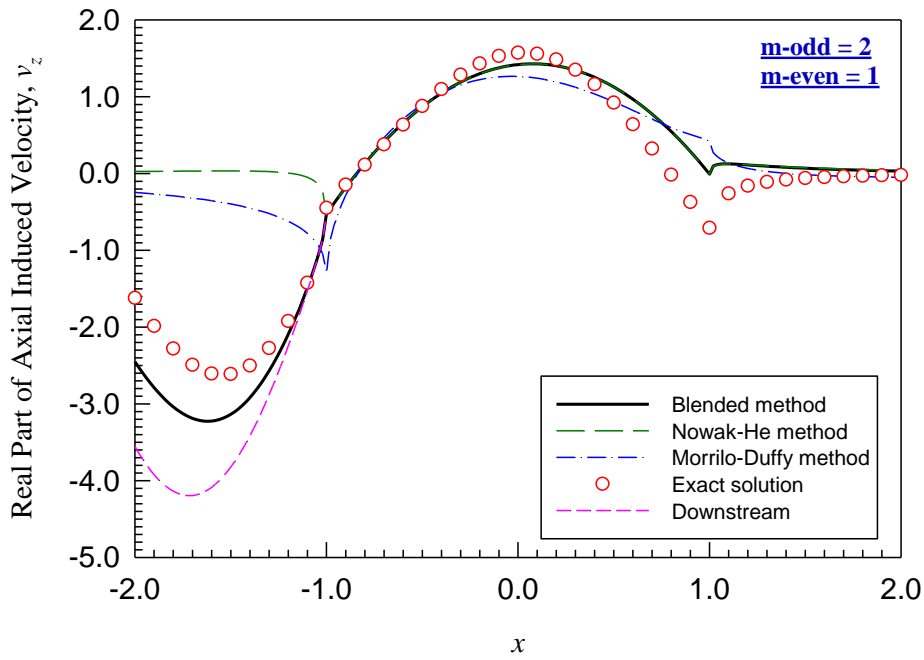
(a)
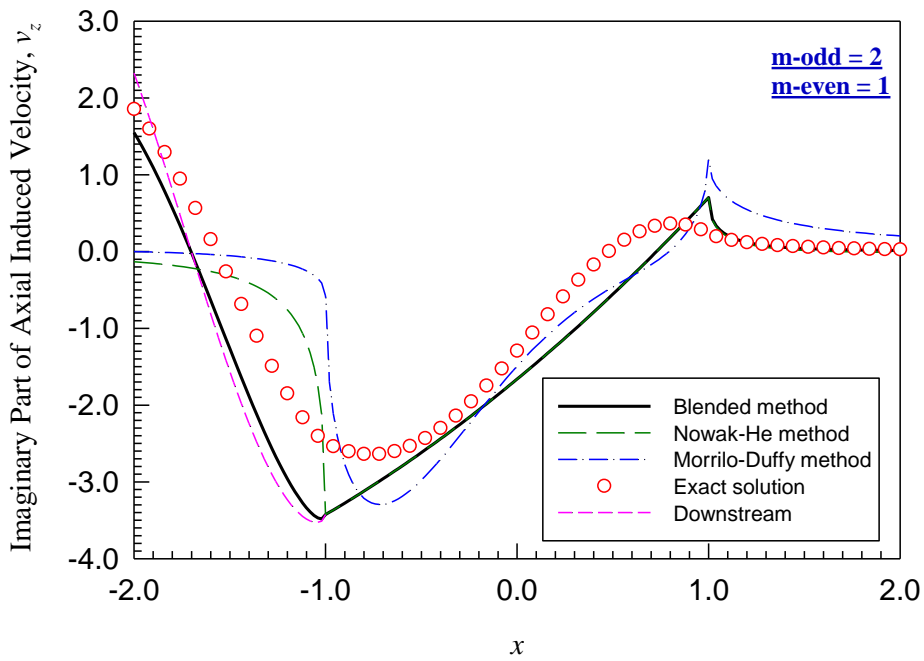
(b)

Figure 5.3 Axial velocity v_z for $y = 0.0$, $z = 0.0$ with τ_1^0 for $\omega = 2.0$, $\chi = 85^o$: (a) real part and (b) imaginary part. (m-odd = 2, m-even = 1)

(a)

(b)

Figure 5.4 Axial velocity v_z for $y = 0.0$, $z = 0.4$ with τ_1^0 for $\omega = 2.0$, $\chi = 85^o$: (a) real part and (b) imaginary part. (m-odd = 2, m-even = 1)

(a)

(b)

Figure 5.5 Axial velocity v_z for $y = 0.0$, $z = 0.0$ with τ_1^0 for $\omega = 3.0$, $\chi = 85^\circ$: (a) real part and (b) imaginary part. (m-odd = 2, m-even = 1)
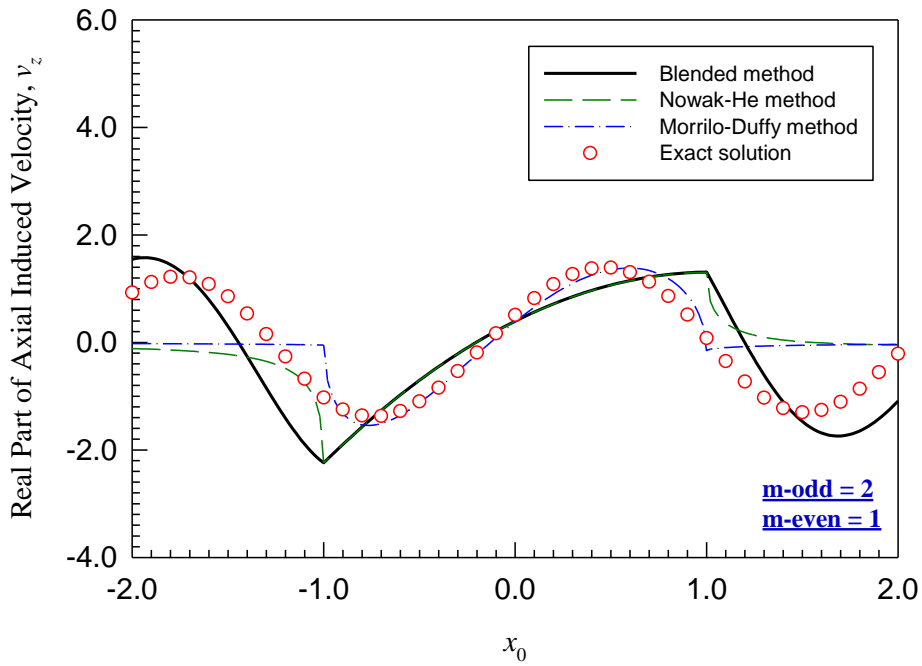
(a)
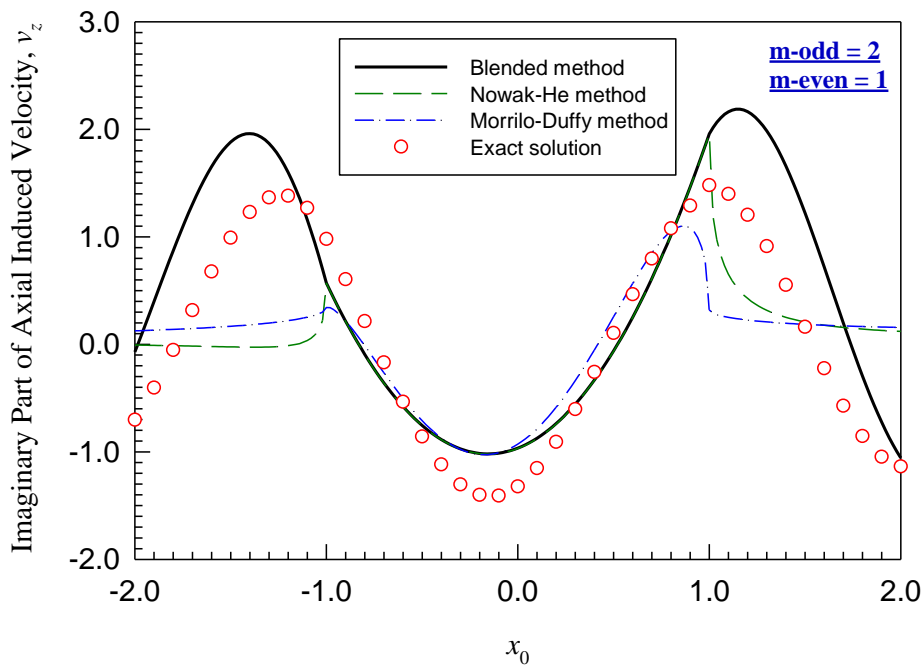
(b)

Figure 5.6 Axial velocity v_z for $y = 0.0$, $z = 0.4$ with τ_1^0 for $\omega = 3.0$, $\chi = 85°$: (a) real part and (b) imaginary part. (m-odd = 2, m-even = 1)
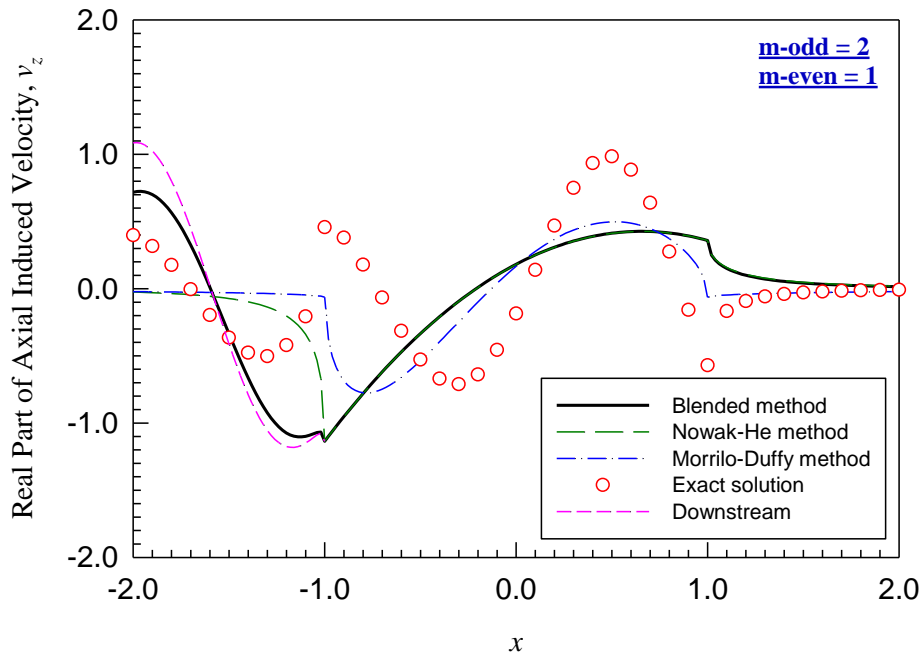
(a)
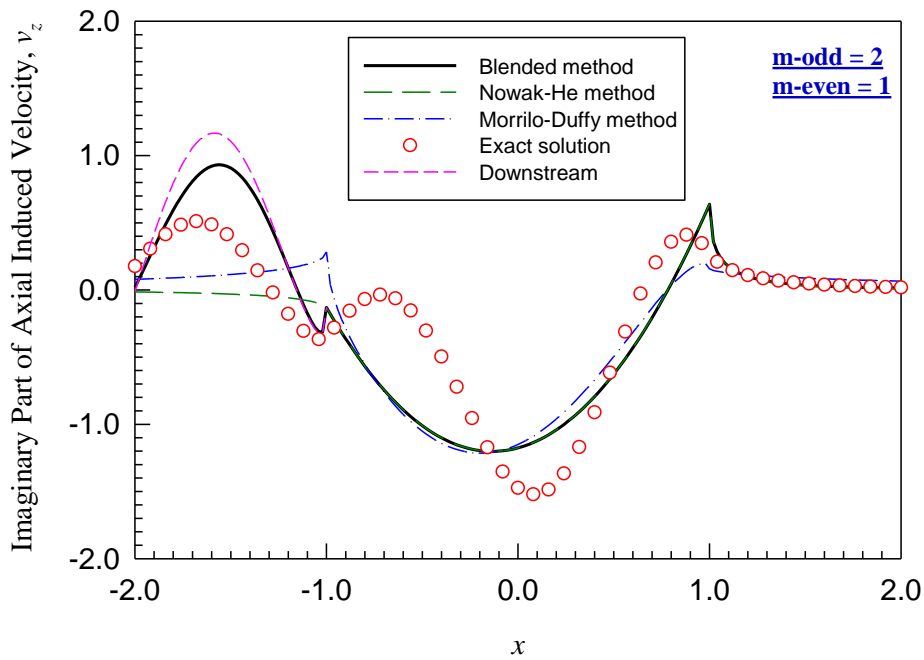
(b)

Figure 5.7 Axial velocity v_z for $y = 0.0$, $z = 0.0$ with τ_1^0 for $\omega = 4$, $\chi = 85^\circ$: (a) real part and (b) imaginary part. (m-odd = 2, m-even = 1)
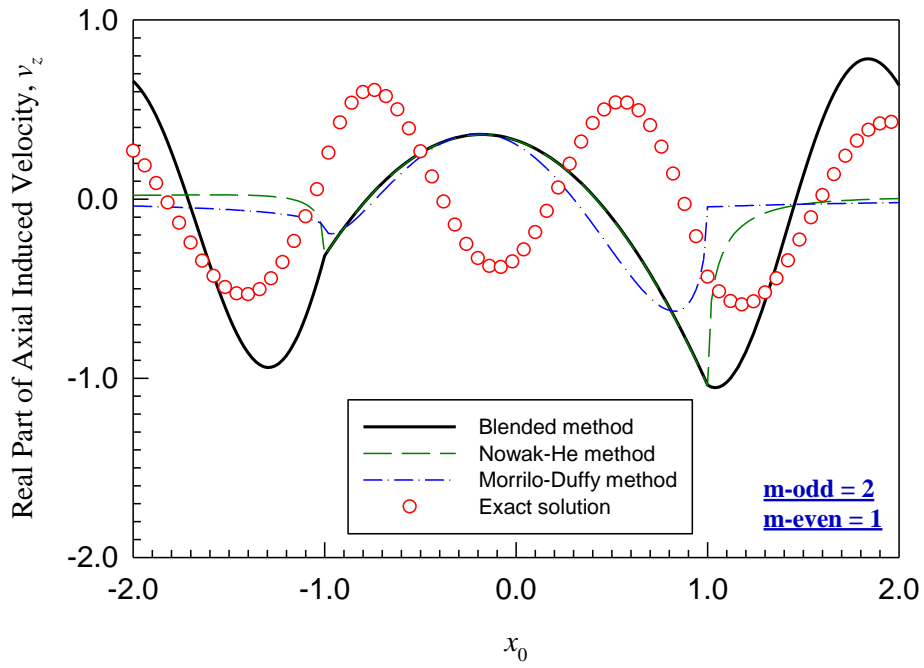
(a)
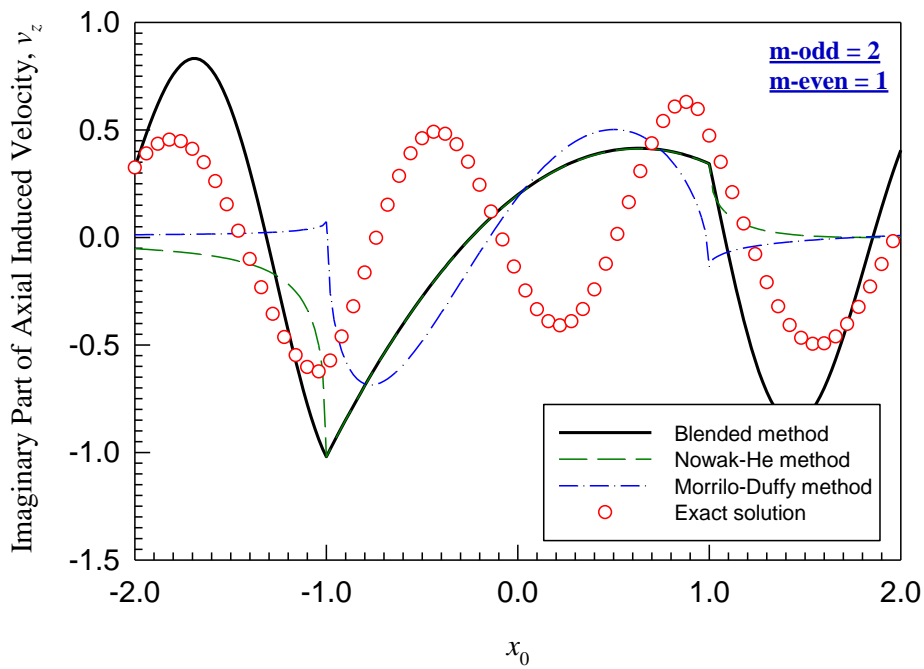
(b)

Figure 5.8 Axial velocity v_z for $y = 0.0$, $z = 0.4$ with τ_1^0 for $\omega = 4$, $\chi = 85^\circ$: (a) real part and (b) imaginary part. (m-odd = 2, m-even = 1)
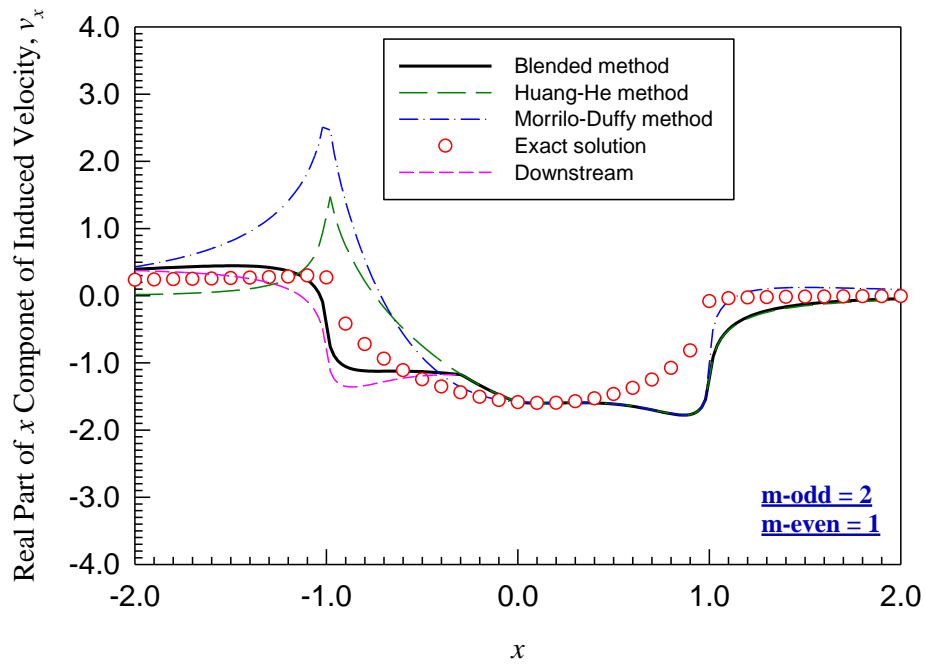
Figure 5.9 Real part of x component of induced velocity v_x for $y = 0.0$, $z = 0.0$ with τ_1^0 for $\omega = 0$, $\chi = 85°$. (m-odd = 2, m-even = 1)
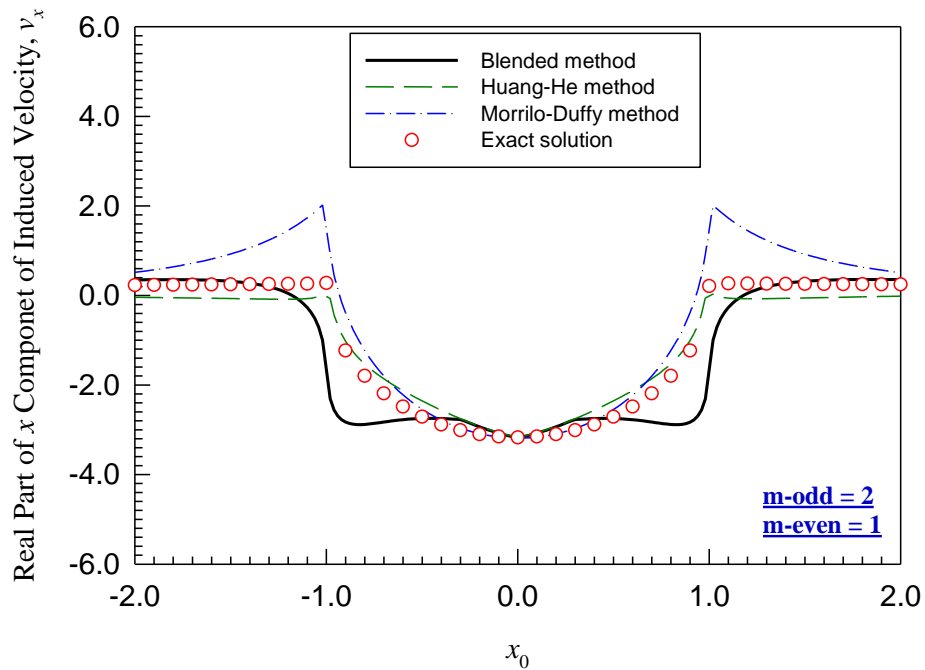
Figure 5.10 Real part of x component of induced velocity v_x for $y = 0.0$, $z = 0.4$ with τ_1^0 for $\omega = 0$, $\chi = 85°$. (m-odd = 2, m-even = 1)
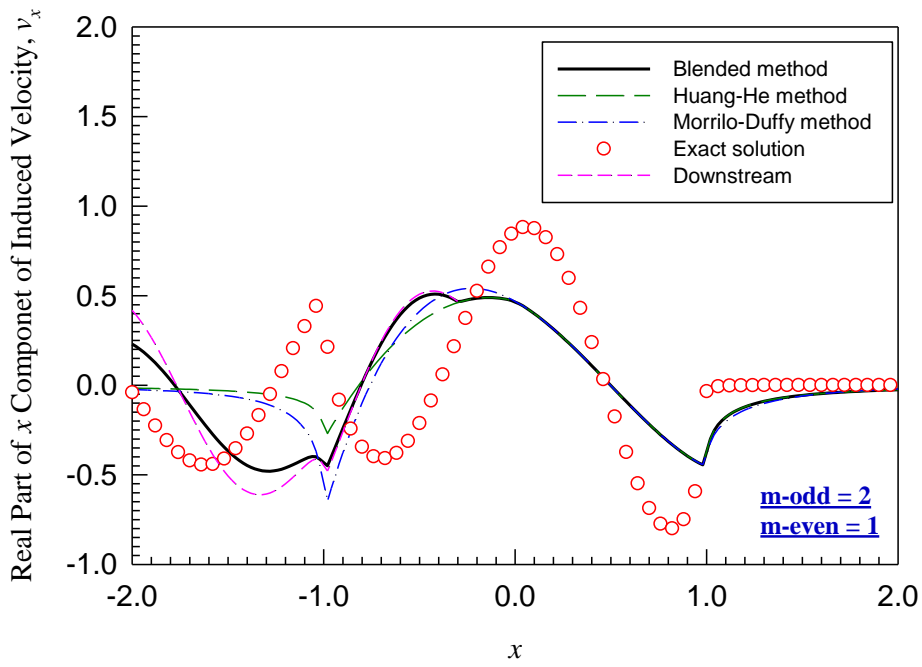
(a)
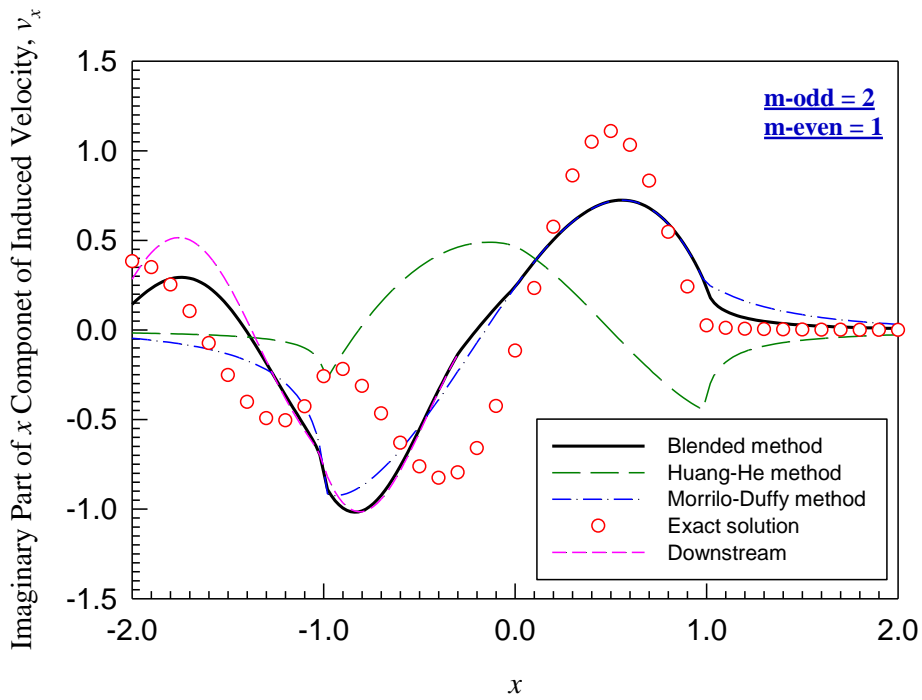
(b)

Figure 5.11 x component of induced velocity v_x for $y = 0.0$, $z = 0.0$ with τ_1^0 for $\omega = 4$, $\chi = 85^\circ$: (a) real part and (b) imaginary part. (m-odd = 2, m-even = 1)
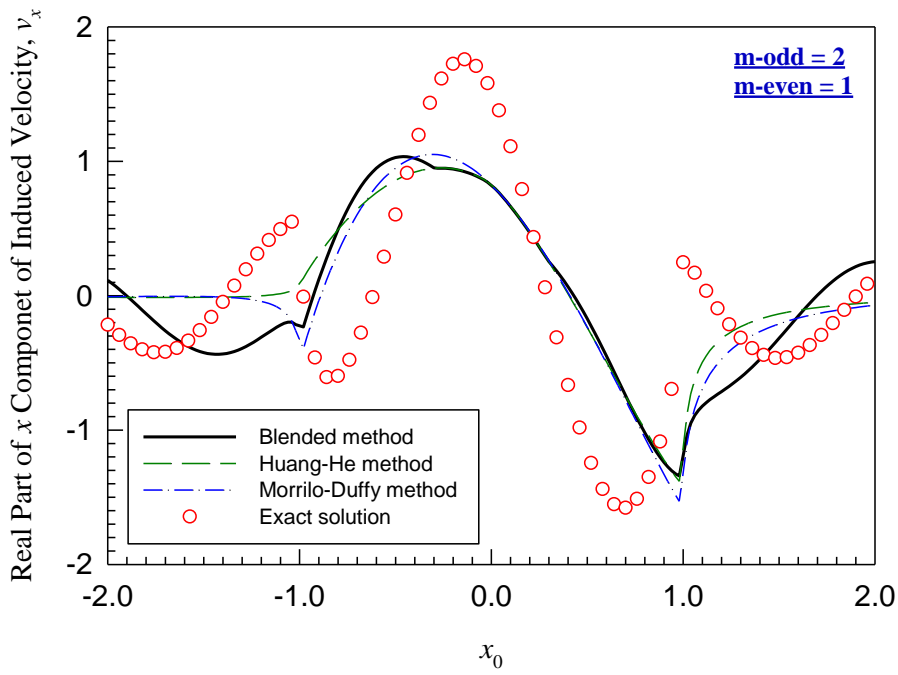
(a)
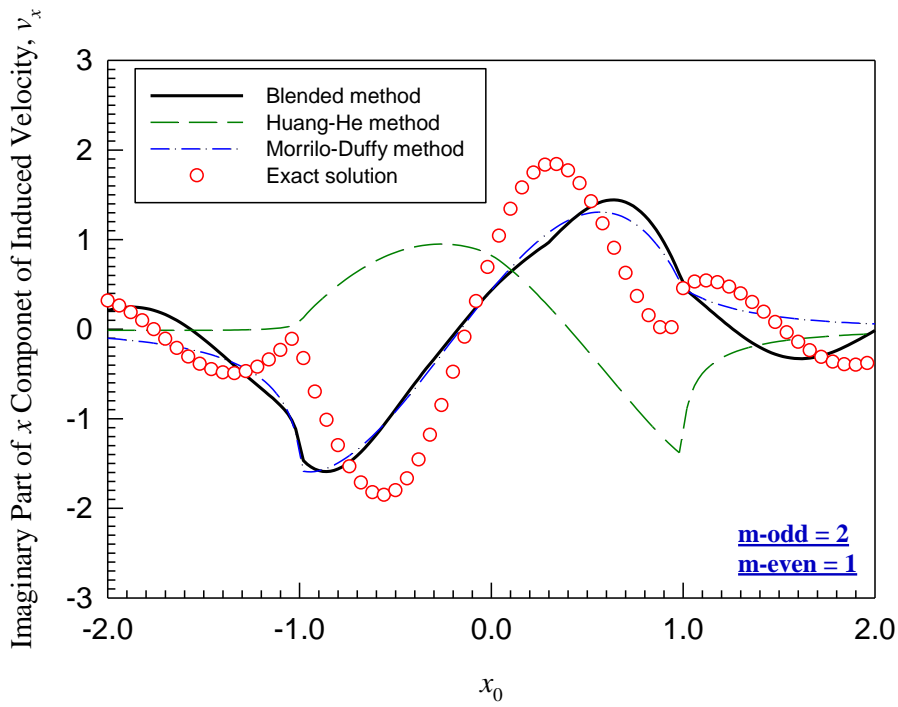
(b)

Figure 5.12 x component of induced velocity v_x for $y = 0.0$, $z = 0.4$ with τ_1^0 for $\omega = 4$, $\chi = 85°$: (a) real part and (b) imaginary part. (m-odd = 2, m-even = 1)
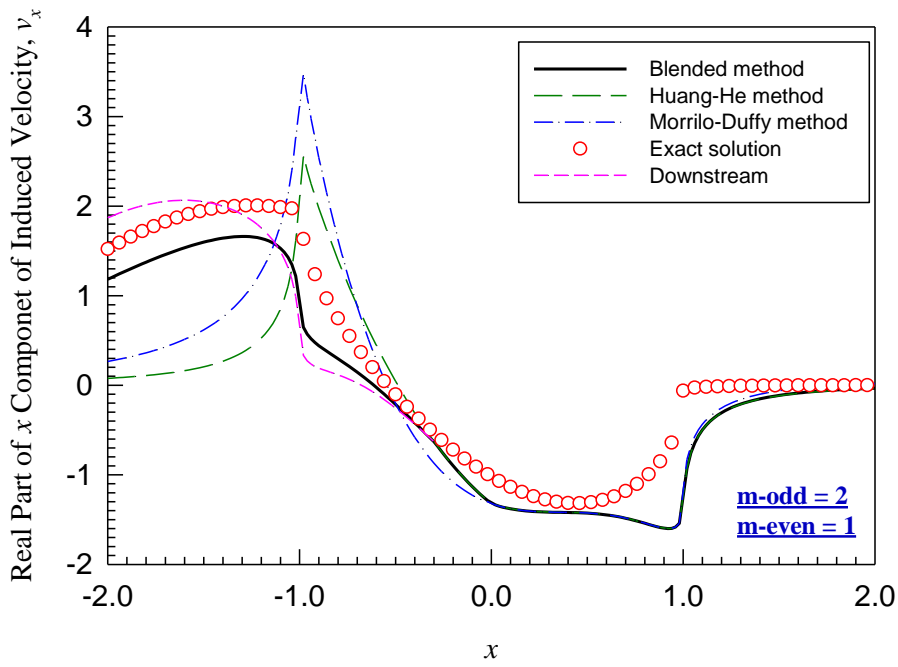
(a)
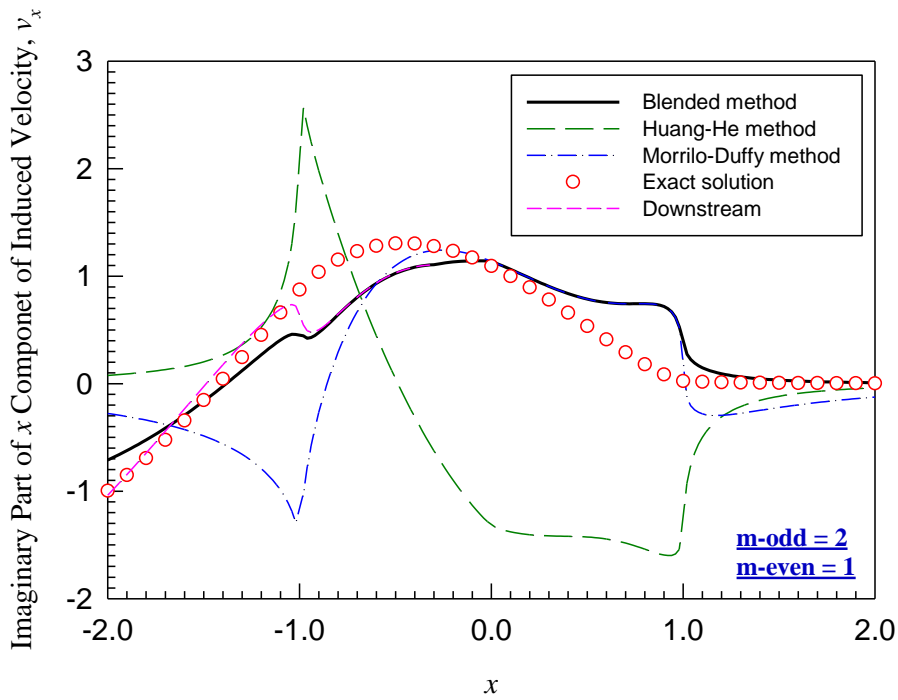
(b)

Figure 5.13 Real part of x component of induced velocity v_x for $y = 0.0$, $z = 0.0$ with τ_1^0 for $\omega = 2.0$, $\chi = 85^{\rm o}$: (a) real part and (b) imaginary part. (m-odd = 2, m-even = 1)

(a)

(b)

Figure 5.14 Real part of x component of induced velocity v_x for $y = 0.0$, $z = 0.4$ with τ_1^0 for $\omega = 2.0$, $\chi = 85^\circ$: (a) real part and (b) imaginary part. (m-odd = 2, m-even = 1)
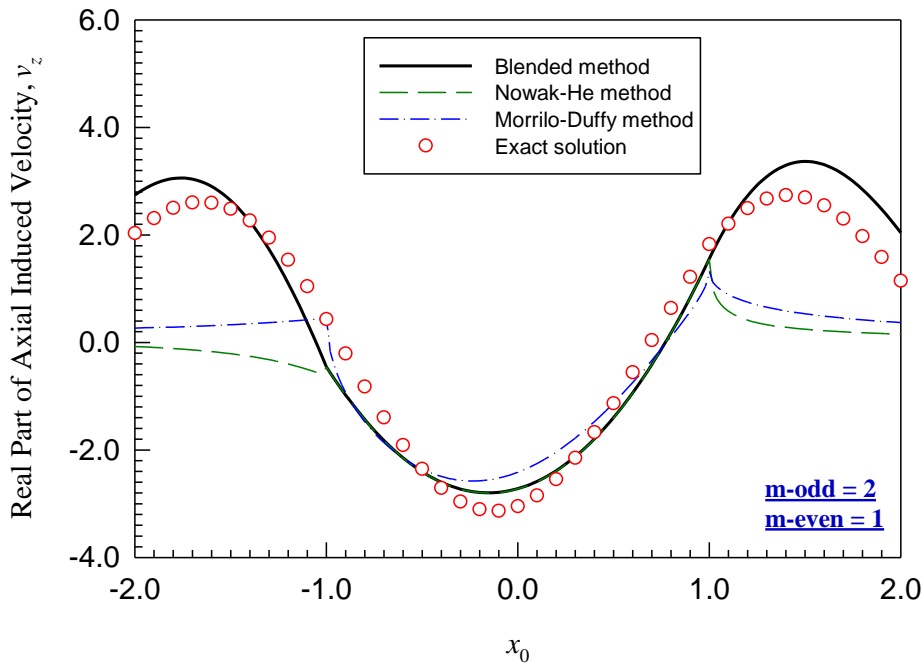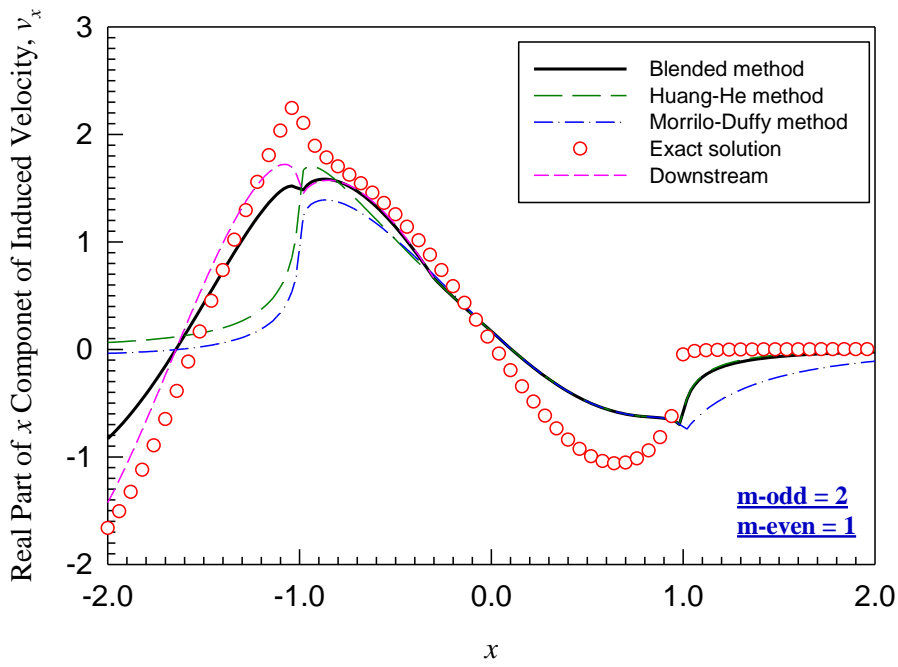
(a)
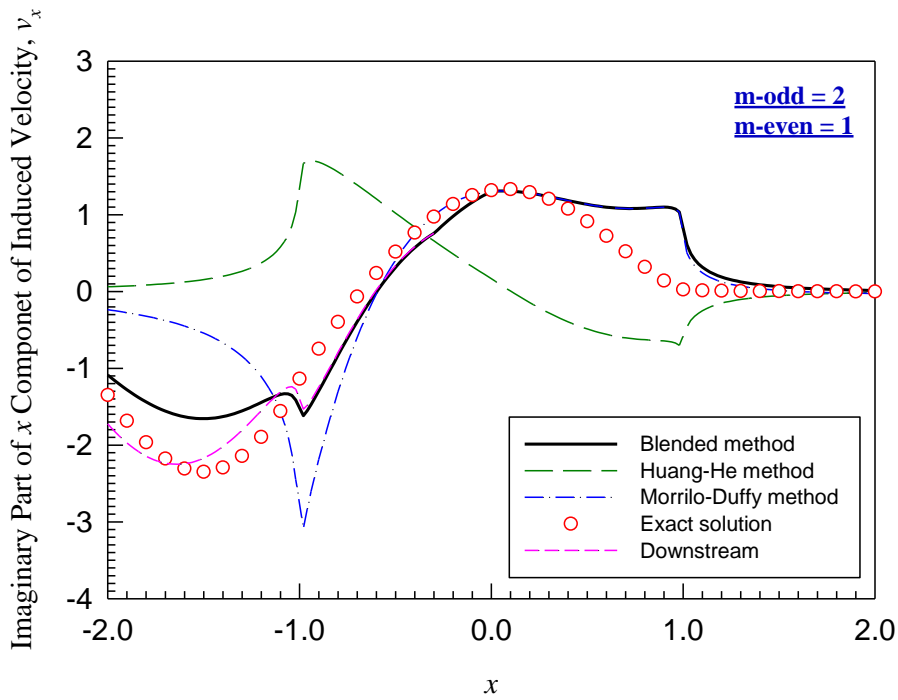
(b)

Figure 5.15 Real part of x component of induced velocity v_x for $y = 0.0$, $z = 0.0$ with τ_1^0 for $\omega = 3.0$, $\chi = 85^\circ$: (a) real part and (b) imaginary part. (m-odd = 2, m-even = 1)
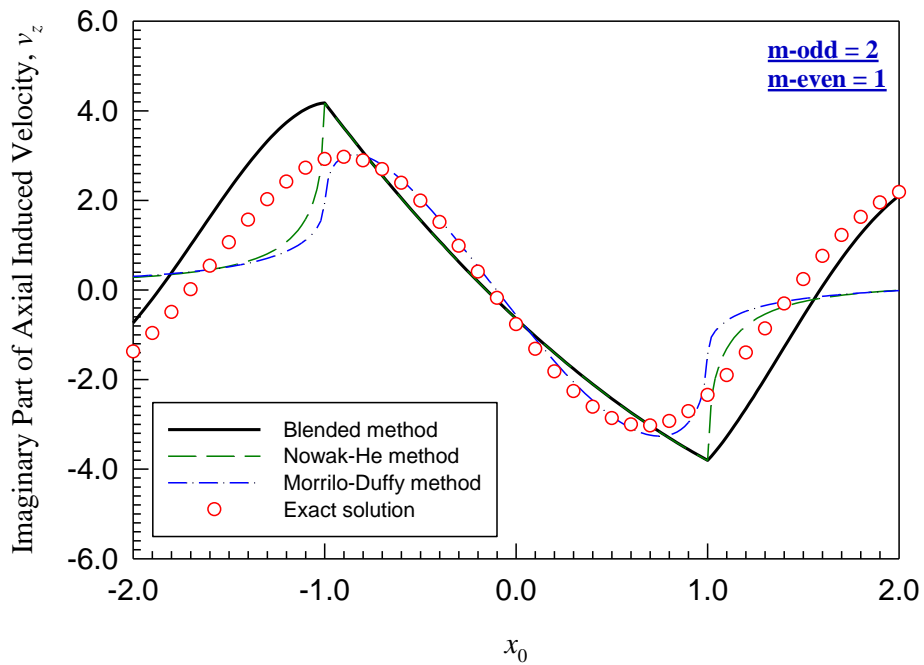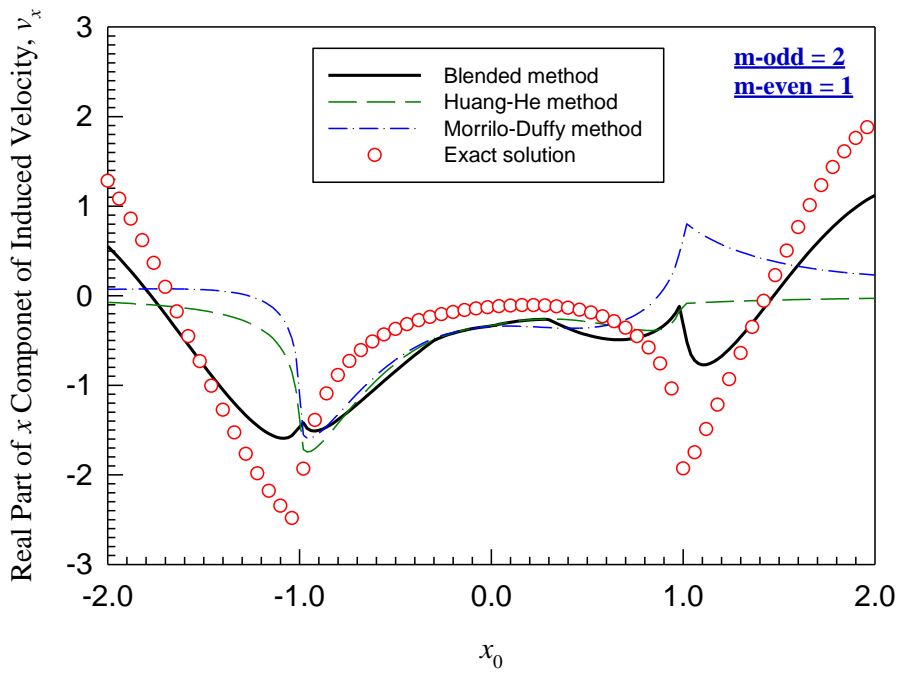
(a)
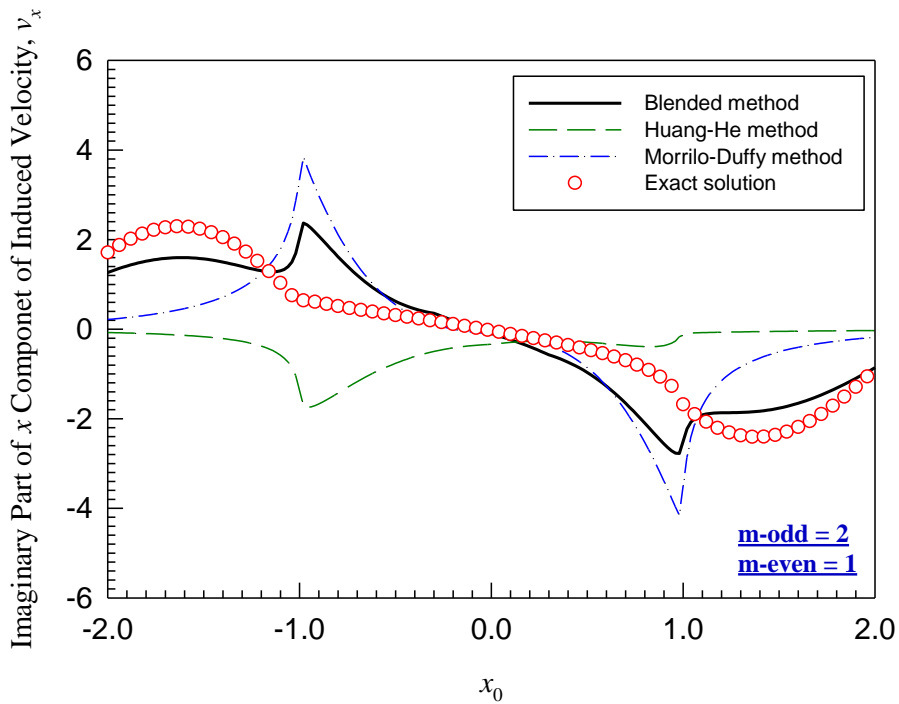
(b)

Figure 5.16 Real part of x component of induced velocity v_x for $y = 0.0$, $z = 0.4$ with τ_1^0 for $\omega = 3.0$, $\chi = 85^\circ$: (a) real part and (b) imaginary part. (m-odd = 2, m-even = 1)
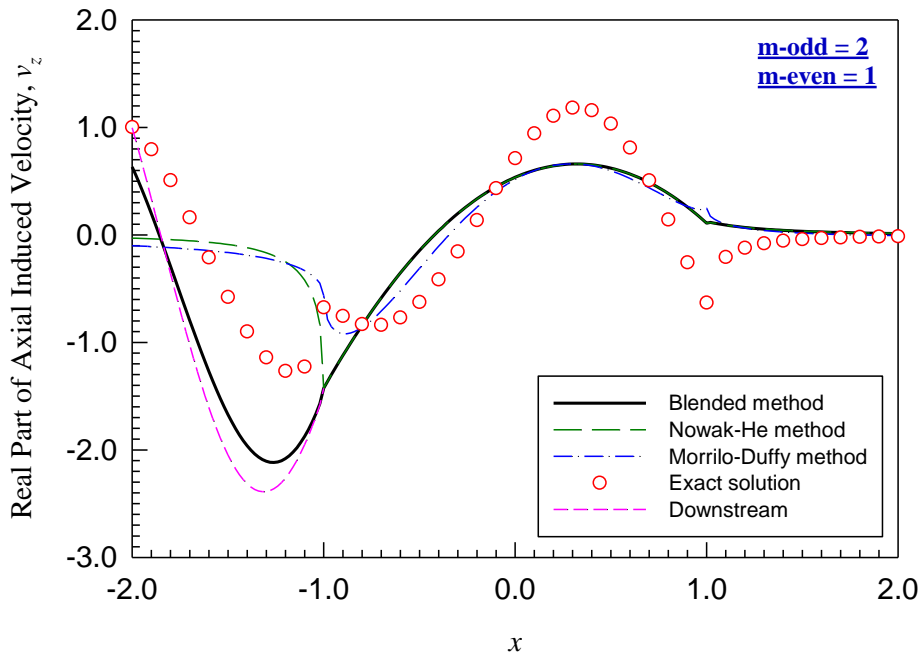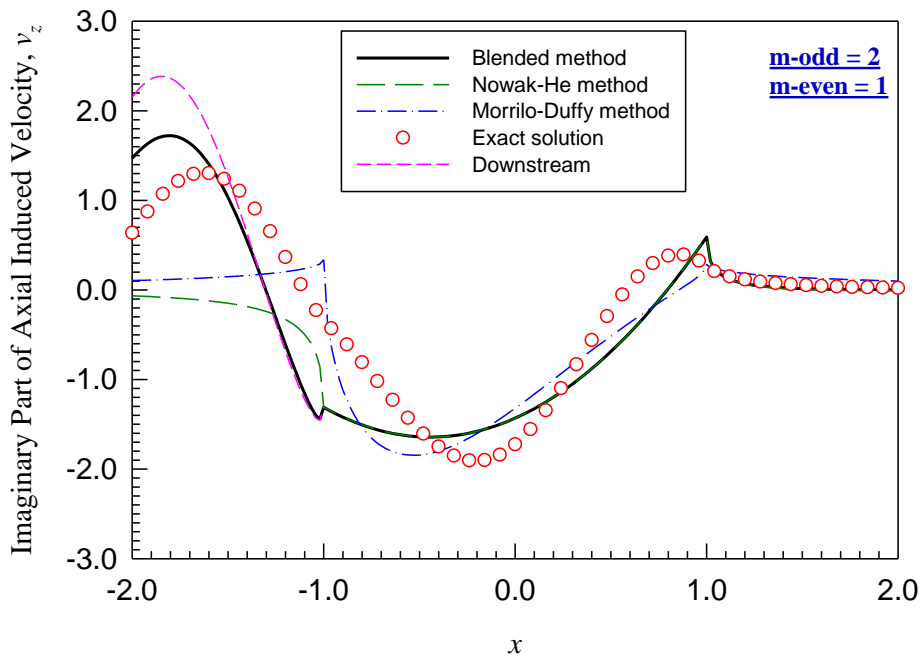
101

It has been seen the 6-state model can give reasonable results both on and off the disk for all components of induced velocity when the reduced frequency is less than 3.0. This frequency range is typical of the frequency range of flight mechanics and controls simulations. Existing flight simulations that use the Pitt model have only 6 states, but they only compute the normal component of flow on the disk. It implies that these simulations could upgrade to this new model with very little increase in computational costs over the present models. With the upgrade, they could compute all three components of flow both on and off the disk. The consequence of this is that the present model is very practical for use in helicopter flight simulation programs. The model is ready to use in its present form for such applications with only a few states.

Chapter 6: Nonlinear Extensions

For the models which are discussed in the previous chapters, the flows are linearized about the free-stream velocity V_∞. Such linear model is quite good in the cruise condition. However, there are certain nonlinear terms that are also important for helicopters in low speed flight or hover. The nonlinearities that we discussed here are: 1.) mass flow nonlinearity, 2.) wake skew nonlinearity, 3.) wake contraction, and 4.) wake curvature.

6.1 Mass Flow Nonlinearity

For a helicopter in hover, V_∞ goes to zero; and the induced velocity computed from those equations will become infinity when the time increase. The reason for this singularity is that the mass flow parameter in the linearized model is based purely on the free-stream velocity. According to momentum theory, the mass flow must also include the induced flow through the rotor. This can be accomplished by attention to momentum theory to give the correct mass flow parameter. When this is done, then the finite-state model in steady, axial flow will agree exactly with classical momentum theory. To make the theory compatible with nonlinear momentum theory, it is necessary to replace the V_∞ term with the total average flow at the rotor.

$$V_T = \sqrt{V_\infty^2 \sin^2 \chi + (V_\infty \cos \chi + \bar{v}_z)^2} \tag{6.1}$$

The mass-flow parameter is defined by the perturbation quantity:

$$\begin{aligned} V &= \frac{d}{d\bar{v}_z}\left(\bar{v}_z V_T\right) \\ &= \frac{V_\infty^2 \sin^2 \chi + (V_\infty \cos \chi + \bar{v}_z)(V_\infty \cos \chi + 2\bar{v}_z)}{V_T} \end{aligned} \tag{6.2}$$

Then Eq. (3.33) with Nowak-He variables can be modified by inserting the $[V]$ matrix on the left-hand side of the equations.

$$\left[M^c\right]_{new}\left\{\overset{*}{\alpha}_n^m\right\}+\left[D^c\right][V]\left[L^c\right]^{-1}\left[M^c\right]_{new}\left\{\alpha_n^m\right\}=\left[D^c\right]\left\{\tau_n^m\right\}\qquad(6.3)$$

where $[V]$ is a diagonized matrix,

$$[V]=\begin{bmatrix}V_T & & & & \\ & V & & & \\ & & V & & \\ & & & V & \\ & & & & \ldots\end{bmatrix}\qquad(6.4)$$

and

$$[M]_{new}=\begin{bmatrix}I & M_{oe} \\ M_{eo}A^{-1} & M_{ee}\end{bmatrix}\qquad(6.5)$$

$$\bar{v}_z=\sqrt{3}\begin{Bmatrix}1\\0\\0\\0\\\ldots\end{Bmatrix}\left[L^c\right]^{-1}\left[M\right]_{new}\{\alpha\}\qquad(6.6)$$

Equations (6.3) to (6.6) give a nonlinear version of the model that reduces to momentum theory in hover.

6.2 Wake Skew Nonlinearity

The $[L]$ matrix in Eq. (6.3) depends on the wake skew angle. As with the mass flow parameter, the wake skew angle must also take into account the effect of the induced flow at the

rotor disk on the equivalent wake skew angle. This introduces another set of nonlinearities into the model, since the [L] matrix will then depend on the states through the wake skew parameter $X = \tan(\chi/2)$. Based on the thesis by He [18], the effective skew angle and skew angle parameter are:

$$\chi_{\text{eff}} = \arctan\left[(V_\infty \sin\chi)/(V_\infty \cos\chi + \overline{v_z})\right] \tag{6.7}$$

$$X = \arctan(\chi_{\text{eff}}/2) = V_\infty \sin\chi / \left(V_T + |V_\infty \cos\chi + \overline{v_z}|\right) \tag{6.8}$$

Equations (6.7) and (6.8) give the effective nonlinearity on the wake skew parameter that is to go into the [L] matrix.

6.3 Effect of Wake Contraction

Based on the continuity equation, the rotor wake will contract downstream as the pressure in the wake expands to atmospheric pressure and the induced flow increases. The amount of the induced flow increases for the nonlinear model—shown in Eq. (6.3)—is determined from the Adjoint theorem for the downstream velocity. What remains, then, is to write a mapping from the linear velocity space of the original model, to a warped space that will produce the wake contraction necessary to ensure continuity. The velocity field for the non-deformed geometry is shown in Eq. (6.8), and the geometric basis for this contraction mapping is illustrated in Fig. 6.1.

$$\overline{v_1} = \overline{v_z}(z=a) = \frac{1}{\pi}\sum_{\psi=0}^{2\pi}\sum_{r=0}^{1} v_z(z=a)r\,dr\,d\psi \tag{6.8}$$

The average velocity within the circular cross-section of the wake at the plane of $z = a$ is expressed in Eq. (6.7).
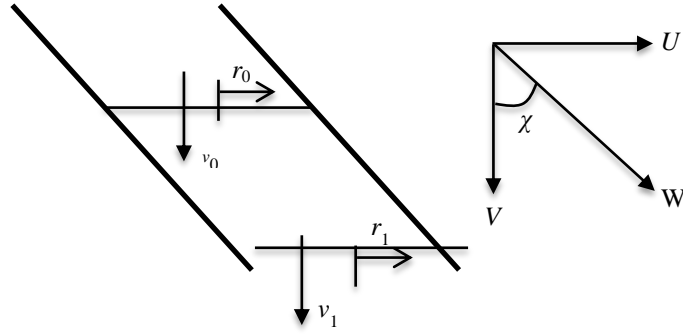
Figure 6.1 Contraction mapping.

From the continuity equation, one obtains

$$\left(\pi R_0^2 \cos \chi_0\right)W_0 = \left(\pi R_1^2 \cos \chi_1\right)W_1 \tag{6.9}$$

where

$$\cos \chi_0 = \frac{V_\infty + \overline{v}_0}{W_0}$$

$$\cos \chi_1 = \frac{V_\infty + \overline{v}_1}{W_1} \tag{6.10}$$

Then the radius of the rotor wake downstream can be found in (6.11).

$$R_1 = R_0 \sqrt{\frac{V_\infty + \overline{v}_0}{V_\infty + \overline{v}_1}} \tag{6.11}$$

The contraction factor at that plane is defined as

$$K \equiv \sqrt{\frac{V_\infty + \overline{v}_0}{V_\infty + \overline{v}_1}} \tag{6.12}$$

For the hover case, $V_\infty = 0$, Eq. (6.12) will be reduced to Eq. (6.13).

106

$$K = \sqrt{\frac{\overline{v_0}}{\overline{v_1}}} \qquad (6.13)$$

When the contraction factor (K) is introduced, it gives

$$\begin{cases} \dfrac{r_1}{r_0} = K, \text{ for } |r_0| \le 1; \\[4mm] \dfrac{r_1}{r_0} = \dfrac{K + |r_0| - 1}{|r_0|}, \text{ for } |r_0| > 1. \end{cases} \qquad (6.14)$$

For the nonlinear model with wake contraction, the Nowak-He variables are used; and only the constant loading case is illustrated. The results have 4 harmonics for the odd terms and no harmonic for the even terms. The z coordinate is the axial axis of the rotor disk and $z > 0$ for below the disk. The average velocities on the rotor disk, below and above the rotor disk for different free stream velocities are tabulated in Table 6.1. The contraction factor can also be computed using Eq. (6.12). As it is shown in Table 6.1, the contraction ratio will approach unity when the free-stream velocity becomes large compared to the induced flow. The wake will be contracted below the disk, while it will be expanded above the disk. For the free-stream velocity equals zero, the wake curvature is the largest, and the rotor wake becomes rigid when it gets bigger. For $V_\infty = 0.0$, the real part of axial velocity for $y = 0.0$, with τ_1^0 for $\omega = 0$ and $\chi = 0°$ at z = 0, 0.4 and -0.4 is shown in Figs. 6.2−6.4, respectively. The result with wake contraction is represented by the black solid line, and the velocity without wake contraction is denoted by the green dashed curve. They are plotted in the same graph for comparison. For the velocity on the disk ($z = 0$), the two curves are identical. To better illustrate the rotor wake shape at the different free stream velocities, the wake contraction streamlines for $V_\infty = 0.0$, 0.1 and 0.4 are demonstrated in Figs. 6.5−6.7, respectively. The same parameters are used in those figures. For

107

$V_\infty = 0.4$, the wake contraction streamlines are almost flat, and little wake contraction phenomenon can be observed.

Table 6.1 Average induced velocity and the contraction factor

$(y = 0.0, -1 < x < 1$ with τ_1^0 for $\omega = 0$, $\chi = 0^o$, (m-odd = 4, even = 0))

z		V_∞				
		0.0	0.1	0.2	0.3	0.4
0	$\overline{v}_0$	0.0581	0.0286	0.0172	0.012	0.0092
0.4	$\overline{v}_1$	0.0863	0.0425	0.0256	0.0179	0.0137
	K	0.8205	0.9500	0.9812	0.9907	0.9945
1.0	$\overline{v}_1$	0.1020	0.0502	0.0302	0.0212	0.0162
	K	0.7547	0.9253	0.9714	0.9856	0.9916
-0.2	$\overline{v}_1$	0.0403	0.0198	0.0119	0.0083	0.0064
	K	1.2007	1.0361	1.0124	1.0060	1.0034
-0.4	$\overline{v}_1$	0.0299	0.0147	0.0089	0.0062	0.0047
	K	1.3940	1.0589	1.0197	1.0094	1.0055
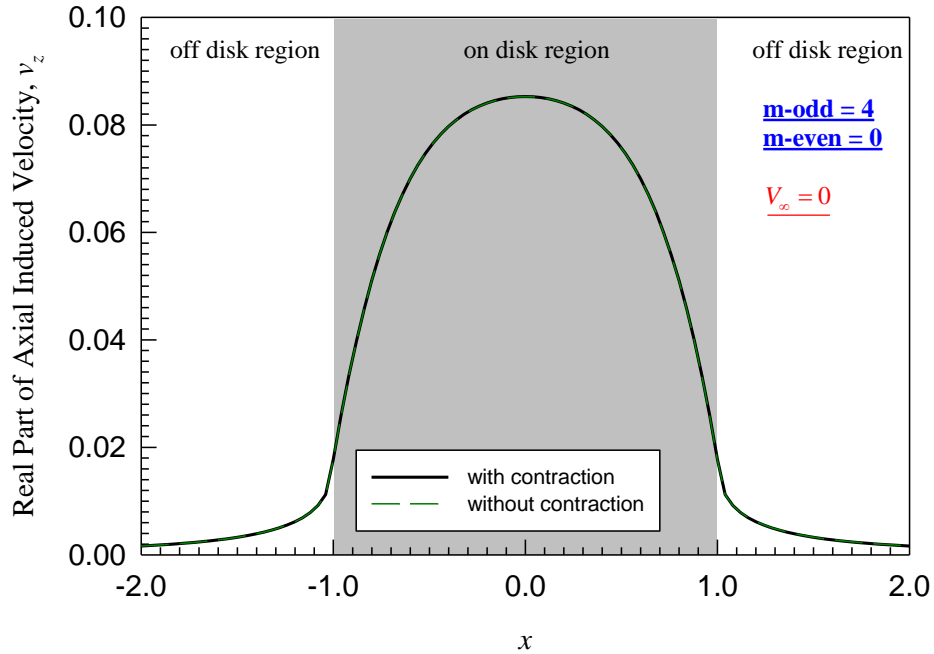
Figure 6.2 Real part of axial velocity V_z for y = 0.0, $z = 0.0$ with τ_1^0 for $\omega = 0$, $\chi = 0^o$, $V_\infty = 0$. (m-odd = 4, m-even = 0)
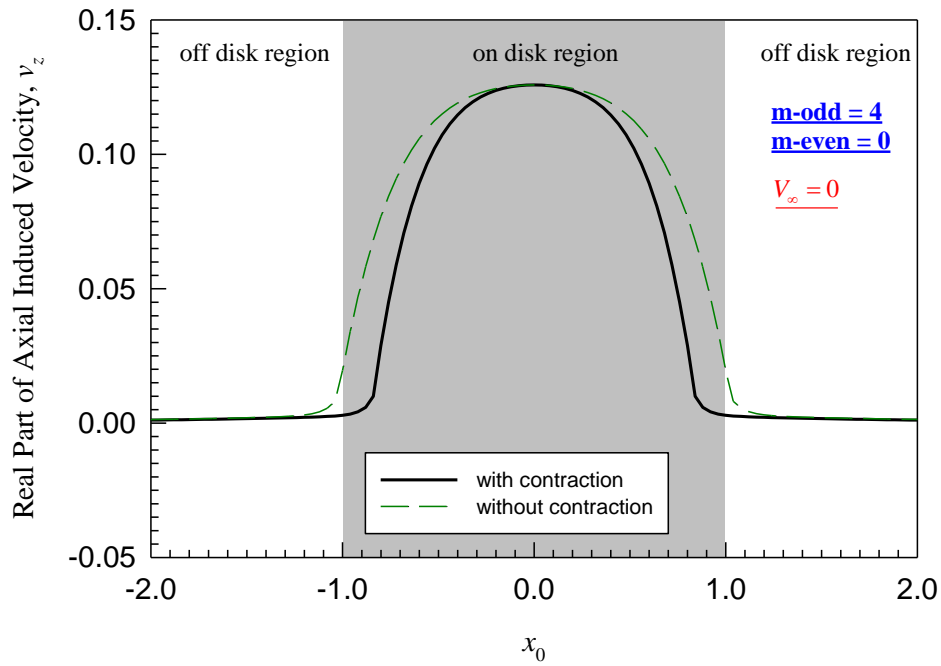
Figure 6.3 Real part of axial velocity v_z for y = 0.0, z = 0.4 with τ_1^0 for $\omega = 0$, $\chi = 0^o$, $V_\infty = 0$. (m-odd = 4, m-even = 0)
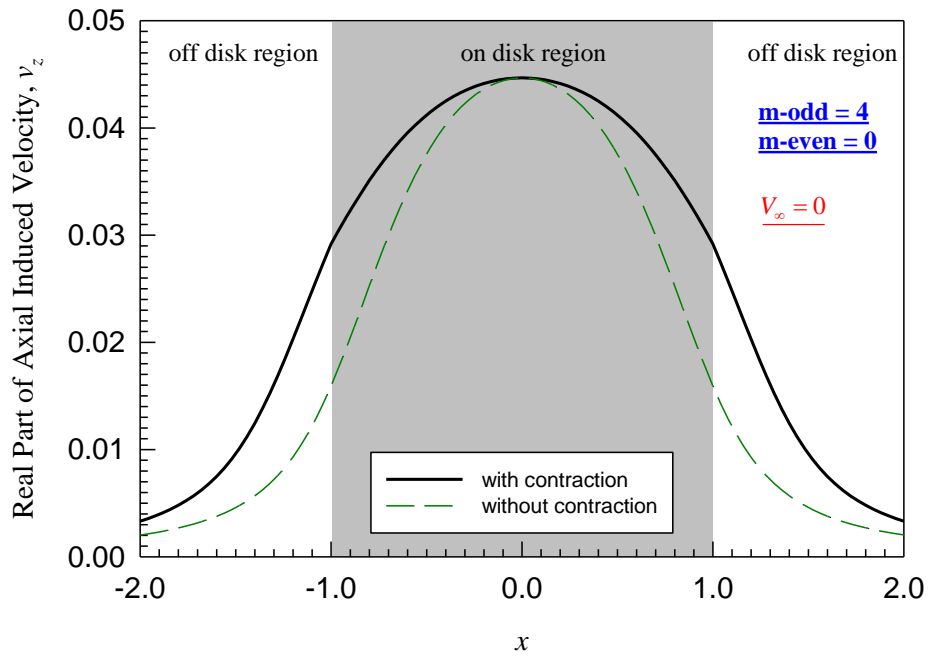
Figure 6.4 Real part of axial velocity v_z for y = 0.0, z = -0.4 with τ_1^0 for $\omega = 0$, $\chi = 0^o$, $V_\infty = 0$. (m-odd = 4, m-even = 0)
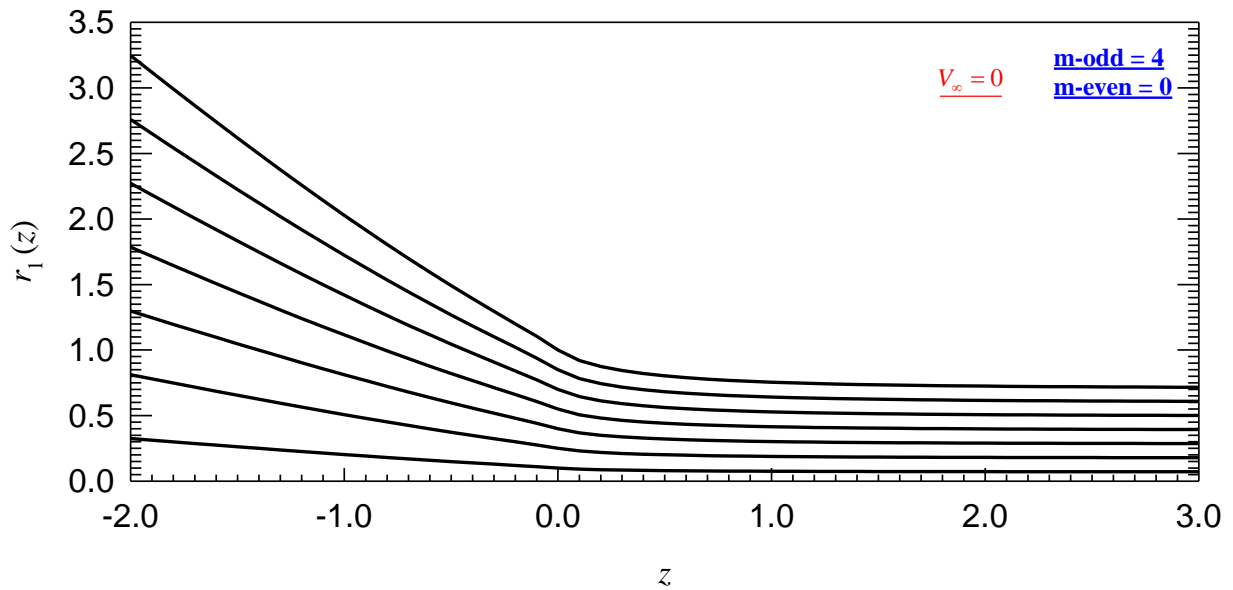
Figure 6.5 Wake contraction streamlines with τ_1^0 for $\omega = 0$, $\chi = 0^o$, $V_\infty = 0$. (m-odd = 4, m-even = 0)
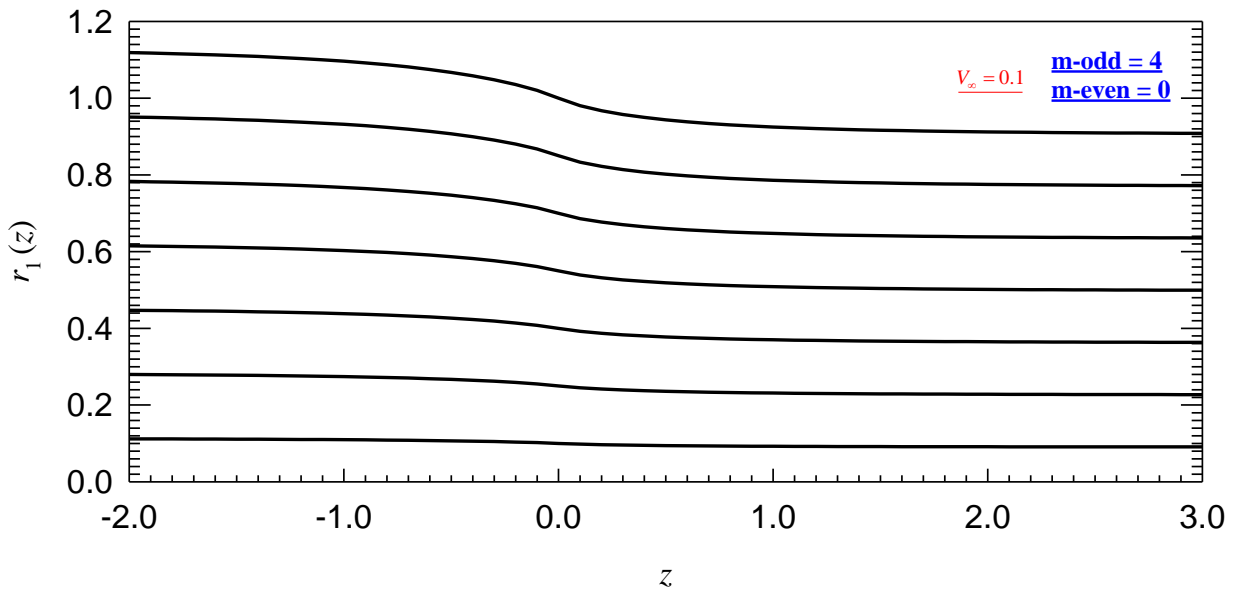
Figure 6.6 Wake contraction streamlines with τ_1^0 for $\omega = 0$, $\chi = 0^o$, $V_\infty = 0.1$. (m-odd = 4, m-even = 0)
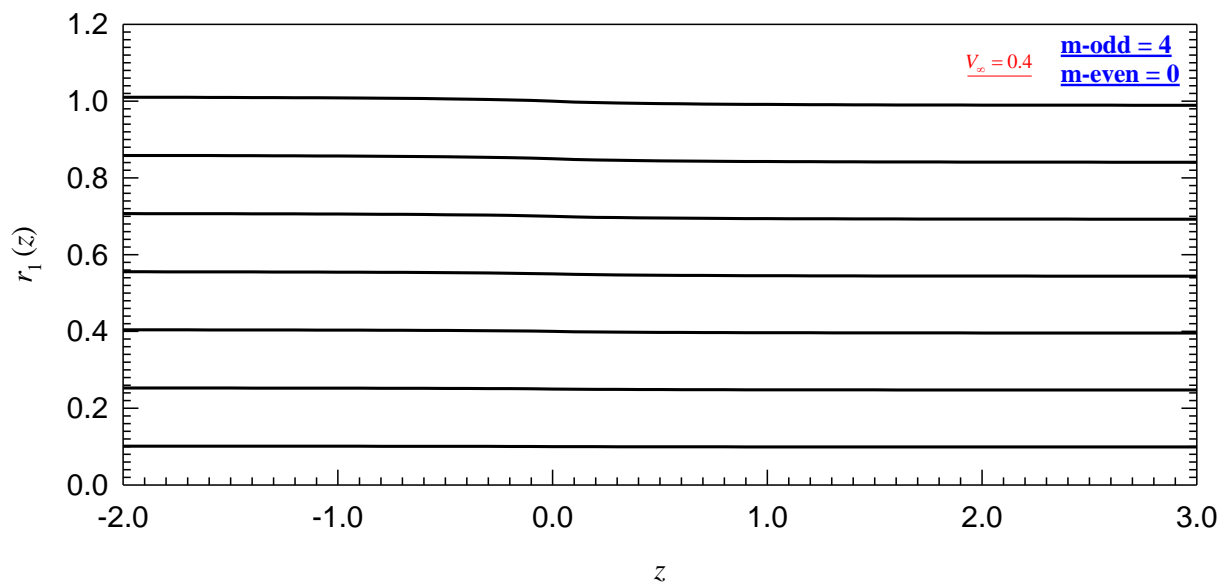
Figure 6.7 Wake contraction streamlines with τ_1^0 for $\omega = 0$, $\chi = 0°$, $V_\infty = 0.4$. (m-odd = 4, m-even = 0)

6.4 Nonlinearity due to Wake Curvature

An important development in the history of dynamic inflow was the realization that wake curvature (during, for example, a pull-up maneuver) has a profound effect on the induced flow field which, in turns, changes the handling qualities. This effect could be introduced into the Pitt-Peters model through a simple, curved momentum tube analysis or a curved vortex-tube analysis [19]. This resulted in extra terms in the [L] matrix that were functions of wake curvature κ and X. Thus, the theory is for small curvature.

This effect could also be incorporated into the He model through appropriate integrals [20]. These also involved κ and products of κ and X. Thus, the wake curvature effects are nonlinear. In Fig. 6.8, the wake distortion parameters for wake contraction, wake skew and wake curvature are illustrated. The wake contraction is due to the helicopter in hover condition which has described in the previous sections. The contraction parameter V is the summation of the non-dimensional freestream velocity (η) and twice of the induced velocity at the rotor disk (v). For

the helicopter in forward flight, the wake will be skewed with an angle of χ. For perfect edgewise flow, such skew angle will be 90° and the skew parameter becomes 1. The wake curvature parameter κ is $1/R$, where R is the curvature radius of the wake. This wake curvature parameter then will be put into the Peters-He finite state inflow model which is given in Eqs. (6.15) –(6.16). In Eq. (6.16), C_{nk} represents wake curvature inflow coupling.

$$\left[M^c \right]_{\text{new}} \left\{ \overset{*}{\alpha_k^1} \right\} + \left[L \right]^{-1} \left\{ \alpha_k^1 \right\} = \frac{1}{2} \left\{ \tau_n^m \right\} \tag{6.15}$$

where

$$\left[L \right] = \left[L^c \right] \left[V \right]^{-1} + \kappa \begin{bmatrix} 0 & \frac{1}{2} C_{nk}^T & 0 \\ C_{nk} & 0 & 0 \\ 0 & 0 & 0 \end{bmatrix} \left[V \right]^{-1} \tag{6.16}$$

Contraction	Skew	Curvature
$V = \eta + 2v$	$X = tan(\chi/2)$	$K = 1/\mathfrak{R}$
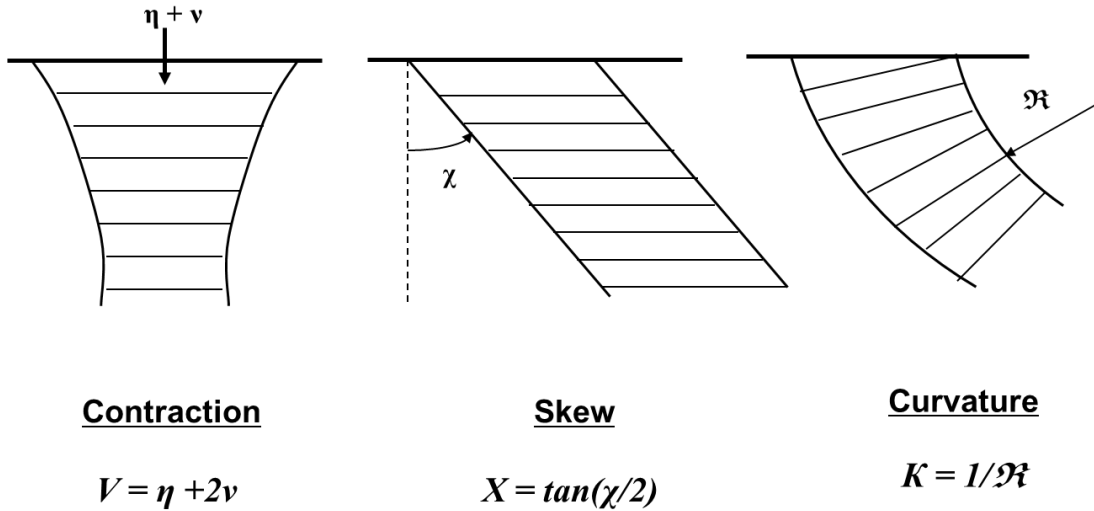
Figure 6.8 Wake distortion parameters

Finally, Ref. [21] demonstrated that, for accurate correlations, the mass flow parameter V, the wake skew parameter X, and the wake curvature parameter κ should not be instantaneously

changed as the flow variables changes. Rather, these three parameters need to be run through a first-order filter to give some time delay between a change of flight condition and the resultant changes in V, V_T, X or κ. Reference [21] found the correct time constants for these first-order time delays from experiments with free-wake analysis. This wake curvature effect and the first-order filters, introduce further nonlinearities into the model.

Since the present model is now formulated in terms of Huang-He variables, the previous work on wake curvature and time delays applies directly to the present model exactly as prescribed in [21]. The extra curvature terms in the He $[L]$ matrix can be directly placed into the odd-odd partition of the present $[L]$ matrix when it is in the Huang-He form. With this addition, the model posed here is a complete, nonlinear model for all three components of flow everywhere in the flow field.

Chapter 7: Conclusions

This dissertation has introduced a new methodology to obtain rotor induced velocity either on the rotor disk or off the disk. The induced velocity below the rotor disk can be computed through an adjoint theorem. The Nowak-He variables and Huang-He variables are both obtained from a single set of states through a change of variables. To make the solution converge well at all skew angles, the Morillo-Duffy solution and the change of variable solution (for example, Nowak-He solution for axial induced velocity, and Huang-He solution for x-component of the induced velocity) are blended with a closed-form downstream velocity (which is exact for perfectly edge-wise flow). This downstream flow is also obtained through an application of the Adjoint Theorem. Comparisons with the exact solution for steady and unsteady flow verify the effectiveness of the new approach. The extended blending method also showed better correlation with the exact solution.

In order to reduce the cost of computation, a version of the model with many fewer states has also been investigated. The reduced-order model has 2 harmonics for odd terms and 1 harmonic for even terms. Results with this reduced-order model for both axial velocity and swirl velocity still show good performance compared with the exact solution for reduced frequency less than 3.

Finally, the model has been extended to include important nonlinear terms. These are introduced to describe nonlinearities due to nonlinear momentum effects and nonlinear geometry effects due to wake deformations—including the wake contraction of the rotor slipstream. The contraction ratio is introduced, and it varies from 0 to 1. The contraction ratio approaches unity when the free stream velocity increases, which implies the rotor wake will become rigid when the free stream velocity increases, which implies the rotor wake will become rigid when the free

114

stream velocity is large enough. Nonlinearities are also introduced due to wake skew and wake curvature, making the model complete.

This new model is ready to be incorporated into production codes in the rotorcraft industry both for real-time flight simulation and for preliminary design calculations.

References

[1] Zhongyang Fei, "A Rigorous Solution for Finite-State Inflow Throughout The Flowfield," Doctor of Philosophy Thesis, Washington University in St. Louis, May 2013.

[2] Joglekar, M. and Loewy, R., "An actuator-Disk Analysis of Helicopter Wake Geometry and the Corresponding Blade Responses," USAAU-LABS Technical Report 69-66, 1970.

[3] Pitt, Dale. M. and Peters, David A., "Theoretical Prediction of Dynamic-Inflow Derivatives," Vertica, Vol. 5, No. 1, March 1981, pp. 21-34.

[4] Gaonkar, Gopal H. and Peters, David A., "Effectiveness of Current Dynamic-Inflow Models in Hover and Forward Flight," Journal of the American Helicopter Society, Vol. 31, No. 2, April 1986, pp. 47-57.

[5] Peters, David A., Boyd, David Doug, and He, Cheng Jian, "A Finite-State Induced-Flow Model for Rotors in Hover and Forward Flight," Journal of the American Helicopter Society, Vol. 34, No. 4, October 1989, pp. 5-17.

[6] Peters, David A. and He, Cheng Jian, "Correlation of Measured Induced Velocities with a Finite-State Wake Model," Journal of the American Helicopter Society, Vol. 36, No. 3, July 1991, pp. 59-70.

[7] Morillo, Jorge and Peters, David A., "Velocity Field above a Rotor Disk by a New Dynamic Inflow Model," Journal of Aircraft, Vol. 39, No. 5, September-October 2002, pp. 731-738.

[8] Peters, David A. and Cao, Wenming, "Off-Rotor Induced Flow by a Finite-State Wake Model," 37th AIAA SDM Conference, Salt Lake City, April 15-17, 1996, Paper No. 96-1550.

[9] Yu, Ke and Peters, David A., "Nonlinear Three-Dimensional State-Space Modeling of Ground Effect with a Dynamic Flow Field," Journal of the American Helicopter Society, Vol. 50, No. 3, July 2005, pp. 259-268.

[10] Hsieh, Antonio, "A Complete Finite-State Model for Rotors in Axial Flow," Master of Science Thesis, Washington University in St. Louis, August 2006.

[11] Peters, David A., Hsieh, Antonio, and Garcia-Duffy, Cristina, "A Complete Finite-State Inflow Theory from the Potential Flow Equations," Given as the Keynote Lecture and included in the Proceedings of the 3rd International Basic Research Conference on Rotorcraft Technology, Nanjing, China, Oct. 14-16, 2009.

[12] Fei, Zhongyang and Peters, David A., "A Rigorous Solution for Finite-state Inflow throughout the Flowfield," The 30th AIAA Applied Aero-dynamics conference, New Orleans, Louisiana, 2012.

[13] Fei, Zhongyang and Peters, David A., "Inflow below the Rotor Disk for Skewed Flow by the Finite-State, Adjoint Method," the 38th European Rotorcraft Forum, 2012.

[14] Peters, David A. and Modarres, Ramin, "A Compact Closed-Form Solution for the Optimum Induced-Flow Distribution of an Ideal Wind Turbine," Wind Energy, 6 FEB. 2013| DOI: 10.1002/we.1597.

[15] Peters, David A., "Two-Dimensional Incompressible Unsteady Airfoil Theory – An Overview," Journal of Fluids and Structures, Vol. 24, No. 3, July 2008, pp. 295-312.

[16] Ulrich, Xialing and Peters, David A., "Sinusoidal Locomotion of a Flexible Wing at High Reynolds Numbers," *Journal of Fluids and Structures*, E-Version, December 2013, 10.1016/j.jfluidstructs.2013.11.017; Print Version: Vol. 45, February 7, 2014, pp. 15-27

[17] Currie, I.G., Fundamental Mechanics of Fluids, 2nd Edition, McGraw Hill, United States of America, 1993, p.31.

[18] Chengjian He, "Development and Application of a Generalized Dynamic Wake Theory for Lifting Rotors," Doctor of Philosophy Thesis, Georgia Institute of Technology, July 1989.

[19] Barocela, Edward, "*The Effect of Wake Distortion on Dynamic Inflow for Lifting Rotors*," Master of Science Thesis, Washington University, May 1997.

[20] Krothapalli, K.R., Prasad, J.V.R., Peters, D.A., "Helicopter Rotor Dynamic Inflow Modeling for Maneuvering Flight," *Journal of the American Helicopter Society*, Vol. 46, No. 2, April 2001, pp. 129-139.

[21] Zhao, J., Prasad, J.V.R., and Peters, D. A., "Rotor Wake Distortion Model for Helicopter Maneuvering Flight," *Journal of the American Helicopter Society*, Vol. 49, No. 4, October 2004, pp. 414-424.

Appendix 1: Coordinate System

The ellipsoidal coordinate system $(v, \eta, \bar{\psi})$ is defined as

$$x = -\sqrt{1-v^2}\sqrt{1+\eta^2}\cos(\bar{\psi}) \tag{A1.1}$$

$$y = \sqrt{1-v^2}\sqrt{1+\eta^2}\sin(\bar{\psi}) \tag{A1.2}$$

$$z = -v\eta \tag{A1.3}$$

where the coordinates v, η and $\bar{\psi}$ are restricted to the following range

$$-1 \leq v \leq 1 \tag{A1.4}$$

$$0 \leq \eta \leq \infty \tag{A1.5}$$

$$0 \leq \bar{\psi} \leq 2\pi \tag{A1.6}$$

Figure A1.1 shows the ellipsoidal coordinate system viewed in the xz plane. The surfaces for $v = $ constant are hyperboloids and the surfaces for $\eta = $ constant are ellipsoids. For the special case, $\eta = 0$ represents the flat circular plane, and v is anti-symmetric along the plane which contains the $\eta = 0$ circular plane. $\bar{\psi}$ is the azimuth angle measured from the negative x axis, with counterclockwise direction viewed along the positive z axis.

The non-dimensional radial position with the ellipsoidal coordinates could be obtained from equations (A1.1) and (A1.2), which is

$$\bar{r}^2 = x^2 + y^2 + z^2 = (1+\eta^2)(1-v^2) + v^2\eta^2 \tag{A1.7}$$

Similarly, from equation (A1.1), (A1.2) and (A1.1), the ellipsoidal coordinates v, η and $\bar{\psi}$ can be expressed in terms of x, y and z as

$$v = \frac{-sign(z)}{\sqrt{2}} \sqrt{1 - \bar{S} + \sqrt{(\bar{S}-1)^2 + 4z^2}}$$
(A1.8)

$$\eta = \frac{1}{\sqrt{2}} \sqrt{\bar{S} - 1 + \sqrt{(\bar{S}-1)^2 + 4z^2}}$$
(A1.9)

$$\bar{\psi} = \tan^{-1}\left(\frac{-y}{x}\right)$$
(A1.10)

where

$$\bar{S} = x^2 + y^2 + z^2$$
(A1.11)
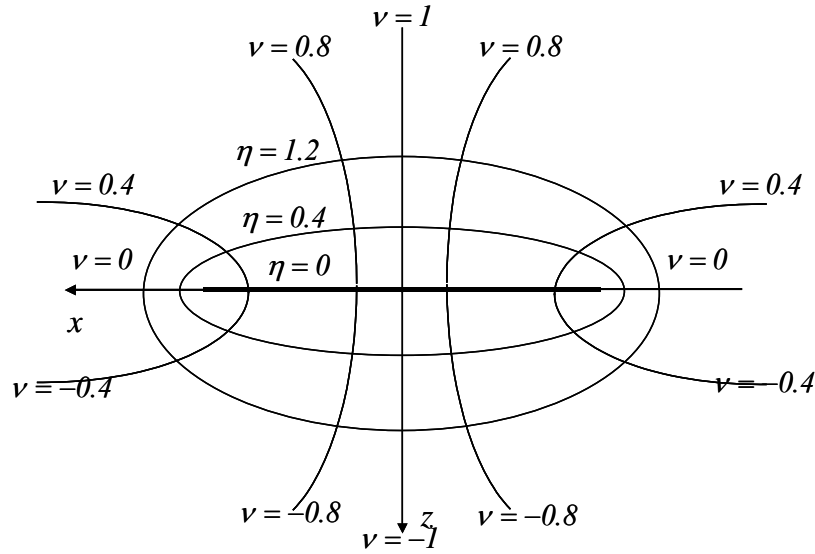
Figure A1.1 Ellipsoidal coordinate system

119

Appendix 2: Normalized Associated Legendre Functions

In the ellipsoidal coordinate system defined in Appendix 1, the Laplace's equation takes the form

$$\frac{\partial}{\partial v}\left[\left(1-v^2\right)\frac{\partial \Phi}{\partial v}\right]+\frac{\partial}{\partial \eta}\left[\left(1+\eta^2\right)\frac{\partial \Phi}{\partial \eta}\right]+\frac{\partial}{\partial \bar{\psi}}\left[\frac{\left(v^2+\eta^2\right)}{\left(1-v^2\right)\left(1+\eta^2\right)}\frac{\partial \Phi}{\partial \bar{\psi}}\right]=0 \quad \text{(A2.1)}$$

Using the principle of separation of variables to solve equation (A2.1), the Laplace equation is expressed by a multiplication of three separated parts which are only functions of v, η and $\bar{\psi}$ respectively.

$$\Phi\left(v,\eta,\bar{\psi}\right)=\Phi_1\left(v\right)\Phi_2\left(\eta\right)\Phi_3\left(\bar{\psi}\right) \quad \text{(A2.2)}$$

Applying Eq. (A2.2) to Eq. (A2.1), the Laplace equation can be separated into the following three equations

$$\frac{d^2\Phi_3}{d\bar{\psi}^2}+m^2\Phi_3=0 \quad \text{(A2.3)}$$

$$\frac{d}{dv}\left[\left(1-v^2\right)\frac{d\Phi_1}{dv}\right]+\left[-\frac{m^2}{1-v^2}+n\left(n+1\right)\right]\Phi_1=0 \quad \text{(A2.4)}$$

$$\frac{d}{d\eta}\left[\left(1+\eta^2\right)\frac{d\Phi_2}{d\eta}\right]+\left[\frac{m^2}{1+\eta^2}-n\left(n+1\right)\right]\Phi_2=0 \quad \text{(A2.5)}$$

where m and n are the constant of separation.

120

Equations (A2.4) and (A2.5) are Legendre's associated differential equations, and the solutions to which are the associated Legendre Functions of the first kind and the second kind ($P_n^m(v)$, $P_n^m(iv)$, $Q_n^m(\eta)$ and $Q_n^m(i\eta)$). Since $P_n^m(iv)$ and $Q_n^m(\eta)$ will yield an infinite pressure in the flow field, so they are omitted.

For the purpose of this research, the associated Legendre functions of the first and second kind are normalized as

$$\bar{P}_n^m = (-1)^m \frac{P_n^m(v)}{\rho_n^m} \tag{A2.6}$$

$$\bar{Q}_n^m = \frac{Q_n^m(i\eta)}{Q_n^m(i0)} \tag{A2.7}$$

where

$$\left(\rho_n^m\right)^2 = \int_0^1 \left(P_n^m(v)\right)^2 dv = \frac{1}{2n+1}\frac{(n+m)!}{(n-m)!} \tag{A2.8}$$

$$Q_n^m(i0) = \begin{cases} \dfrac{\pi}{2}(-1)^{m+n+1}(i)^{n+1}\dfrac{(n+m-1)!!}{(n-m)!!}, & m+n=even \\[4mm] (-1)^{m+n+1}(i)^{n+1}\dfrac{(n+m-1)!!}{(n-m)!!}, & m+n=odd \end{cases} \tag{A2.9}$$

In this research, numerical codes are developed to compute all the required values of $\bar{P}_n^m(v)$ and $\bar{Q}_n^m(i\eta)$ based on the following recurrence relations

$$\bar{P}_{n+1}^m(v) = \sqrt{\frac{(2n+3)(2n+1)}{(n+1)^2 - m^2}}\left[v\bar{P}_n^m(v) - \sqrt{\frac{n^2-m^2}{4n^2-1}}\bar{P}_{n-1}^m(v) \right] \tag{A2.10}$$

121

$$\bar{P}_{n+1}^{m}(v) = \sqrt{\frac{(2n+3)}{(n+m+1)(n+m)}} \left[\sqrt{\frac{(n-m+1)(n-m)}{2n-1}} \bar{P}_{n-1}^{m}(v) \atop + \sqrt{1-v^2}\sqrt{2n+1}\bar{P}_{n}^{m-1}(v) \right] \tag{A2.11}$$

$$\bar{P}_{n}^{m+1}(v) = \frac{1}{\sqrt{1-v^2}} \left[\sqrt{\frac{(2n+1)(n+m)}{(2n-1)(n+m+1)}} \bar{P}_{n-1}^{m}(v) - \frac{(n-m)}{\sqrt{(n+m+1)(n-m)}} v\bar{P}_{n}^{m}(v) \right] \tag{A2.12}$$

$$\bar{Q}_{n+1}^{m}(i\eta) = \bar{Q}_{n-1}^{m}(i\eta) - (2n+1)K_{n}^{m}\eta\bar{Q}_{n}^{m}(i\eta) \tag{A2.13}$$

$$\bar{Q}_{n}^{m+1}(i\eta) = \frac{1}{\sqrt{1+\eta^2}} \left[\bar{Q}_{n-1}^{m}(i\eta) - (n-m)K_{n}^{m}\eta\bar{Q}_{n}^{m}(i\eta) \right] \tag{A2.14}$$

where

$$K_{n}^{m} = \left(\frac{\pi}{2}\right)^{(-1)^{n+m}} H_{n}^{m} \tag{A2.15}$$

$$H_{n}^{m} = \frac{(n+m-1)!!(n-m-1)!!}{(n+m)!!(n-m)!!} \tag{A2.16}$$

$$(n)!! = \begin{cases} (n)(n-2)(n-4)...(2) & \text{for } n \text{ even} \\ (n)(n-2)(n-4)...(1) & \text{for } n \text{ odd} \end{cases} \tag{A2.17}$$

$$(0)!! = 1, \ (-1)!! = 1, \ (-2)!! = \infty, \ (-3)!! = -1$$

In order to calculate to the derivation of $\bar{P}_{n}^{m}(v)$ and $\bar{Q}_{n}^{m}(i\eta)$, the recurrence relations for are

given by

$$(1-v^2)\frac{d\bar{P}_{n}^{m}(v)}{dv} = \sqrt{\frac{(2n+1)(n^2-m^2)}{(2n-1)}} \bar{P}_{n-1}^{m}(v) - nv\bar{P}_{n}^{m}(v) \tag{A2.18}$$

122

$$\left(1-v^2\right)\frac{d\bar{P}_n^m(v)}{dv} = \sqrt{(n+m+1)(n-m)}\sqrt{1-v^2}\,\bar{P}_n^{m+1}(v) - mv\bar{P}_n^m(v) \qquad (A2.19)$$

$$\left(1+\eta^2\right)\frac{d\bar{Q}_n^m(i\eta)}{d\eta} = -\left[\frac{1}{K_n^m}\bar{Q}_{n+1}^m(i\eta) + (n+1)\eta\bar{Q}_n^m(i\eta)\right] \qquad (A2.20)$$

$$\left(1+\eta^2\right)\frac{d\bar{Q}_n^m(i\eta)}{d\eta} = \sqrt{1+\eta^2}\,\frac{Q_n^{m+1}(i0)}{Q_n^m(i0)}\bar{Q}_n^{m+1}(i\eta) + mn\eta\bar{Q}_n^m(i\eta) \qquad (A2.21)$$

where K_n^m is defined by Eq. (A2.22)

A2.1 Orthogonality Integrals

$$\int_0^1 \bar{P}_j^m(v)\bar{P}_n^m(v)\,dv = \begin{cases} \delta_{jn}, & n+m=odd,\ j+m=odd \\ \delta_{jn}, & n+m=even,\ j+m=even \\ U_{jn}^m, & n+m=even,\ j+m=odd \end{cases} \qquad (A2.23)$$

$$U_{jn}^m = \sqrt{\frac{H_n^m}{H_j^m}}\,\frac{\sqrt{(2j+1)(2n+1)}}{(j+n+1)(j-n)}(-1)^{\frac{j+n-2m-1}{2}} \qquad (A2.24)$$

A2.2 Area Integrals

$$\int_0^1 \bar{P}_n^m(v)\bar{P}_j^m(v)v\,dv = \begin{cases} A_{jn}^m, & j+m=odd,\ n+m=odd \\ G_{jn}^m, & j+m=even,\ n+m=even \\ D_{jn}^m, & j+m=odd,\ n+m=even \end{cases} \qquad (A2.25)$$

where A_{jn}^m, G_{jn}^m and D_{jn}^m are defined as:

$$A_{jn}^m = \frac{2}{\sqrt{H_n^m H_j^m}}\,\frac{\sqrt{(2n+1)(2j+1)}}{(n+j+2)(n+j)}\,\frac{(-1)^{\frac{n+j-2m}{2}}}{\left((j-n)^2-1\right)} \qquad (A2.26)$$

123

$$G_{jn}^m = \begin{cases} \sqrt{H_j^m H_n^m} \sqrt{(2j+1)(2n+1)} \dfrac{\left(2m^2 - n^2 - j^2 - n - j\right)}{(n+j+2)(n+j)} \dfrac{(-1)^{\frac{n+j-2m}{2}}}{\left((n-j)^2 - 1\right)}; \\ \\ \qquad\qquad\qquad\qquad\qquad\qquad\qquad j \neq 0; n \neq 0; m \neq 0 \\ \\ \qquad G_{00}^0 = \dfrac{1}{2} \quad j = n = m = 0 \end{cases} \tag{A2.27}$$

$$D_{jn}^m = \begin{cases} \sqrt{\dfrac{1}{H_j^m H_n^m}} \dfrac{1}{\sqrt{(2j+1)(2n+1)}}, \, j = n \pm 1 \\ \\ \qquad\quad 0, \, j \neq n \pm 1 \end{cases} \tag{A2.28}$$

Curriculum Vitae

JIANZHE HUANG

EDUCATION

Washington University in St. Louis	*St. Louis, MO*
PhD in Mechanical Engineering	2013.01-2015.05
Southern Illinois University Edwardsville	*Edwardsville, IL*
Master's in Mechanical Engineering	2009.08-2012.12
South China University of Technology	*Guangzhou, China*
Bachelor of Science in Electrical Engineering	2005.09-2009.06

EXPERIENCE

Teaching Assistant — *Edwardsville, IL*

Department of Mechanical Engineering, SIUE
- Instructor of ME 262 (Dynamics) in Spring 2012
- Instructor of ME 356L (Dynamics Systems Laboratory) in Fall 2011

Electrical Engineering Intern — *Yichang, China*

China Gezhouba Corporation — 2008.06-2008.07

PROJECTS

Team Leader, Attenuation Tests on Tie PADs (*Unit Rail*)	2010.02-2010.09
Fatigue and Static Properties of *Tie PAD 2.5.1* (*Unit Rail*)	2009.10-2010.02
Collar Port-holes Specimen Fatigue Test (*Schlumberger*)	2010.02-2010.07
Fatigue Damage Test of Collar Port-holes (*Schlumberger*)	2011.01-2012.08
Seismic Test of Computer Server Frame (*APC by Schneider Electric*)	2011-2012
The GEN II OWS Transducer Test (*Amsted Rail*)	2012.08-2012.11
An Investigation to Design the Gusset Plates in Steel Trusses	2012.01-2012.06

HONORS

Outstanding Cadres of Student Association in SCUT (2008)
Outstanding Graduate Student in SIUE (2011)

PROFESSIONAL MEMBERSHIPS/AFFILIATIONS

- ASME Student Membership since 2011

PUBLICATIONS AND PRESENTATION

Journal publications

- **Jianzhe Huang**, Albert C. J. Luo (2015), "Periodic Motions and Bifurcation Trees in a Buckled, Nonlinear Jeffcott Rotor System", *International Journal of Bifurcation and Chaos*, Vol. 25, No. 1, 1550002 (34 pages)
- **Jianzhe Huang**, David A. Peters, J.V.R. Prasad (2014), "Converged Velocity Field for Rotors by a Blended Potential Flow Method", GSTF on Journal of Aviation Technology, in press.
- **Huang, Jianzhe** and Luo, Albert C. J. (2014), "Analytical periodic motions on bifurcations in a nonlinear rotor system", *International Journal of Dynamics and Control*, Issue 2, pp 425–459.
- Luo, Albert C. J. and **Huang, Jianzhe** (2013), "Period-3 motions to chaos in a softening Duffing oscillator", International Journal of Bifurcation and Chaos, 24 (3), Article no.: 1430010 (26 pages)
- Luo, Albert C. J. and **Huang, Jianzhe** (2012), "Unstable and Stable Period-m Motions in a Twin-well Potential Duffing Oscillator", Discontinuity, Nonlinearity, and Complexity, 1, 113-147.
- Albert C.J. Luo and **Jianzhe Huang** (2013), "Asymmetric periodic motions with chaos in a softening Duffing oscillator", *Int. J. Bifurcation Chaos*, Vol.23, Issue 05, 1350086 (31 pages).
- Albert C.J. Luo and **Jianzhe Huang** (2013), "Analytical Solutions for Asymmetric Periodic Motion to Chaos in a Hardening Duffing Oscillator", *Nonlinear Dynamics*, Vol.72, Issue 1-2, pp 417-438.
- Albert C.J. Luo and **Jianzhe Huang** (2013), "Analytical period-3 motions to chaos in a hardening Duffing oscillator", *Nonlinear Dynamics*, Vol.73, pp 1905-1932.
- Albert C.J. Luo and **Jianzhe Huang** (2012), "Approximate solutions of periodic motions in nonlinear systems via a generalized harmonic balance", *Journal of Vibration and Control*, Vol.18, Issue 11, pp 1661-1674.
- Albert C.J. Luo and **Jianzhe Huang** (2012), "Analytical Dynamics of Period-*m* Flows and Chaos in Nonlinear Systems", *Int. J. Bifurcation Chaos,* Vol.22, Issue 04,1250093 (29 pages)
- Albert C.J. Luo and **Jianzhe Huang** (2012), "Discontinuous dynamics of a non-linear, self-excited, friction-induced, periodically forced oscillator", *Nonlinear Analysis: Real World Applications*, Vol.13, Issue 1, pp. 241-257
- Albert C.J. Luo and **Jianzhe Huang** (2012), "Analytical Routes of Period-1 Motions to Chaos in a Periodically Forced Duffing Oscillator with a Twin-well Potential", *Journal of Applied Nonlinear Dynamics*, Vol. 1, Issue 1, pp. 73-108

Conference Publications and Presentations

- **Jianzhe Huang** and D.A. Peters, "Real-Time Solution of Nonlinear Potential Flow Equations for Lifting Rotors", 5th Nonlinear Science and Complexity, August 4-9, 2014, Xi'an, China.
- **J. Huang**, D. A. Peters, M. Nowak and J. V. R. Prasad, "Converged velocity field for rotors by a blended potential flow method", AHS 70th Annual Forum and Technology Display, May 20-22, 2014.
- **Jianzhe Huang** and Albert C.J. Luo, "Analytical Solutions for Period-1 Motions in a Nonlinear Jeffcott Rotor System", IDETC/CIE, August 4-7, 2014, Portland, Oregon, USA, DETC2014-35458.
- Albert C.J. Luo and Jianzhe Huang, "Period-3 motions and bifurcation in a softening duffing oscillator", IDETC/CIE, August 17-20, Buffalo, New York, USA, DETC2013-13002.
- Albert C. J. Luo and **Jianzhe Huang**, "Stability and Bifurcation analysis of periodic motions in a periodically forced Duffing oscillator", The 2011 ASME International mechanical Engineering Congress and Exposition, IMECE11, November 11-17, 2011, Denver, Colorado, USA, IMECE 2011-62949.
- Albert C.J. Luo and **Jianzhe Huang**, "Switchability conditions of motions in a nonlinear, friction-induced oscillator", ASME 2011 International Design Engineering Technical Conferences & Computers and Information in Engineering Conference, IDETC/CIE, August 21-31, Washington, DC, USA, DETC2011-47384.
- Albert C.J. Luo and **Jianzhe Huang**, "Approximate analytical solutions of complex periodic motions and chaos in a nonlinear Duffing oscillator", 3rd International conference on Dynamics, Vibrations and Control, August 2011.